Nature and efficiency of pyroclast generation from porous magma: Insights from field investigations and laboratory experiments

Inauguraldissertation

zur Erlangung des Doktorgrades

der Fakultät für Geowissenschaften

der Ludwig-Maximilians-Universität München

vorgelegt von

Ulrich Küppers

München, 21. Juli 2005

1. Berichterstatter:	Prof. Donald Bruce Dingwell
2. Berichterstatter:	Prof. Ludwig Masch
Tag der mündlichen Prüfung:	23. November 2005

[…] On the morning of his departure he put his planet in perfect order. He carefully cleaned out his active volcanoes. He possessed two active volcanoes; and they were very convenient for heating his breakfast in the morning. He also had one volcano that was extinct. But, as he said, “One never knows!” So he cleaned out the extinct volcano, too. If they are well cleaned out, volcanoes burn slowly and steadily, without any eruptions. Volcanic eruptions are like fires in a chimney.

On our earth we are obviously much too small to clean out our volcanoes. That is why they bring no end of trouble upon us. […]

From “The Little Prince” by Antoine de Saint-Exupéry

Fiat 500 in Catania, Italy, covered in ash settling from the plume of Mt. Etna. 3 November 2002

Content

List of figures

List of tables

List of abbreviations

BAF	block-and-ash flow
BET	Brunauer-Emmett-Teller
BP	before present
CT	computer tomography
DRE	dense rock equivalent
e.g.	exempli gratia (for example)
ka	Thousand years (kilo years)
LMU	Ludwig-Maximilians-Universität [München]
Ma	Million years
MP	measurement point
MPa	Mega Pascal
MSH	Mount St. Helens
OP	open porosity/offene Porosität
OUV	Older Unzen Volcano
PEF	potential energy for fragmentation
SC	sample container
USDP	Unzen Scientific Drilling Project
YUV	Younger Unzen Volcano

Thanxx to

Prof. Donald Bruce Dingwell for coming to Munich and offering and supervising this very interesting topic. Thereby, I became assured to resign from my job in a geological engineering bureau.

My parents who enabled this scientific life by always supporting me. “Non scolae sed vitae discimus” was written at Grundschule Schaftlach. I was struggling through my first years of Latin but many years after having successfully received the „großes Latinum“, this language turned out to be very useful for travelling on Italian volcanoes…

My sisters Barbara, Claudia, and Andrea for going through the Küppers way of education, countless competitions of who is having the longest hairs, opening my mind to topics I hadn’t been aware of before or simply having a drink in the fridge. I was wearing a green tie for the defence.

Donia for her love, agreeing in usually volcano-orientated holidays, patiently enduring the periods of me being in the field or being bad-tempered in the later stage of the thesis.

Oli (we can do everything!) Spieler for introducing me into the mystery (misery?) of magma fragmentation, opening many inspiring questions (some of them still unsolved…) and interest in the progress of this work.

My colleagues in office and lab, Bastel Müller (Did you make the EGU meeting get moved to Vienna in order to not get wet again in Nice?) and Betty Scheu (not only for insisting to be my co-pilot during the Sicily field trip. I’m looking forward to climbing Mt. Fuji!). It was a pleasure to work with you and you probably prevented me having a date with a psychologist….

Several colleagues for many hours inside and outside science or in the field, namely (in alphabetic order) Alex (Sir Bamboo) Nichols, Alfonso (most excellent) Davila, Annarita Mangiacapra, Ben (wicked) Kennedy, Jacopo (buona colata) Taddeucci, and many more unmentioned but not forgotten.

The institute’s secretaries, especially Greta for frequent help and assistance in any kind of, organisational, and bureaucratic questions.

The mechanics Wolfgang and Martin for helping me out whenever something had broken or got stuck.

Setsuya Nakada and Hiroshi Shimizu who were great help before, during and after our field campaigns to Unzen

All professors involved in the Umlauf of this thesis. Their cooperation and fast proceeding allowed a publication in 2005.

Thanxx to

Flo (Fuoco) for always being there, either just for a beer, a slide show or going to Stromboli and/or Etna.

Ziggy for always being there (too!), cutting his hair first, co-organizing the best parties in Waakirchen (the famous lagerfiregrillwurschtcontest, a legend since 1990) and drinking Red Bull.

This work was funded by the projects DI 431-14-3, DI 431-20-1 from the German Science Foundation (DFG), the EU project MULTIMO as well as general University funds.

Preamble

Parts of the data presented in this thesis have been published in scientific journals or are in the process of reviewing. Below, these papers are listed in alphabetic order of their first authors:

Kennedy B, Spieler O, Scheu B, Kueppers U, Taddeucci J, Dingwell DB (2005) Conduit implosion during vulcanian eruptions. Geology 33/7, 581-584

Kueppers U, Scheu B, Spieler O, Dingwell DB (2005) Field-based density measurements as tool to identify pre-eruption dome structure: set-up and first results from Unzen volcano, Japan. JVGR 141, 65-75.

Kueppers U, Scheu B, Spieler O, Dingwell DB. Fragmentation efficiency of explosive volcanic eruptions: a study of experimentally generated pyroclasts. JVGR, in press

Scheu B, Kueppers U, Mueller S, Spieler O, Dingwell DB. Petrophysical analysis of the 1990-1995 Unzen eruption: an experimental synthesis. Submitted to JVGR

Spieler O, Kennedy B, Kueppers U, Dingwell DB, Scheu B, and Taddeucci J (2004) The fragmentation threshold of pyroclastic rocks. EPSL 226, 139-148

Zusammenfassung

Es gibt eine stetig wachsende Anzahl von Menschen, die im Umkreis von Vulkanen leben, die in historischer Zeit aktiv waren und bei denen mit weiteren Ausbrüchen gerechnet werden muss. Da eine Umsiedlung aller potentiell von Naturgefahren gefährdeten Personen unmöglich ist, ist ein für jeden Einzelfall optimiertes Risikomanagement unabdingbar. Im Zusammenhang mit dem von aktiven Vulkanen ausgehenden Gefährdungspotential ist es daher vonnöten, die vor und während eines Vulkanausbruchs ablaufenden Prozesse bestmöglich zu quantifizieren und damit verstehen zu können. Bis vor einigen Jahren war dies nur durch Versuche an Analogmaterialien und/oder durch numerische Modellierungen möglich. Um die Risikoabschätzung zu optimieren, genügen diese beiden vereinfachenden Angehensweisen nicht mehr.

Intensive Geländeuntersuchungen frischer, vulkanischer Eruptionsprodukte und deren präzise Charakterisierung stellen – unter Abwägung der vulkanischen Risiken und logistischer Probleme - eine gute und schnelle Art dar, wichtige Informationen über die vor und während eines Ausbruchs ablaufenden Prozesse und deren Dynamik zu sammeln. Daneben erlaubten experimentelle Weiterentwicklungen Experimente an natürlichen Proben im in Vulkanen vorkommenden Temperatur- und Druckbereich und ermöglichten die umfassende Analyse der generierten Feinpartikel. Durch kontrolliertes Verändern eines einzelnen Versuchsparameters konnte dessen Einfluss auf den Verlauf und Ausgang eines Experimentes sehr genau bestimmt werden. Diese Informationen stellen wichtige, für eine realitätsnahe Risikofallmodellierung benötigte Eingabeparameter dar.

Im Rahmen der vorliegenden Arbeit wurden folgende Fragestellungen erstmalig bearbeitet bzw. der vorhandene Datensatz beträchtlich erweitert:

- Welche Rückschlüsse auf den Internaufbau eines Vulkandoms und damit auf das Magmenaufstiegs- und Entgasungsverhalten kann man aus der Untersuchung der Porosität einer statistischen Anzahl von repräsentativen Proben aus den vulkanischen Ablagerungen ziehen (Kapitel II)?

Im Rahmen von zwei Geländekampagnen in den Jahren 2000 und 2001 wurde zusammen mit Kollegen die Porosität von mehr als 1100 Proben aus den Ablagerungen des jüngsten Ausbruchs (1990-1995) des Vulkans Unzen, Japan gemessen. Zu diesem Zweck wurden die trockenen Proben in Plastiktüten eingeschweißt und an Luft sowie unter Wasser gewogen. Aus beiden Differenzgewichten ließen sich die Dichte und die Porosität errechnen. Die Daten zeigten einheitlich eine bimodale Dichteverteilung mit Porositätswerten von 8.0 bzw. 20.5 vol. %. Diese beiden Werte konnten mit Lagen unterschiedlicher Porosität korreliert

werden, die im Spine nahezu senkrecht und in den Domloben annähernd hangparallel ausgerichtet waren. Aus dieser Anordnung und der ermittelten Dichteverteilung ließen sich Rückschlüssen auf das Aufstiegs- und Fließverhalten sowie die Magmenentgasung ziehen.

- Wie viel Überdruck muss in Abhängigkeit von der offenen Porosität einer Probe angelegt werden, um durch schnelle Druckentlastung deren vollständiges Zerbrechen zu erwirken (Kapitel III-6.1)?

Die Untersuchung des Fragmentationsverhaltens natürlicher Proben und die Ermittelung des Bruchschwellenwertes (= ΔP_{fr}) wurde in der „Fragmentationsbombe“ (Alidibirov und Dingwell, 1996) durchgeführt. Sie besteht aus einem hitzeresistenten Hochdruckautoklaven („Vulkan“), einem großen, darüber liegenden Tank („Atmosphäre“) zum Rückgewinnen der künstlich erzeugten Feinpartikel und einer zwischengeschalteten Berstscheibe („Magmapfropfen“), die den Überdruck im Autoklaven sicherstellte. Experimentelle Weiterentwicklungen dieses Aufbaus (Spieler et al., 2004) erlaubten Experimente im in Vulkanen vorkommenden Temperatur- und Druckbereich und ermöglichten zudem die umfassende Analyse der generierten Feinpartikel. Durch eine Anordnung von bis zu drei Berstscheiben war es im Rahmen dieser Versuchsreihe möglich, die verwendeten zylindrischen Proben (Höhe = 60 mm, Durchmesser = 26/25 mm) einer Temperatur von 850 °C und einem Druck von bis zu 50 MPa auszusetzen. Der Druck wird über in den Autoklaven eingeleitetes Argon, welches auch die offene Porosität füllt, angelegt. Nach Erreichen des thermischen Gleichgewichts und stabilen Enddrucks wurde die Fragmentation durch ein gezieltes Überschreiten der Stabilität der obersten Berstscheibe initiiert. Da jede Berstscheibe einem bestimmten Relativdruck widerstehen kann, führt die Öffnung der obersten Berstscheibe in unmittelbarer Folge zur Öffnung der mittleren und unteren Berstscheibe. Daraufhin breitet sich eine Dekompressionswelle in den Autoklaven aus und trifft nach kurzer Zeit auf die Probeoberfläche. Das unter Überdruck stehende Gas in der offenen Porosität wird sich aufgrund des eingestellten Druckgefälles schnell auszudehnen beginnen. Die offene Porosität der verwendeten Probe und der während des Experiments angelegte Druck in Kombination entscheiden darüber, bei welchem Druck eine Probe erstmalig komplett zerbrochen und in den über dem Autoklaven befindlichen Tank ausgeworfen wird.

Die ermittelten Ergebnisse zeigen eine negative, nicht-lineare Korrelation des Bruchschwellenwertes mit der offenen Porosität (OP). Der Abfall der Bruchschwelle dichter Proben (0 – 15 vol. % OP) mit zunehmender Porosität ist sehr stark, Proben mit höherer

Porosität weisen eine nur schwache Abnahme des Bruchschwellenwertes auf. Versuche an Proben mit hohen Porositätswerten zeigten zudem den starken Einfluss der Blasentextur (Größe, Anzahl, Form) auf das Bruchverhalten, da in großporigen Proben ein Teil des angelegten Drucks entweichen kann ohne vorher zur Fragmentation merklich beigetragen zu haben (Probenpermeabilität. siehe Mueller et al., 2005). Die Ergebnisse legen die Vermutung nahe, dass die Fragmentation der Proben in den vorliegenden Versuchen die Folge eines komplexen Zusammenspiels mehrerer Prozesse war. Der Einfluss folgender drei Parameter gilt als gesichert: Scherkräfte an der Probenhalter- respektive Conduitwand, die Zugfestigkeit der Blasenwände und die Blasentextur.

- Welchen Einfluss hat die angelegte Energie (das Produkt aus Porosität und angelegtem Druck) auf die Genese von Aschepartikeln (Kapitel III-6.2)?

Die Effizienz des Bruchprozesses wurde hinsichtlich der Größenverteilung und der Oberflächenzunahme der experimentell erzeugten Feinpartikel untersucht. Die Versuche wurden in der Fragmentationsbombe durchgeführt. Nach jedem Experiment wurde der Tank mit destilliertem Tank in einen Sedimentationszylinder mit einem unten angeschraubten Glaskolben ausgespült. Dabei wurde eine Größenseparation bei 250 µm vorgenommen. Nach zwei Tagen Sedimentationszeit wurde das überstehende Wasser abgelassen und sämtliche Feinpartikel im Glaskolben konzentriert. Mit Hilfe eines Rotationsverdampfers konnte diese Fraktion schnell getrocknet und anschließend gewogen werden. Die getrocknete Grobfraktion wurde gesiebt und die Siebfraktionen gewogen.

Die Oberfläche der experimentell erzeugten Pyroklastika wurde mittels Argon-Adsorption in einem Micromeritics® Gemini 2375 bestimmt. Zu diesem Zweck wurden vier Korngrößenbereiche getrennt gemessen (<250 µm; 250 µm <x< 710 µm; 710 µm <x< 2 mm; >2 mm). Die Oberflächenzunahme ergab sich aus einem Vergleich der ermittelten Oberflächenwerte der Fragmentationsprodukte mit denen der Probenzylinder vor den Experimenten. Für alle drei untersuchten Probensätze zeigte sich ein positiver Zusammenhang zwischen angelegtem Druck und abnehmender Durchschnittspartikelgröße wobei Partikel >2 mm keinen messbaren Zugewinn an Oberfläche aufwiesen. Zusammengerechnet wiesen die Proben mit dem mittleren Porositätswert generell einen höheren Wert an Oberflächenzunahme auf als die porösesten Proben. Dies liegt vermutlich daran, dass mit zunehmender Porosität die Blasenwandstärke und somit die pro Bruch erzeugte neue Oberfläche abnimmt.

Die Größenanalyse umfasste trockenes Sieben (Partikel >250 µm) und Laserbeugung (Partikel <250 µm suspendiert in destilliertem Wasser) in einem Coulter® LS230 mit Partikelgrößenanalyse nach der Fraunhofer Theorie. Durch eine Umberechnung der Ergebnisse der Laserbeugungsmessungen (vol. % in Gew. %) war es mögliche, die Ergebnisse beider Techniken zu kombinieren. Die Methode der Partikelgrößenbestimmung mittels Laserbeugung beruht auf der Annahme sphärischer Partikelform und konstanten Brechungsindex. Feinpartikel vulkanischer Gesteine erfüllen beide Normen in der Regel nicht. Zur Kontrolle der Laserbeugungsergebnisse wurden daher die Partikel nach den Messungen zurückgewonnen und bis Maschenweite 63 µm trocken gesiebt. Ein Abgleich ergab einen unerheblichen Einfluss auf den Verlauf der Partikelverteilungskurve im Bereich <250 µm.

- Wie hoch ist die porositätsabhängige Abrasion in trockenen Massebewegungen und welchen Einfluss hat dies auf die ermittelten Gelände- und Laborergebnisse (Kapitel III-7)?

Die Abrasionsversuche wurden an acht Probensätzen (vier unterschiedliche Porositätswerte bei je zwei Partikelgrößen) durchgeführt. Die Probe (zwischen 40 und 160 g, bis zu 100 Partikel) wurde hierzu in einen Gummizylinder gegeben, der sich horizontal und konstant schnell drehte. Die Versuchsdauer betrug zwischen 15 und 120 Minuten. Die Ergebnisse zeigten eindeutig die Zunahme der Abrasivität mit zunehmender Porosität, Partikelgröße, sowie Versuchsdauer. Ihr transportweitenabhängiger Einfluss während der Block-und-Asche Ströme ist nicht von der Hand zu weisen, konnte jedoch an Hand der Ablagerung des jüngsten Ausbruchs des japanischen Vulkans Unzen (1990-1995) nicht eindeutig nachgewiesen werden, da aufgrund der verstrichenen Zeit zwischen Ausbruchsende und Geländekampagnen keine Zuordnung der einzelnen Messpunkte zu Fließeinheiten mehr möglich war. Die geringen Mengen an erzeugten Feinpartikeln <250 µm ließen den Rückschluss zu, dass die Abrasion während des Trocknungsprozesses der Feinpartikel aus den Fragmentationsexperimenten nur eine untergeordnete Rolle spielte.

I Introduction

As of today, approximately 500 million people live within 100 km of a historically active volcano. However, many recent and historic volcanic eruptions did not only have an impact on the direct neighbourhood of a volcano but a rather world-wide one (e.g. (in alphabetic order) El Chichon [Mexico], 1982; Krakatoa [Indonesia], 1883; Laki [Iceland], 1792-94; Pinatubo [Philippines], 1991; Tambora [Indonesia], 1815; Vesuvius [Italy], 79). As for any potential natural disaster, it will likely remain impossible to completely relocate people away from potentially threatened areas. Therefore, the best possible protection includes intense surveying, optimized forecasting, and realistic and reliable hazard assessment. To deal with the imminent risk of active volcanoes, this requires a detailed knowledge of pre- and syn-eruptive processes, data that can not be achieved exclusively from direct field observation.

Buoyancy differences are a first order reason for the rise of magma. Volcanic eruptions may be phreatic, phreatomagmatic or magmatic, the latter scenario of which was addressed in this study. Rising magma is subject to decreasing lithostatic pressure. As a direct consequence, volatiles become increasingly oversaturated and bubbles will nucleate and grow depending on initial volatile content and melt viscosity. Both factors directly influence the diffusivity that limits the rate of bubble growth. Increasing amounts of bubbles increase the buoyancy difference to the surrounding rocks and lead to an acceleration of the rising melt-bubble mixture. Beside the limiting factors mentioned above, the overpressure in the gas bubbles greatly depends on the magma's ascent speed as it controls the residence time to conditions favourable to degassing (a combination of lithostatic pressure and magma temperature) and the time of overpressure reduction due to degassing. Dingwell (1996) evaluated the viscoelastic properties of magma at fragmentation and showed that any liquid will break if the applied stress is too high to be compensated by elastic deformation and too rapidly applied to be compensated by viscous deformation. Papale (1999) modelled the onset of magma fragmentation as a consequence of high acceleration rates upon bubble growth and magma rise. Volcanic eruptions occur when the bubbly melt can no longer withstand the exerted stress that derives from the overlying weight (lithostatic pressure), the expanding gas bubbles (internal gas overpressure) and different ascent velocities in the conduit (velocity profile). The melt will be fragmented and the gas-pyroclast mixture will be erupted.

This study has combined close investigation of the deposits of the 1990-1995 eruption of Unzen volcano, Japan (chapter II) and detailed laboratory investigations on samples of this eruption and other volcanoes (chapter III).

The field work intended to reveal the density distribution of samples from within the eruptive products. Although all samples already underwent one eruption, their physical state (e.g. crystallinity, porosity) mostly remained close to sub-surface pre-eruption conditions due to their high viscosity and accordingly allowed their usage for the analysis of the fragmentation behaviour. In that purpose, rapid decompression experiments that simulate volcanic eruptions triggered by internal gas overpressure have been performed at 850 °C to evaluate fragmentation threshold and fragmentation efficiency. Laboratory investigations of that kind are one approach to bridge the gap between observational field volcanology and risk assessment as they reveal information on what can not be investigated closely but what is essential to know for realistic eruption models and the adjacent hazard mitigation. Changing the experimental conditions and close investigation of the artificial products reveals the influence of physical properties on the fragmentation behaviour.

II Field work and sampling

1 Geological setting and eruptive history of Unzen volcano

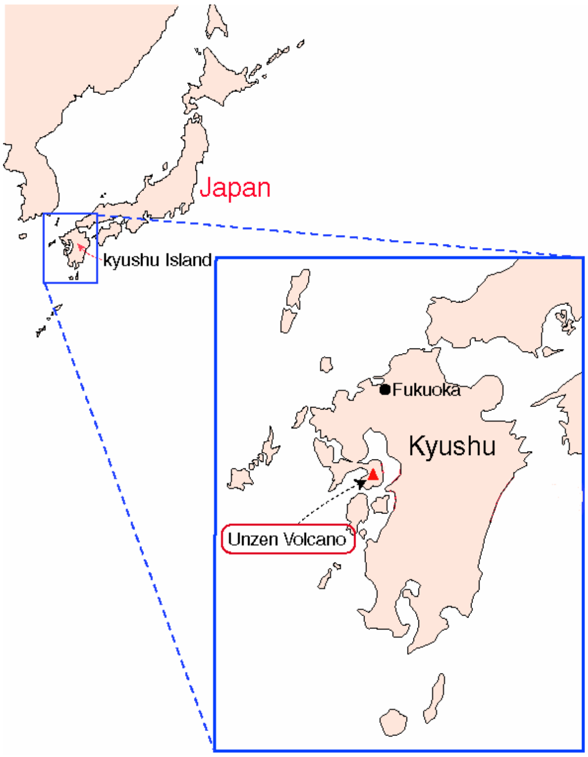

Figure 1: Map showing the location of Unzen volcano on Kyushu, the southermost of the four main islands of Japan. (taken from: http://133.5.170.64/Museum/Museum-e/Part2-e/kyushu-e/kyushu-e.htm)

The volcano Unzen is located on the Shimabara peninsula on Kyushu, the southernmost of the four major islands constituting Japan (Figure 1). Tectonically, it is part of the “Ring of fire”, a volcanic chain along converging plate boundaries that limit most of the Pacific Ocean. In South Japan, the Philippine Sea Plate is being subducted west-north-westwards. The active volcanic chain on Kyushu is called Ryukyu arc and comprises e.g. Sakurajima, Kirishima and Tsurumi volcanoes. Unzen lies approximately 70 km off to the West of this volcanic arc in an active East-West directed volcanotectonic depression. This Unzen graben (up to 2 mm of subsidence and 14 mm of spreading per year) is part of a chain of several “en echelon” rifts that extends south-eastwards in an oblique way from the Ryuku arc into the East China Sea (Figure 2). Eruptive products of Unzen have almost entirely filled the graben. As a consequence, its dimensions above sea level can only be estimated to 30-40 km in East-West and 5 km in North-South direction (Hoshizumi et al., 1999).

The onset of volcanic activity in this area is marked by the beginning subsidence that is believed to have begun approximately 500 ka ago. The volcanic history of Unzen can be divided in two parts, the Older Unzen volcano (OUV) and the composite Younger Unzen volcano (YUV) with a gap in activity between 200 and 100 ka BP. Although approximately 120 km^3 of magma were erupted during the 300 ka of OUV activity, fairly little is known about this first period as most of its deposits have been covered by deposits of YUV. Recently, two flank drillings (USDP-1 [752 m final depth below surface] at the north-eastern and USDP-2 [1463 m final depth below surface] on the eastern flank) successfully penetrated

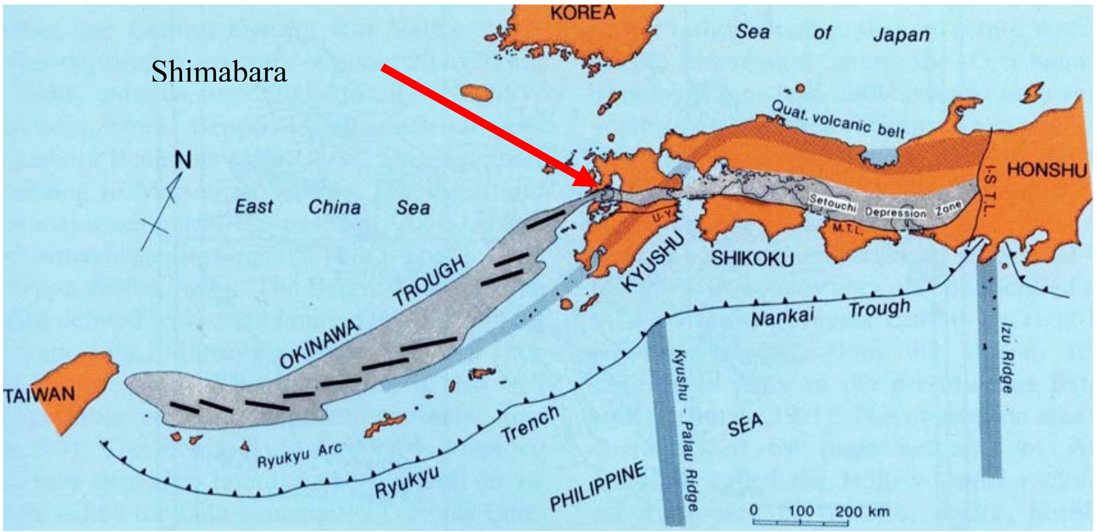

Figure 2: Tectonic map of Southern Japan (Okada, 1992). Unzen (red arrow) is located 70 km to the West of the quaternary volcanic belt in one of several “en echelon” segments.

the deposits of OUV and YUV and reached the underlying basement (Hoshizumi et al., 2004). A further drilling project (USDP-4, USDP-3 was the pilot drilling) targeted the conduit and successfully penetrated it at around sea level, i.e. roughly 1.400 m below the dome (Nakada et al., 2004). As only few explosive eruptions are documented in the cores, the volcanic history of OUV can be summarized as a series of non-explosive effusions of thick lava flows and/or domes associated with gravitationally driven block-and-ash flows (BAF). Approximately 8 km³ of porphyritic andesite to dacite were erupted since 100 ka BP (YUV). Several collapse events, preferentially with eastward collapse directions did take place. As the volcanic activity was not restricted to a single eruption centre, Unzen volcano is a volcanic complex with several peaks, each of which resulting from a single eruptive period. YUV can be subdivided into Nodake, Myokendake, Mayuyama, and Fugendake eruption centres (“-dake” is Japanese for peak). The activity from the Fugendake centre started about 20 ka BP within the scar of the Myoken caldera. It comprises five lava flows, four lava domes, four pyroclastic flow deposits and one debris-avalanche deposit. The historic activity dates back to 1663 when the Furuyake lava flow (olivine-bearing basaltic andesite) started from a vent within the Myoken caldera scar and flowed 1 km to the North. In 1792, the Shin’yake lava flow (dacite) erupted from a vent very close to the 1663 site and flowed north-eastwards for 2 km. This eruption was accompanied by many earthquakes, strong fumarolic activity, and changes in groundwater flows and temperatures. On 21 May 1792, one month after the extrusion of the flow, Mayuyama hill (a 4 ka old lava dome, 3 km to the East of the flow vent) collapsed. The resulting debris avalanche destroyed big parts of the town of Shimabara, entered the sea, and generated a tsunami that killed approximately 15.000 people at the opposite shore of the

Shimabara bay. Several times during the 20th century, frequent earthquakes shook Mt. Unzen without being accompanied by volcanic activity.

2 The last eruption of Unzen volcano (1990-1995)

The last eruption had been preceded by many earthquakes from November 1989 on. The hypocenters were located to the West of Unzen beneath the Chijiwa Bay and moved east- and upwards with time. The first volcanic tremor beneath the Fugendake summit was recorded in early July 1990. On 17 November 1990, phreatic eruptions occurred from two craters in the summit region and marked the end of a 198 years quiescence period. Activity declined after few days but resumed in February 1991 with phreatomagmatic eruptions. On 20 May, lava was first observed at the surface and quickly filled the crater. From 24 May on, the lava overflowed the crater rim and the first gravitationally driven BAFs occurred. They generally ran out in easterly directions (Figure 3) with runout distances usually below 3 km from the

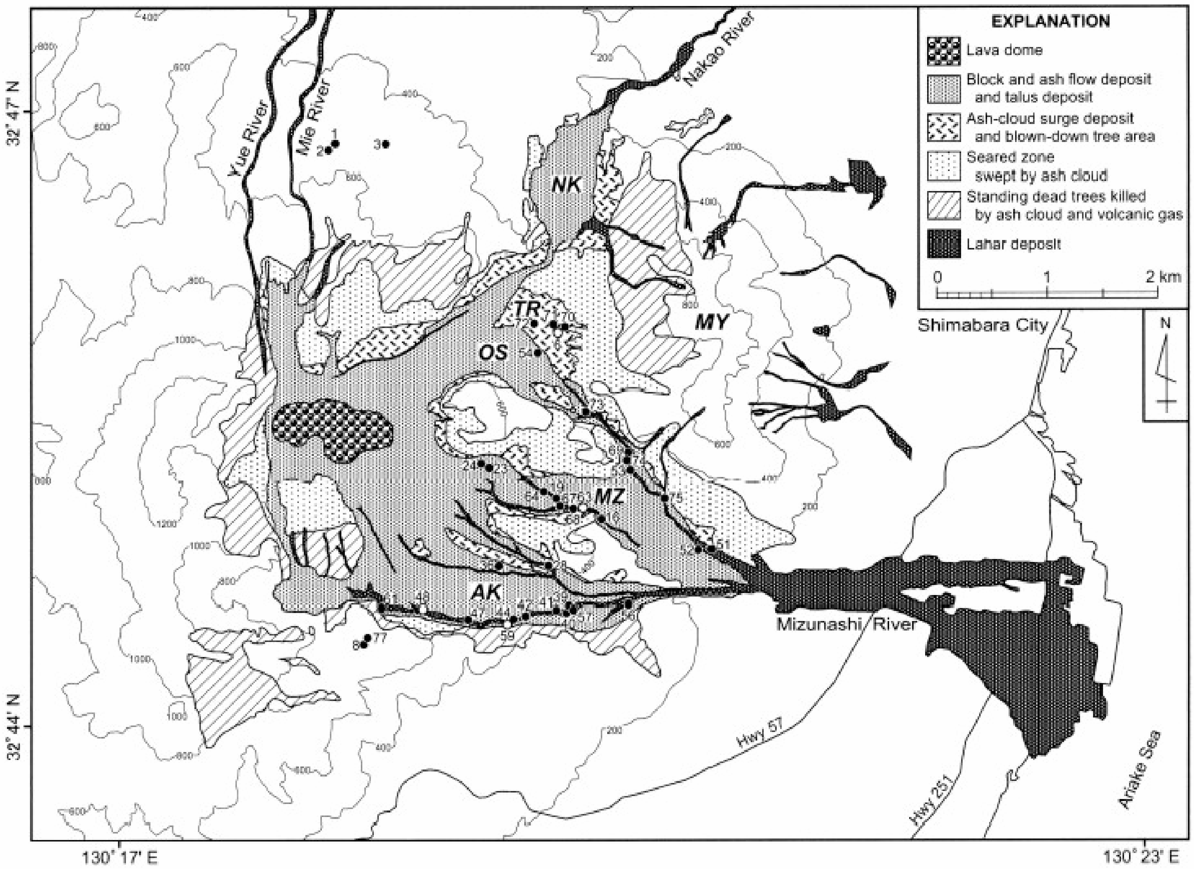

Figure 3: Map showing the deposits of the 1990-1995 Unzen eruption (Miyabuchi, 1999). It shows the deposits as of 18 September 1995. The BAF with the maximum runout distance (19 July 1993, 5.6 km from the source) reached the Highway 57 (Hwy 57) in the Mizunashi river valley. (AK for Akamatsudani, MZ for Mizunashi, OS for Oshigadani, and NK for Senbongi valley, respectively. TR for Taruki Height, MY for Mayuyama Hill.)

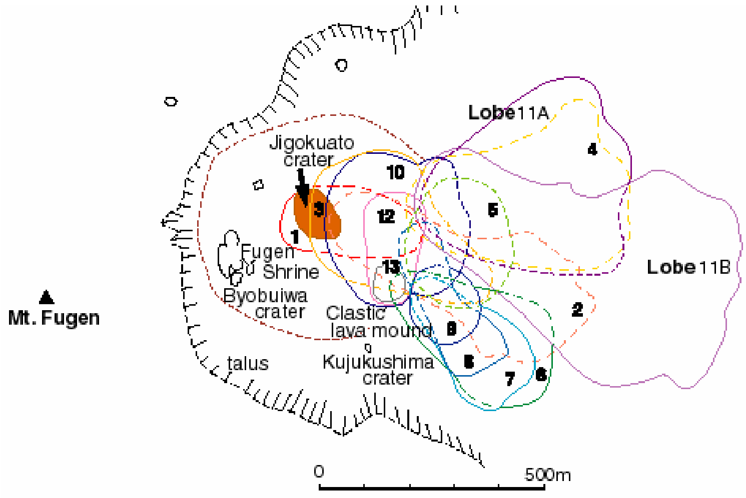

Figure 4: Sketch map of the maximum dimension of each lobe before its collapse or overflowing. This eruption produced a complex dome, built-up of at least 14 single lobes. (http://133.5.170.64/Museum/Museum-e/Part3-e/P8-e/dome_keisei-e.htm)

source (Ui et al., 1999). The largest BAFs took place on 3 June, 8 June, and 15 September 1991, and 23 June and 19 July 1993, the latter of which had the longest overall runout distance (5.6 km). Lava extrusion continued at variable extrusion rates until February 1995 and built up a complex dome by endogenous and exogenous growth (Figure 4). This Heisei-Shinzan ("Shinzan" is Japanese for "new mountain", "Heisei" is the name of the recent era in Japan that began on 8 January 1989) lava dome is made up of fourteen dome lobes (Nakada et al., 1999). Today, lobe 11 B on the eastern flank and the dome with the spine are the most

Figure 5: Dome as seen from North-East. The latest eruption of Unzen produced a complex dome, formed of at least fourteen single lobes. Many lobes collapsed gravitationally or are overlain by later exogenous lobes. Due to that, most of what can be seen of the dome today is made up of lobes 11 B.

prominent morphological features (Figure 5, 7). Apart from that, remnants of lobe 11 A (to the North of lobe 11 B) and lobes 6 and 8 (to the South of lobe 11 B) are still visible while nearly all preceding or following lobes had been buried by these lobes or were removed by collapses. The current dimension of the dome is approximately 800 m in North-South, 1.200 m in East-West, and 240 m in vertical extension. The total erupted volume during this eruption is estimated to be 2.1 km³ (dense rock equivalent), 0.9 km³ of which are represented by the dome in its today's state (Nakada et al., 1999 and literature cited therein).

3 The deposits of the 1990-1995 eruption

Figure 6: Extrusion area of lobe 11 A, looking northeastwards. As the confining pressure of the conduit walls is released upon extrusion, the lava shows differently oriented extension cracks.

3.1 The Dome

As described above, the last eruption produced a complex dome by endogenous and exogenous growth. The growth behaviour could be correlated with the effusion rate and was exogenous when the effusion rate was high (Nakada et al., 1999). The effusion rate showed two peaks. The still existing dome lobes (11 B, 6, 8, and 11 A in order of volume) have been formed primarily exogenously and show primary extrusive structures like crease structures and unloading cracks (Figure 6). The coverage of such lobes with loose blocks was only minor in proximal parts. In distal parts, ramp structures and flank-parallel shear bands were visible. The flow front of lobe 11 B flowed down the Eastern flank of Unzen for approximately 700 m. The last growth stage of the dome (since mid 1994) was again

Figure 7: Picture looking north-eastwards. The dome surface is completely covered with angular, mostly dense blocks. The spine is bisected and can be seen in the background. Height of the spine is approximately 30 m, width 150 m.

endogenous. The area around the spine is completely covered by angular, mostly dense blocks of up to several meters size. At few locations, a solidified spine has pierced through the carapace of blocks. The most prominent one is a bisected structure that in total is 30 m high and 150 m wide and makes up the point of highest elevation (1.486 m asl, Figure 7). This is 240 m above the pre-eruption surface (Jigokuato crater). Nonaka et al. (2004) investigated the residual water content and revealed that the spine had solidified 420 m below surface. The western part of the spine (left side in Figure 7) is the site of strong fumarolic activity. On 17 October 2003, the temperature at this fumarole was recorded as being 326 °C (most recent update on the web page of Shimabara Earthquake and Volcano Observatory). During the Unzen Scientific Drilling project (USDP-4) that tempted to penetrate the conduit of the last eruption, the highest measured temperature was 155 °C in July 2004 at a depth of approximately 1.400 m below the spine. However, it was assumed that this temperature had been reduced by the drilling fluid and expected to reach 200 °C (Sakuma et al., 2004). In addition to the high degree of alteration of the recovered samples, the unexpected low temperatures encountered during the conduit drilling are believed to be due to effective cooling by hydrothermal fluid circulation (Setsuya Nakada, pers. comm.)

3.2 Block-and-ash flow (BAF) deposits

Fugendake lies inside the Myoken caldera, a horseshoe-shape structure open to the East. From 24 May 1991 on, the extruding lava overflowed the Jigokuato crater rim and BAFs

Figure 8: Cross-section through an erosional channel in Akamatsudani valley, approximately 20 m high. The alternation of thin ash-rich layers (bright grey) and unsorted BAF deposits is clearly visible. Bettina Scheu (arrow) in the middle for scale.

travelled down the flanks of Unzen in easterly directions. Most of them were generated by gravitational instabilities (Merapi-type). The flow direction was closely correlated with the direction of dome growth. The first valley to become affected was Mizunashi valley. The Senbongi valley was affected in May 1993, after thick deposits inside the Oshigadani valley allowed subsequent BAFs to overrun the Taruki Height, a former prominent morphological feature. The last BAF travelled down inside the Akamatsudani valley. The deposits are composed of several flow units of up to 5 m thickness (Miyabuchi, 1999) that are not welded (Figure 8). The final thickness does locally exceed 200 m (Nakada et al., 1999). The BAF deposits contain angular to subangular blocks of up to 10 m in size that frequently exhibit post-deposition, in-situ fragmentation by cooling joints that are either radially arranged (blocks with homogeneous porosity) or parallel to layers with varying porosity (Figure 9a, b).

Fig. 9: The BAF deposits are covered by many large blocks that show in-situ fragmentation by cooling cracks. These cracks can be either radially arranged (9 a, left) or in a parallel way (9 b, right).

During the monsoon seasons, heavy rainfalls frequently triggered lahars. These lahars produced deep erosional channels in all affected valleys. However, it is assumed that a large fraction of the BAF deposit surfaces has remained relatively unchanged. One indicator of this assumption were randomly distributed chunks of wood on top of the BAF deposits that have been carbonised exclusively at their bottom by the latent heat of the deposits (Miyabuchi, 1999). To reduce the imminent risk of lahars, seeds and young, quickly growing plants were distributed by helicopter on the steep, upper slopes of Unzen. As of 2001, the vegetation density generally increased uphill. Apart from lahar reworking, infrastructure rebuilding and dam construction heavily changed the deposits in lower parts of Akamatsudani, Mizunashi, Oshigadani, and Senbongi valleys.

Many blocks in the BAF deposits and on the dome showed a layered porosity distribution (Figure 10). This had important implications for emplacement mechanisms and fragmentation behaviour (see below). Several blocks in the BAF deposits showed friction mark-like structures (up to 50*50 cm large) with a few mm thin layer of cataclasite that could have resulted from block-block collision during BAF transport. However, some blocks on the dome showed similar features, some of which were fractured perpendicular to the movement direction (Figure 11). As collisions during the BAFs could accordingly not exclusively be responsible for these features, some of them may result from shallow processes in the dome or the uppermost part of the conduit where a point load simultaneously caused superficial shearing and fracture opening. As none of these features on blocks from within the BAF deposits was found to be covered with a thin layer of pseudotachylite as found by Schwarzkopf et al. (2000) on Merapi, the impact-induced energy was – in the case of the investigated blocks – not sufficiently high to cause superficial melting. The energy is a

Fig 10 (left): The porosity was often arranged in layers of several centimetres to a few decimetres (width of picture is 1 m).
Fig. 11 (right): Friction mark-type structure with cataclasite surface and fractures perpendicular to the movement direction (coin for scale, width of picture is 35 cm).

function of temperature, mass, and velocity difference of two (or more) colliding blocks. At Unzen, the blocks have most probably been too “cold” to allow for impact-induced melting.

4 Field-based density measurements

4.1 Introduction

Ascending magmas show variable porosity in space and time. Although a paramount input parameter for valid and realistic models of eruptive behaviour, the density distribution within complex domes or conduits is still poorly known. Conduit-filling rocks have been made accessible either by erosion (e.g. Inyo dome, USA) or drilling (Unzen), but it is assumed that their physical properties (e.g. porosity, state of alteration) differ from the ones of the melts that ascended therein during an eruption. Within the volcanic edifice, the physical properties of silica-rich magma are, due to its high viscosity, only subject to minor changes. Therefore, the density distribution from within the deposits of volcanic eruptions may be used to shed light on pre-eruptive conditions. Knowledge on the density distribution is important for future hazard assessment in general (via modelling conduit flow and dome collapse/explosion behaviour) and the likelihood of an explosive eruption during a volcanic crisis in particular.

4.2 Methods of laboratory density measurements

Most of the common methods to determine the density/porosity of volcanic rocks are not practicable for extensive investigations as they involve sample transport to the laboratory and specific sample preparation:

- Water saturation (e.g. Belikov et al., 1964; Schopper, 1982; Cas and Wright, 1987; Gardner et al., 1996) requires a very long pre-measurement preparation time (or high vacuum) and it cannot be assured that all pores are completely water-filled (especially large pores on the surface of the sample will leak immediately).
- Impregnation with a silicon spray (Houghton and Wilson, 1989).
- Coating with saran (Mayfield and Schiffman, 1998).
- Coating with cellulose acetate (Polacci et al, 2003).
- Coating with paraffin by briefly submerging the sample in liquid paraffin (Raue, 2004).

Methods 2 to 5 require a drying period of the coating. As the coating is a thin film on the sample surface, the volume of broken-up bubbles on the surface is excluded during the volumetric measurement.

- Mercury-intrusion porosity (Belikov et al., 1964). This method is not practicable for samples with varying pore size and can lead to structural collapse of pumiceous samples. As some Mercury will remain in the samples, these contaminated samples may not be used for other investigations.

4.3 Field-based density measurements

Performing density measurements directly at the point of deposition reduces the logistic effort enormously as no sample transport is necessary. The density of the samples is determined using the Archimedean principle, i.e. the weight and the buoyancy of the sample must be known. The buoyancy is achieved by measuring the weight of the dry sample below water. To avoid time-consuming pre-measurement sample preparation either by water-saturating or coating, the measuring procedure was changed and the weight of a dry sample, evacuated in a plastic bag, is determined in air and under water. Both values are used to calculate the density according to:

$$\rho_{sample} = \frac{m_{air}}{m_{air} - m_{water}} * \rho_{water} . \qquad \text{Eq. 1}$$

m_{air} is the weight of the sample (g) evacuated in a plastic bag in air and m_{water} is the weight of the same sample (g) submerged. ρ_{water} was assumed to be 1 (g/cm³).

In the light of this new approach, a set-up that allowed for quantifying the density of volcanic rocks directly in the field was designed (Figure 12). It consisted of:

- Vacuum pump (Metzger, Germany), maximum vacuum is 250 mbar.
- Precise digital balance (Ohaus, Germany), maximum load is 4.1 kg.
- An aluminium tripod with a holding device for the balance.
- A water-proof bag or a bucket.
- 10 litres of water and
- Minor consumable items (plastic bags, glue).

The total weight (including water) was below 20 kg and all needed equipment could be easily carried by two people. It was used extensively during two field campaigns on Unzen volcano. The energy for the vacuum pump and the balance was supplied by rechargeable AA-batteries, making the measurements independent of direct power supply in the field. To avoid bag failure during and after evacuation, one of three different types of plastic bags with different wall thickness was chosen depending on the roughness of the sample surface. The buoyancy of the used plastic bags was found to be minor and therefore negligible.

Figure 12: The set-up for the density measurements directly in the field. The balance is fixed on the tripod. A water reservoir (right) is placed below the balance and the sample can be submerged with a special holding device (left). The inset shows the vacuum pump, the silicon injection device and plastic bags.

Set-up: The balance was fixed on top of the tripod with three adjustment screws guaranteeing a horizontal position. The waterproof bag was hung centrally below the balance, from where a holding device led down to the sample holder. The measurements have been performed inside the waterproof bag acting as water reservoir and screen. Additionally, a special measuring program of the balance, taking the average weight over a thirty seconds period, was used to exclude any influence of the wind on the weighing. No pre-evacuation sample preparation was required. Two specific weights of each evacuated sample have been determined: (1) the weight of the dry sample in air and (2) under water. For the latter weight, samples have been evacuated in plastic bags. In this purpose, a line of highly viscous, silicon-based glue was squeezed on the bag rim. This glue made energy-consuming melting procedures (e.g. for plastic bag sealing in kitchens) unnecessary. After placing a plastic tube that connected the sample surface to the vacuum pump, the bag was closed along the line of glue. Upon switching the vacuum pump on, the bag became sucked onto the rock sample. The glue kept the vacuum stable for at least fifteen minutes after having pulled the plastic tube out of the bag. During the two campaigns on Unzen, thirty samples have usually been measured at each measurement point (MP). The time needed was about three hours, consisting of fifteen minutes for collecting, fifteen minutes for the set-up of the apparatus and approximately five minutes per sample for evacuation procedure and measurement.

In order to minimize secondary changes to the deposits, future measurements of the described kind should be performed as soon as possible after the end of an eruption:

“Deposit freshness”: secondary influences such as erosion, weathering, or human processes may dramatically change the state of the deposits or influence the relative abundance of different components greatly. Extensive dam constructions are taking place at Unzen to reduce the risk and possible hazards of lahars.

“Vegetation”: the growth of vegetation can make the deposits inaccessible and accelerate the weathering process. During 1991 through 1993, several lahars occurred during the monsoon season. As a matter of risk mitigation, fast-growing plants were distributed from helicopters on the steep, unconsolidated slopes made up of BAF deposits. These plants effectively stabilized the slopes and diminished the number of hazardous lahars.

Eruptive activity permitting, measurements on fresh deposits would allow for a better horizontal and temporal resolution of density variations. Sample dimensions (max. 20 cm) and climatic conditions (dry samples are needed) may impose limitations on the use of this method.

4.4 Results

The method described above has been successfully applied to the deposits of the 1990-1995 eruption of Unzen volcano. Measurements have been primarily performed in the four valleys that were most affected by BAFs and on the dome (Figure 13). Short set-up and measurement times allowed up to sixty measurements per day under fieldwork conditions. More than 1100 samples with a total weight of 2.2 tons have been measured and thereby clearly demonstrated the feasibility of this method during two field campaigns:

- 175 samples with more than 150 kg of weight have been measured in the year 2000 together with Bettina Scheu, Dr. Oliver Spieler and Dr. Joachim Gottsmann.
- 927 samples with slightly more than 2 tons of weight have been measured in the year 2001 together with Bettina Scheu.

A statistically significant data set of density distribution of clasts from within BAF deposits could be achieved. As no reports of similar field-based density investigations have been found in literature, this data set was the first of its kind. Density investigations have been performed on the surface of the BAF deposits. Due to the time interval that had passed between the end of the eruption and the field work, it remained impossible to correlate single

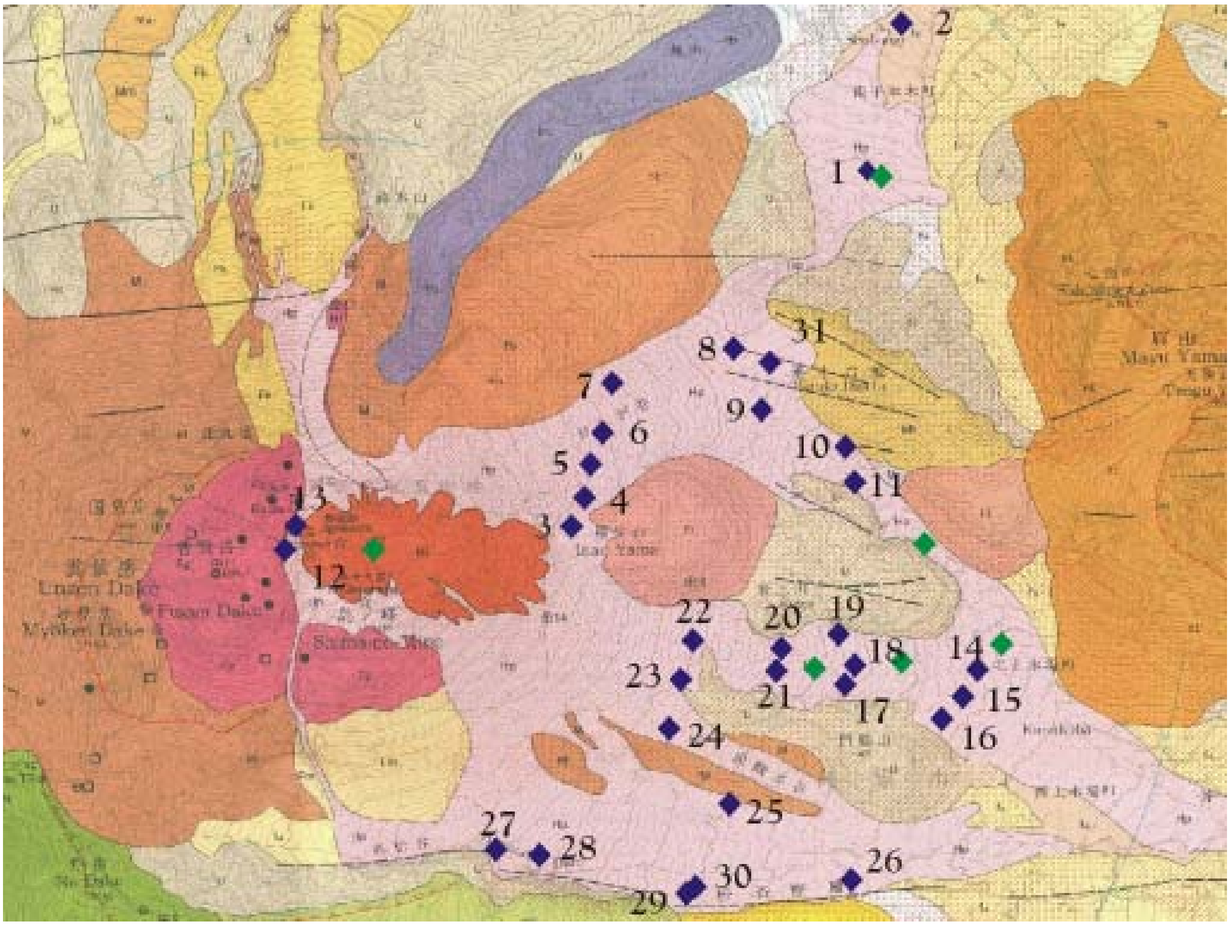

Figure 13: Map showing the location of field based density measurements (on geological map by Watanabe and Hoshizumi, 1995). The pink colour indicates BAF deposits, the dark orange shows the extension of the dome. Blue diamonds indicate measurement locations (MPs) of the campaign in the year 2001, green diamonds the MPs of the 2000 campaign. (map width is 6 km)

MPs to deposits of single flow units. The four valleys and the dome have each been analysed independently. The density distribution is shown in two graphs, one at 0.05 g/cm³ resolution (left) to precisely show the density results, one at 0.1 g/cm³ resolution (right) to highlight the peak locations of density abundance. For the case of Oshigadani valley, a very high resolution had to be chosen to graphically highlight the peak at low porosity (= high density). Using the program *PeakFit*™, the density distributions have been analysed and the peaks and their fraction were evaluated. All five data sets revealed their statistical reliability (probability, randomness) and showed concordantly bimodal results with peaks at 2.0 +/- 0.05 and 2.3 +/- 0.05 g/cm³ but changing peak ratios. The peak ratio values corresponded to the area covered by each peak curve (gaussian) as fraction of the total area. Below, the results of each valley (from North to South) and the dome have been described separately.

- Senbongi Valley (MP 1 and 2):

This valley is located to the Northeast of Unzen approximately 3 km away from the lowermost parts of the dome lobe in its today's extension. It was first affected on 23 June 1993 after a major collapse of lobe 11 A. Until then, Senbongi had been protected by the Taruki Height. After the Oshigadani Valley had been filled as thick as 100 m by the deposits of earlier BAFs (Nakada et al., 1999), the former morphological feature could be overrun and BAFs entered the Senbongi valley by falling down a vertical cliff of approximately 100 m height. Although only few BAFs affected this area, they directly led to a complete loss of infrastructure, buildings and cultivated areas. The outcrop situation was generally poor due to dense vegetation and dam construction. 54 samples were measured at two MPs with a resulting mean density of 2.1 g/cm^3 (range is 1.6 to 2.4 g/cm^3). The distribution was found to be bimodal with peaks at 2.05 and 2.35 g/cm^3, representing 65 and 35 %, respectively (Figure 14).

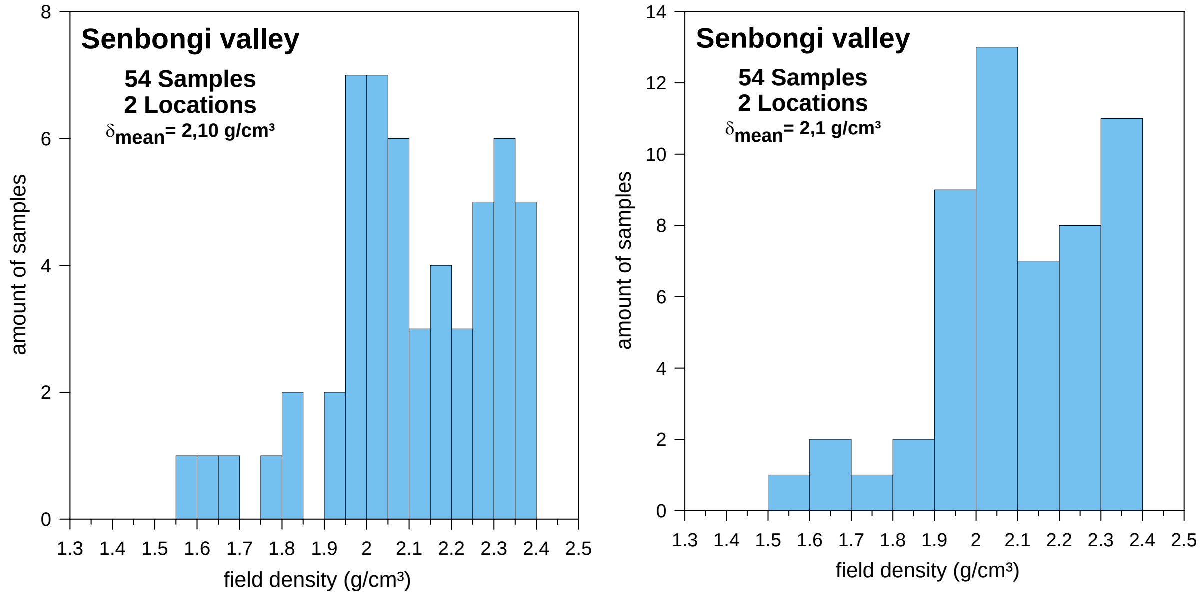

Figure 14: Plot showing the density distribution of 54 samples measured at two locations in Senbongi valley. The left graphs shows the density at high resolution (0.05 g/cm^3), the right graphs highlights the peaks of density abundance (0.1 g/cm^3) at 2.05 and 2.35 g/cm^3.

- Oshigadani Valley (MP 3 to 11 and 31):

This valley to the Eastnortheast of Unzen was affected by BAFs from 25 August 1991 on until the end of the BAF activity in early 1995. The deposit thickness locally exceeded 100 m (Nakada et al., 1999). The reworking activity was concentrated on a major erosional channel on the northern edge that is leading to a waterfall entering the Senbongi valley. Despite the dense vegetation, a good distribution of measuring locations was possible in the middle and upper parts and 298 samples have been measured at ten MPs indicating an average density of

2.0 g/cm³ (range is 1.4 to 2.4 g/cm³). The density distribution was evaluated to be bimodal with peaks at 2.075 and 2.25 g/cm³, representing 60 and 40 %, respectively (Figure 15).

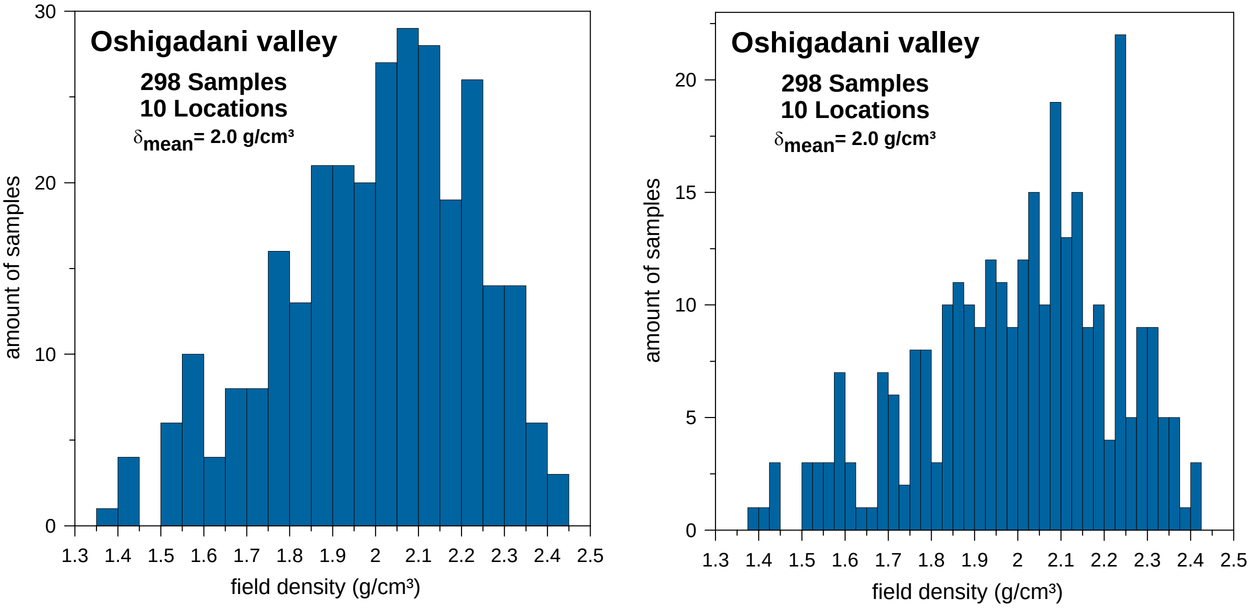

Figure 15: Plot showing the density distribution of 298 samples measured at ten locations in Oshigadani valley. The left graphs shows the density at high resolution (0.05 g/cm³), the right graphs highlights the peaks of density abundance (0.025 g/cm³) at 2.08 and 2.25 g/cm³. In the case of this valley, a very fine resolution had to be chosen to graphically show the peak at high density.

- Mizunashi Valley (MP 14 to 23):

For the first three months after 24 May 1991 (onset of BAF activity), BAFs exclusively travelled down this valley directly to the East of the volcano. It was only affected until June 1993 as, after the dome growth had shifted its direction, the later occurring BAFs travelled

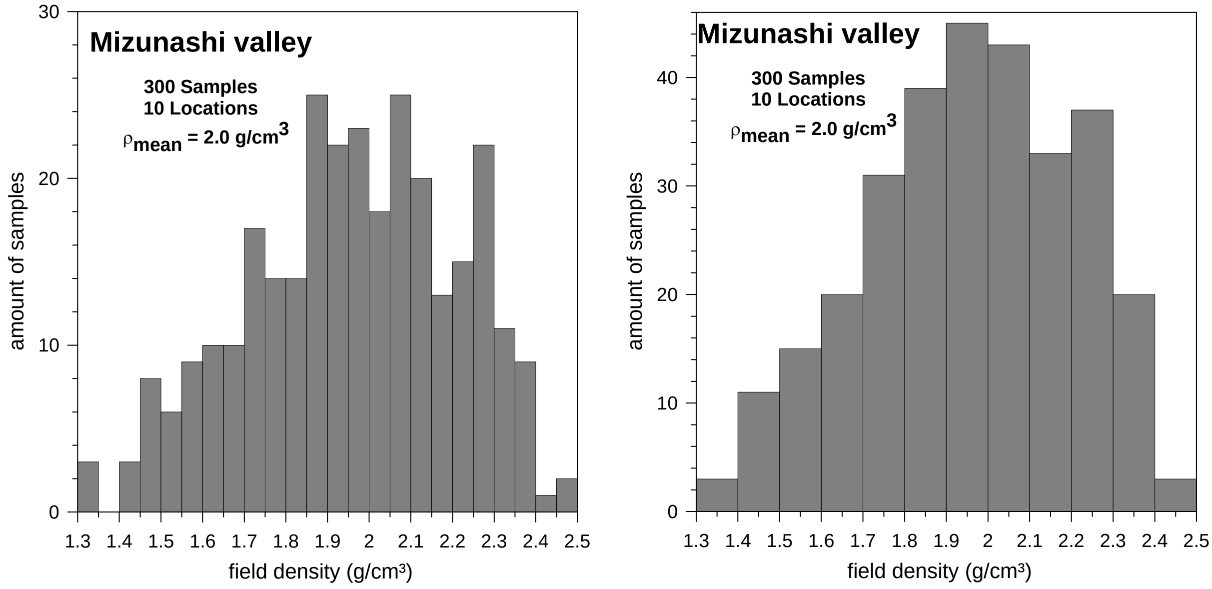

Figure 16: Plot showing the density distribution of 300 samples measured at ten locations in Mizunashi valley. The left graphs shows the density at high resolution (0.05 g/cm³), the right graphs highlights the peaks of density abundance (0.1 g/cm³) at 1.95 and 2.25 g/cm³.

down the Akamatsudani and Oshigadani valleys. Outcrop conditions were very good in the lower parts due to sparse vegetation. Most of the reworking appeared to have been restricted to a large erosional channel (compare Oshigadani) that is crossing the valley in the middle part in southeasterly direction. The abundance of lapilli-sized particles was found to be highest in this valley and chunks of wood were abundant. As all of them were found to be carbonised exclusively on their bottom sides (due to the contact with hot BAF deposits), an in-situ position was assumed and accordingly proved the low influence of later reworking processes for large areas of the BAF deposits. Miyabuchi (1999) found chunks of wood in Akamatsudani valley and measured temperatures of 60 to 100 °C (December 1996) in proximal BAF deposits. Sebastian Mueller (pers. comm.) reported similar findings (wooden chunks exclusively carbonised at the bottom side) during a 2004 field campaign on Augustine volcano (Alaska, USA). As in Oshigadani Valley, a decrease in porosity with increased transport distance could be discerned. The mean density of 300 samples measured at ten MPs is 2.0 g/cm^3 (range is 1.3 to 2.5 g/cm^3). The density distribution was found to be bimodal with peaks at 1.95 and 2.25 g/cm^3, representing 80 and 20 %, respectively (Figure 16). The percentage of dense rock samples was found to be lowest in this valley.

- Akamatsudani Valley (MP 24 to 30):

This valley was affected by BAFs from 19 June 1991 on until 11 February 1995 (the very last BAF during this eruption). Dense vegetation and ongoing dam construction strongly influenced the MP locations. As a consequence, most of them had to be relocated from where they had been planned and ended up not covering a large portion of the primary depositional

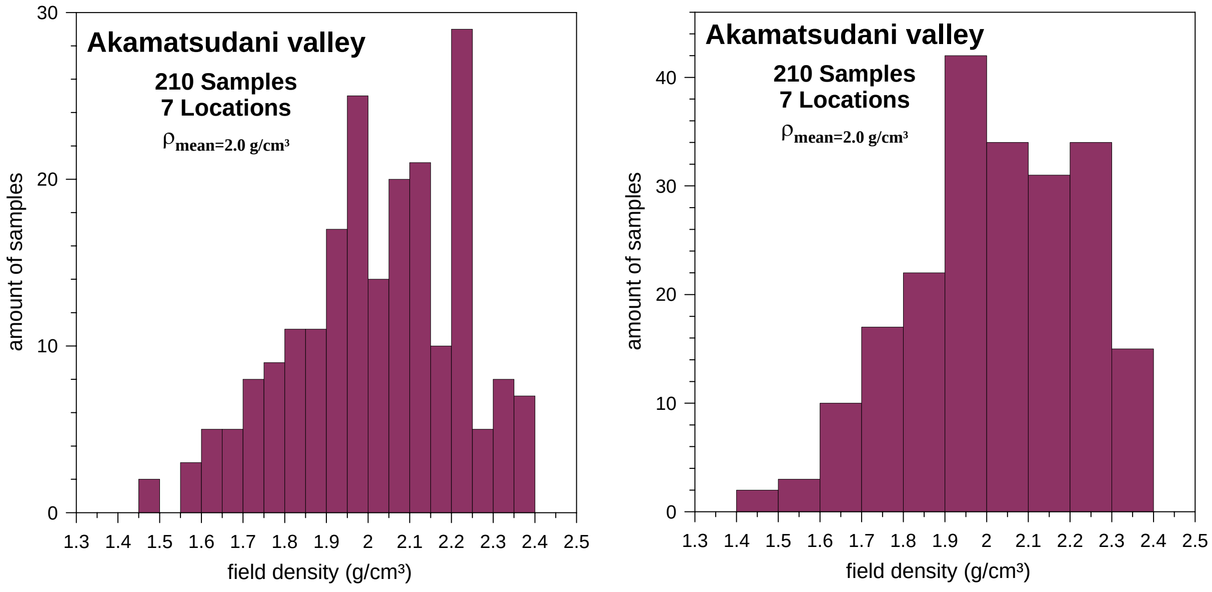

Figure 17: Plot showing the density distribution of 210 samples measured at seven locations in Akamatsudani valley. The left graphs shows the density at high resolution (0.05 g/cm^3), the right graphs highlights the peaks of density abundance (0.1 g/cm^3) at 1.95 and 2.25 g/cm^3.

area. Nevertheless, the results obtained in this valley showed a similar density distribution to the other valleys. Accordingly, the results were assumed to be reliable. 210 samples were measured at seven MPs and the resulting mean density was 2.0 g/cm³ (range is 1.6-2.4 g/cm³). The density was distributed bimodally with peaks at 1.95 and 2.25 g/cm³, representing 59 and 41 %, respectively (Figure 17).

- Dome talus (MP 12 and 13):

No measurements have been performed directly on the dome as access to the dome was restricted to overview surveys. As a consequence, measurements have been performed at two MPs at the western edge of the dome talus and revealed dense rocks to be the most abundant rock variety. The results confirmed visual estimations achieved on the dome during four ascents (see chapter II-3.1). No access was possible to the border areas or the inclined lobe 11B on the eastern flank of Unzen. 65 samples were measured with a resulting mean density of 2.2 g/cm³ (range is 1.9 to 2.4 g/cm³). The density distribution showed peaks at 1.95 and 2.25 g/cm³, representing 20 and 80 %, respectively (Figure 18). Bread crust bombs found west of the dome talus originated from the vulcanian eruption of 11 June 1991 and represented the least dense rock variety that could still be found (1.4 to 1.6 g/cm³).

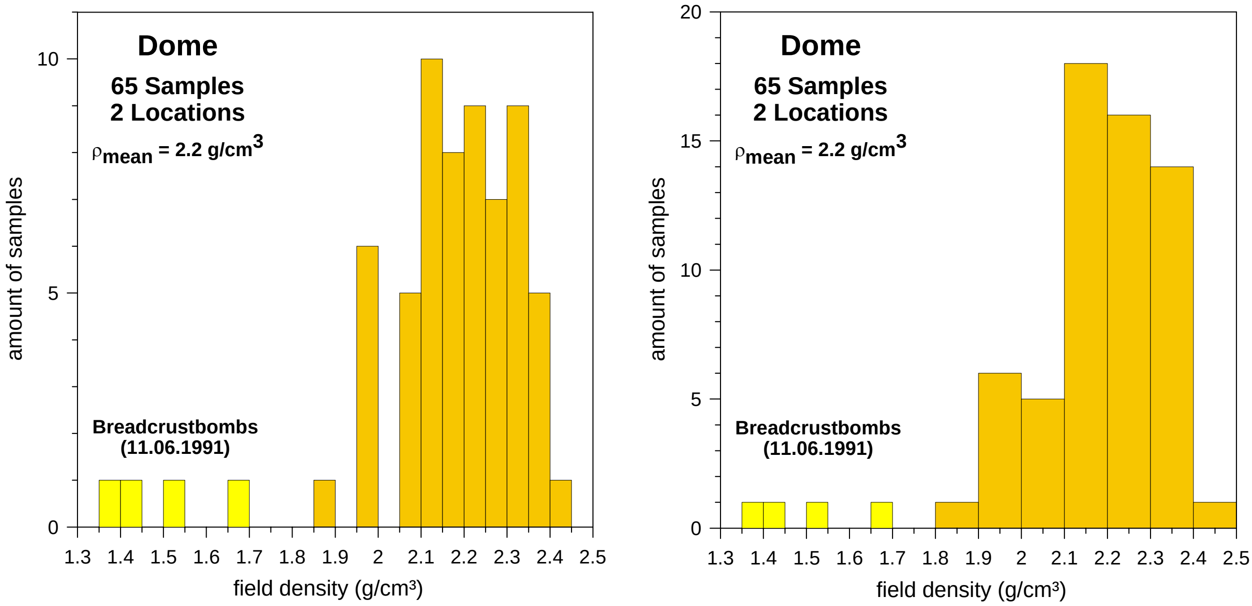

Figure 18: Plot showing the density distribution of 65 samples measured at two locations at the base of the dome talus. The left graphs shows the density at high resolution (0.05 g/cm³), the right graphs highlights the peaks of density abundance (0.1 g/cm³) at 1.95 and 2.25 g/cm³.

23 samples of the field measurements covering the whole density range were selected for correlation measurements in the laboratory. Rock cylinders (26 mm in diameter, up to 60 mm long) drilled from these samples were measured using a Micromeritics® 1330 Helium pycnometer. The results indicated that the matrix density, including closed porosity and crystals is in the range of 2.5 to 2.6 g/cm^3. The resulting range of open porosity was calculated to be 4.0 to 35.5 vol.%. Accordingly, the maximum difference between the field-based density measurements and the Helium pycnometry measurement (on a cylinder drilled from the respective clast) was calculated to be generally below 5 % (Figure 19). Thereby, the field-based density measurement method was found to be fast, effective and sufficiently precise to replace existing laboratory based techniques.

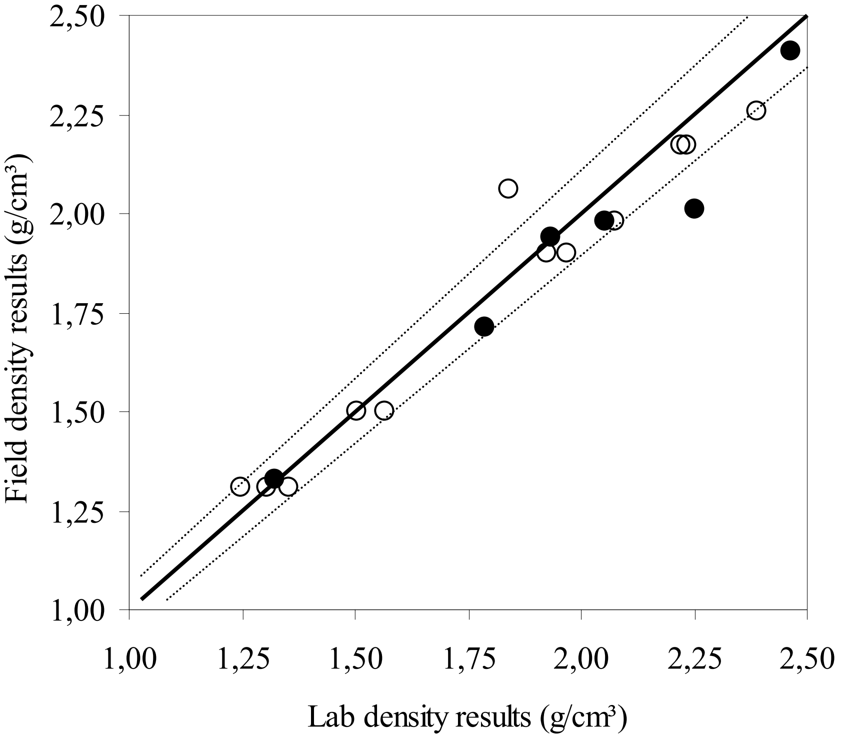

Figure 19: Laboratory vs. field results of density measurements from 2000 (full circles) and 2001 (open circles) samples. The results show a good agreement between the two data sets. Dashed lines mark the 5 % error line. 23 data points represent 96 correlation measurements.

4.5 Interpretation

Due to the large number of measurements performed at the 31 MPs, a good coverage of the deposits of the 1990-1995 Unzen eruption was achieved. All samples from within the four valleys belonged to deposits of BAFs that had been triggered by gravitational collapse of dome lobes. Based on the highest temperature measured at a fumarole on the dome, the temperature of the central zone of these lobes was not higher than 650 °C (Umakoshi et al., 1992). This temperature is below Tg (~ 715 °C, Marcel Potuzak, pers. comm.) and explains why no welded deposits have been found.

The density measurements in the lab showed good agreement with field data and thereby served as a good indicator of the method's validity and applicability (Figure 19). Different values of field and laboratory density probably resulted from different sample sizes (blocks in the field, cylinder drilled from blocks in the lab). The values achieved in the field included open and closed porosity; laboratory measurements via Helium pycnometry on cylinders evaluated the open porosity, on powder the closed porosity.

Taking the measured sample size as being representative for the density distribution within the deposits of the last Unzen eruption, an estimation of the porosity could be achieved. All five data sets (four valleys and dome talus) revealed a bimodal density distribution with similar peak values. This bimodal distribution matched closely with observed features in blocks on the dome and in the BAF deposits. Results from the Mizunashi valley differed from the results of the other valley data sets by exhibiting a higher abundance of porous rock varieties. The peak ratio ($80_{[porous]}:20_{[dense]}$) was found to differ from all other data sets found within the valleys (60:40). The Mizunashi valley was affected by BAFs only until mid-1993. According to Setsuya Nakada (pers. comm.), the density of erupted rocks had increased over the time span of the eruption. In the light of this statement, the Mizunashi data compared to the other three data sets is believed to show the shift in the density distribution from 1993 to 1995 and allow for a rough vertical resolution of the deposits. The peak ratio was constant (60:40) for Akamatsudani, Oshigadani, and Senbongi valley. All these areas have been affected until the end of the eruption. The ratio found at the base of the dome (20:80) represented the final stage of the eruption. The average density was highest there because samples investigated were associated with late-stage extrusion of dense degassed lava. A quantitative decrease of porous rocks with increased transport distance could be roughly discerned by comparing density distributions at locations parallel to the flow direction. As no correlation of the MPs with flow units was possible, it remained unsolved if this finding was due to preferential abrasion of weak clasts (i.e. the most porous ones) during transport or due to primary density distributions within different flow units. The degree of transport-induced abrasion has been investigated below (chapter III-7).

Although the last day of emplacement of a BAF in a single valley differed by more than 1.5 years (June 1993 in Mizunashi and February 1995 in Akamatsudani), constant peak values (though at changing ratios) could be found. It was accordingly assumed, that magma ascent mechanisms (except the ascent and extrusion rate) remained fairly constant throughout the run of the eruption. The density distributions in all valleys and the dome revealed bimodal distributions and reflected most probably the banding found in the dome and the spine. The internal structure of the spine and of many blocks found on the dome (Figure 10) or within the BAF deposits was found to be sheet-like with layers of different degrees of porosity. Layer thickness is in the cm to dm range.

Three reasons might have been responsible for heterogeneous porosity distribution:

- Syn-ascent mixing of two distinct dacitic magmas with different primary water content,
- Different time span available for degassing due to different ascent and extrusion rates, and
- Flow-controlled vesicle collapse.

Petrological investigations by Nakada and Motomura (1999) showed a constant main element composition of lavas erupted from 1990 to 1995, whereas the water content was decreasing continuously over the time span of the eruption. In slight contrast, melt inclusion analyses from Botcharnikov et al (2003) indicated complex pre-eruptive magma mixing at Unzen with three melts with different major element compositions and water contents. Close field investigations revealed that layers of different porosity exhibited a subvertical alignment in the spine as well as a flank-parallel alignment where dome lobes had been flowing down the eastern flank of Unzen. Smith et al. (2001) interpreted porosity heterogeneities as mostly flow-controlled. Extrusion rates were variable throughout the eruption and showed two major peaks (Nakada et al., 1999). This resulted in repeated shifts between endogenous and exogenous dome growth. Fast ascent rates were associated with high porosities as the influence of degassing was low (Nonaka et al., 2004). Nearly all Unzen lavas of the last eruption were found to exhibit low values of residual water content (Nakada et al., 1999). The latter two causes mentioned above did most probably have the strongest influence during the development of the porosity distribution found at Unzen (Mastrolorenzo et al., 2001). Explaining the found features as being magma ascent-related differs from the interpretation of Mt. St. Helens (MSH) deposits of Hoblitt and Harmon (1993). Looking at the "bimodal density distribution of cryptodome dacite from the 1980 eruption of Mt. St. Helens", they stated that the dense rocks represented the more degassed outer rim of the cryptodome and the more porous rocks the cryptodome interior. The discrepancy between these two interpretations likely reflected different emplacement processes (intrusive cryptodome at MSH and extrusive dome at Unzen with endogenous and exogenous dome growth).

The set-up designed to perform field-based density measurements has been successfully used on deposits of Unzen volcano. The results were evaluated to be reliable and statistically significant. Wind and clast humidity were found to be the most problematic parameters. As of July 2005, this method has been used for further field campaigns on Augustine (USA), Bezymianny (Kamchatka), Colima (Mexico) (Mueller et al., 2005), Anak Krakatoa, Kelut, and Merapi (all Indonesia).

4.6 Summary

The density distribution inside a dome and the upper part of the conduit is crucial to the eruptive style of an explosive volcano. This information cannot be collected during an ongoing eruption but is important for future hazard assessment via modelling conduit flow and dome collapse/explosion behaviour. Therefore, the percentage of the mass fractions of all rock types in the primary and secondary volcanic deposits must be evaluated. For this purpose and at the lowest logistic effort, field-based density measurements have been performed on Unzen volcano, Japan. The resultant density distribution was found to be generally bimodal at constant peak values but changing peak ratios. The most abundant rock types at Unzen exhibited an open porosity of 8 and 20 vol.%, respectively. The porosity was found to be arranged in layers of cm- to dm-scale that were oriented subparallel to flow direction, i.e. subvertical within the conduit and flank-parallel within the dome lobes. The achieved results allowed for an internal picture of the dome during the last eruption of Unzen volcano. The evaluated picture of the density distribution within the uppermost parts of the conduit and the dome itself allowed for insights into and a better understanding of magma ascent and degassing conditions at Unzen volcano during its last eruption. Knowledge of the density distribution is additionally required to draw conclusions from the results of laboratory investigations on the fragmentation behaviour to the monitored behaviour of Unzen volcano during its last eruption (see below).

Field based density measurements

III Laboratory work

5 Sample characterisation before fragmentation

All Unzen samples were taken in 2000 and 2001 from BAF deposits of the last eruption (1990-1995) and vulcanian deposits of 11 June 1991 close to the dome. Extensive fieldwork revealed that the sample's physical properties had not changed measurably during the BAF transport or after deposition (Kueppers et al., 2005). In contrast to sampling on the dome, the collected BAF deposits have not been subject to hydrothermal alteration due to latent heat and/or exposure to fumarolic activity. Samples of the drill core that had penetrated the Unzen conduit in 2004 (i.e. less than 10 years after the end of the eruption) revealed strong alteration (Nakada et al., 2004). Each Unzen sample name consists of two digits and one letter. The digits indicate the year of sampling, i.e. "00" samples have been sampled in 2000. Every letter stands for a sample of different porosity; "A" samples label the densest sample set. All bread-crust bombs derive from the 11 June 1991 vulcanian eruption and have been named BKB (abbreviation of the German word Brotkrustenbombe) without indicating the campaign's year.

For the investigation of the fragmentation behaviour, samples of three more volcanoes have been analysed to enlarge the range of open porosity and chemical composition of the samples used. The Montserrat samples have been collected by Dr. Oliver Spieler in 2002 in Belham valley and derive from vulcanian eruptions in summer 1997. The Mt. St. Helens (MSH) sample used is identical to the one used by Spieler (2001) and derives from the cryptodome of the 18 May 1980 eruption. The "Biondo" sample (golden pumice) of Stromboli originates from the 5 April 2003 paroxysm. The "Bruno" sample of Stromboli represents the typical ejecta. Both samples have been collected by Dr. Jacopo Taddeucci shortly after the paroxysm. In this study, the latter three sample sets have only been characterized for their open porosity.

For a petrological description of the samples used see Anhang 1.

Thin sections:

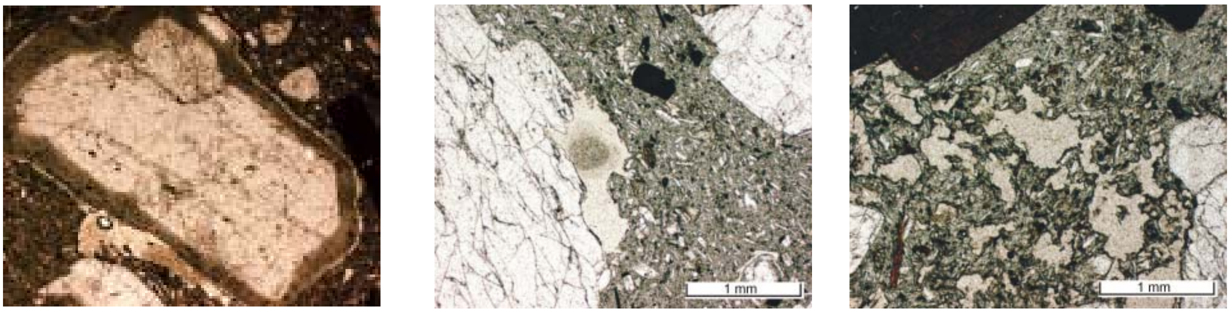

Figure 20: Thin section images of Unzen dacite rocks. Left (a): Rim indicating the disequilibrium of this plagioclase phenocryst with the surrounding melt. Middle (b): Internally fractured plagioclase crystals in a holocrystalline groundmass. Right (c): The bubble interconnectivity is very high in porous samples. Bubble shape is accordingly very irregular. The matrix is very rich in microlites.

Approximately 40 thin sections of Unzen samples covering the whole porosity range have been investigated for bubble and phenocryst textures. 50 % of the thin sections were oriented vertically whereas 50 % were oriented parallel to flow alignment. No statistically relevant petrographic investigation has been performed in this study as this had been the subject of research by Nakada et al. (1999). Phenocrysts were found to be aligned parallel to flow direction and the orientation of the long axes showed a maximum range of approximately 20 degrees. Microlites and bubbles were generally oriented parallel to the long axis of the phenocrysts. In the pressure shadow of phenocrysts or xenoliths, the orientation of microlites and bubbles was seen to deviate by as much as 70 degrees. Abundant phenocrysts of plagioclase and hornblende were exhibiting idiomorphic shape and were up to 20 mm long. Nearly all of them showed reaction rims of either resorption or late-state rim-growth with different chemical composition, indicating that the phenocrysts were in chemical disequilibrium with the surrounding melt (Figure 20 a). Most phenocrysts or their fragments exhibited internal fractures without single fragments having been moved apart (Figure 20 b). Several phenocrysts had pieces broken off and it was usually not possible to identify individual fragments and reassemble them. As no clustering of fragments or fractured phenocrysts has been observed, variable local strain is unlikely to have been responsible for these two features. It seemed more likely that two distinct events caused 1) some phenocrysts to break and the fragments to be moved apart and 2) the phenocrysts or their fragments to be fractured without the fragments being moved apart. If so, the relative timing of these two processes is clear with the crystals breaking being the first process. The matrix was mostly fully crystallised (holocrystalline) with mostly plagioclase (up to 250 µm long) (Figure 20 c). On a DRE basis, the matrix crystallinity was noted to be fairly constant throughout samples of varying porosity. All samples exhibited non-spherical bubbles with microlites having heavily deformed the bubble walls. In dense samples, many bubbles were found adhered to the phenocrysts, capable of reaching their length. With increasing porosity in dome-forming samples, bubbles size and thereby the interconnectivity tended to increase. Bread-crust bombs exhibited smaller bubbles than the most porous lavas but a higher bubble number density. Apart from the microlite content, it appeared to be obvious that the bubble shape was additionally influenced by syn-ascent shearing and/or partial bubble collapse upon effective degassing.

Porosity determination

The sampled blocks have been cut in slices and drilled. Drilling orientation was parallel to flow alignment to re-enact original orientation. Two kinds of density have been measured: 1) the "geometrical" density (ρ_{math}), calculated from the cylinder volume (Vol_{cyl}) and the weight, and 2) the matrix density, i.e. the density of the replaced volume ($Vol_{AccuPyc}$). The latter one is achieved in a Helium Pycnometer. A measuring cell of known volume is pressurised to a certain final pressure (P_1). From the sample weight and the equilibrium pressure (P_2) that is recalibrated after having opened the valve to a second (reference) cell at known volume, the matrix density including closed porosity and crystal content is evaluated. Measurements on Unzen cylinders revealed values in the range of 2.60 +/- 0.05 g/cm^3 for all dome-forming lavas and 2.23 +/- 0.03 g/cm^3 for bread-crust bombs. The resulting range of open porosity is calculated from the volume of the cylinder and the replaced volume according to

$$\Phi open = \frac{Vol_{cyl} - Vol_{AccuPyc}}{Vol_{cyl}} * 100 \qquad \text{Eq. 2}$$

It is in the range of 3.0 to 35.5 vol.% for lavas and up to 54.0 vol.% for bread-crust bombs. Representative sample material of each rock type was milled to < 10 µm and three to five Helium Pycnometry measurements have been performed with this powder. From this result ($\rho_{AccuPyc}$) and the geometrical density, the closed porosity could be calculated according to

$$\Phi closed = \left[\frac{\rho_{AccuPyc} - \rho_{math}}{\rho_{AccuPyc}} * 100 \right] - \Phi_{open} \qquad \text{Eq. 3}$$

It is generally below 2.5 vol.% for the dome-forming rocks. As expected, bread-crust bomb samples exhibited higher values of closed porosity, as high as 6.0 vol.%.

The “Biondo” sample of Stromboli exhibited an open porosity of 80.5 vol.%, the “Bruno” sample 47.5 vol.%. The MSH sample 36.0 vol.%, the dense Montserrat sample 3.1 vol.%, and the Montserrat pumice 68.8 vol.% (Table 1).

Bubble distribution

In natural lavas, bubbles will not be distributed evenly in any case and on any scale. On the scale of the dome or large blocks within the BAF deposits, the bubble distribution was clearly heterogeneous and layers with different degrees of porosity alternated in a layer-like structure. On the scale of the samples measured in the field (< 20*20 cm), these layer-like structures could still be seen in few samples. For the field-based density measurements, these samples have not been chosen as they would have delivered a “mix” density. Bubble distribution in the investigated thin sections (2 D) was found to be mostly homogeneous. In order to investigate the 3D bubble distribution, some measurements of the cylinders have been performed with computer tomography (CT) with Mrs. Silke Hecht (Tiermedizinische Klinik, LMU München) and Dr. H. Zeitler (Radiologisches Zentrum München-Pasing). This technique calculated the 3D-image from a series of pictures taken at a certain step width. Two factors are important for the analysis: 1) small step width (at best below 0.5 mm) and 2) high resolution of the images. The amount of measurements was limited but indicated a homogeneous bubble distribution on the size scale of a 26*60 mm cylinder. A limiting factor for the investigation of the bubble distribution by CT method remained the picture resolution (approximately 1 mm for the used machines). In order to address this question more in detail and evaluate the distribution of either bubbles or phenocrysts, measurements are planned together with Dr. Burkhard Schillinger and Mr. Johannes Brunner (Technische Universität München) at the new neutron source FRM-II. Only preliminary results on Unzen cylinders could have been achieved as this neutron source did only start working in 2004. These results indicated the feasibility of bubble distribution analysis with the described technique.

Surface analysis

Surface analysis was performed via Argon adsorption in a Micromeritics® Gemini 2375 (Figure 21) and the specific surface area was determined using the BET method. Argon instead of Nitrogen was used as adsorptive gas because in that way the precision of measurements on samples exhibiting small surfaces was higher due to its smaller molecular dimension (Scheu, 2005). This technique is a relative measurement between a reference and a sample tube. Three types of tubes have been used:

- Standard tube, straight: 0.75 cm inner diameter, 15.5 cm length, 6.5 cm³ volume with a maximum sample capacity of 2 cm³
- Standard tube (1) with bulb at the base: bulb dimensions: 1.7 cm inner diameter, 3.8 cm length, 12.0 cm³ total volume with a maximum sample capacity of 6 cm³
- Large tube: ~2.6 cm inner diameter, 14.5 cm length, 77.0 cm³ volume with a maximum sample capacity of approximately 20 cm³

Tubes (1) and (2) can be directly fixed to the machine and have been used to measure the surface of the artificial pyroclasts (see below). Whether a bulb tube is required as reference tube or not depended on the amount of sample material. The sample cylinders have been measured in the large tube (3), for which a special adapter is required, and a bulb tube as

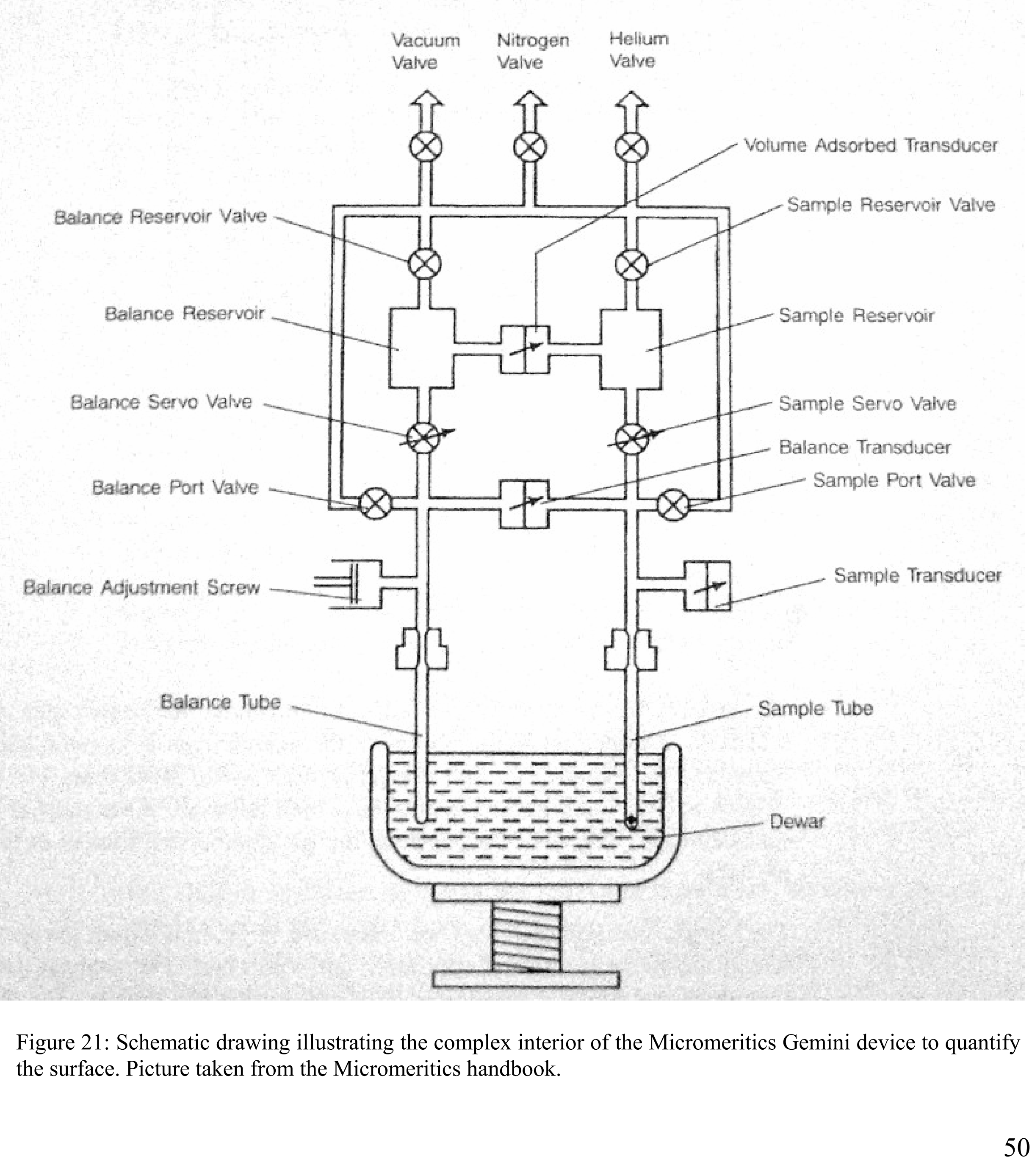

Figure 21: Schematic drawing illustrating the complex interior of the Micromeritics Gemini device to quantify the surface. Picture taken from the Micromeritics handbook.

reference tube. Prior to the measurements, the hot samples, dried in a vacuum furnace at 200 °C, were attached to the Gemini. When two tubes of different volumes were used, either massive or evacuated glass rods and/or additional glass beads were used to minimize the differential volume. As no adsorption is supposed to take place on ideal glass surfaces, the amount of gas adsorbed on the tube walls, the filler rods and/or the glass beads was assumed to be negligible.

At the beginning of each measurement, the reference and the sample tubes were evacuated and immersed into a dewar filled with liquid nitrogen (77 K). The internal volume and the cryogenic temperature surrounding both tubes were kept stable throughout the complete measurement. The different volumes of the reference and the sample tubes (with the sample therein) were determined using Helium 5.0 that is not adsorbed at these conditions. After another evacuation procedure, Argon 5.0 was added in both tubes. The gas was assumed to be adsorbed as a monolayer on any free surface (i.e. all outer sample surfaces plus any bubble/fracture surface of the open pore space). Accordingly, the pressure tended to decrease in the sample tube. A differential pressure transducer recorded the beginning imbalance between the two tubes and caused a servo valve to open, let more gas into the sample tube and maintained the pressure balance between the two tubes. Ideally, the Argon pressure over the sample was kept stable. This could have been achieved when delivery and adsorption rates were equivalent. The amount of adsorbed Argon was determined at nine relative pressure steps. From the total amount of Argon dispensed, the previously evaluated tube volumes, and the sample weight, the specific surface area (m^2/g) represented by the sample was calculated.

Several cylinders of each set of samples have been measured to determine the pre-fragmentation surface, usually using cylinders of 30 mm length (Scheu, 2005). The length reduction of the cylinders was necessary to guarantee thermal equilibrium of the sample as the large heat capacity of the 60 mm long cylinders caused the liquid nitrogen to fade away before the end of the measurement. The specific surface area before fragmentation (As_{spec}) multiplied with the weight of the cylinder (m_{cyl}) yields the pre-fragmentation cylinder surface (As_{cyl}).

$$As_{cyl} = As_{spec} * m_{cyl} \qquad \text{Eq. 4}$$

This surface value was compared to the surface values achieved for the experimentally derived pyroclasts. By comparing these two values, the surface area generated by the fragmentation experiment can be evaluated (see below).

6 Fragmentation behaviour

Volcanic eruptions and their style are influenced by many different parameters, such as melt composition, initial volatile content, magma ascent rate and volume, and style of degassing. Although the influence of many factors can nowadays be pinpointed fairly precisely, a complete and generally accepted picture of the physical processes during magma fragmentation is still missing. It remains unanswered as to what degree the fragmentation is influenced by brittle or ductile processes. Fragmentation is called “brittle” when stress around the bubbles exceeds a critical value and “ductile” when the gas volume fraction exceeds a critical value and the thin magma film becomes unstable.

6.1 Investigation of the fragmentation threshold

6.1.1 Introduction

Sparks (1978) defined a fragmentation criterion based on the closest possible packing of undeformed bubbles. Other studies based on density measurements of pumices revealed porosities as high as 90 vol.% (Sparks et al., 1994; Gardner et al., 1996). As pyroclasts may exhibit every possible value of porosity, this can not be the only parameter controlling or influencing the magma fragmentation. McBirney and Murase (1970) suggested that gas overpressure in bubbles and the magma’s tensile strength influence the formation of pyroclastic rocks. Dingwell (1996, 1998) evaluated the viscoelastic properties of magma and showed that any liquid will break if the applied stress is too high to be compensated by elastic deformation and too rapidly applied to be compensated by viscous deformation. Papale (1999) modelled the onset of magma fragmentation as a consequence of high acceleration rates upon bubble growth and magma rise. Sparks et al. (1994) and Alidibirov and Dingwell (2000) stated that for the case of brittle fragmentation in conduits or domes, internal overpressure is more than likely the main driving force with the tensile strength playing a minor role. Alidibirov (1994) and Zhang (1999) examined the stress distribution in the walls of spherical bubbles depending on bubble wall thickness and estimated the maximum gas pressure that gas bubbles in silicate melts may withstand before failure. Mungall et al. (1995) stated that the stress will be heterogeneously distributed in bubbles that exhibit a non-spherical shape due to shear-induced deformation or high crystal content. They assumed that the stress exerted by the gas overpressure might locally increase due to stress concentration where the bubble wall curvature radius is smallest.

As it will most likely remain impossible to investigate syn-eruptive processes in a volcanic edifice on-site, enhanced understanding can only be achieved by a combination of detailed textural analyses of the eruptive products and laboratory experiments or modelling. Many experimental approaches use analogue materials (e.g. Taddeucci et al., 2004; Ichihara et al., 2002; Mader et al., 1996) or powders (Cagnoli et al., 2002). The applicability of these results to "real" magma fragmentation needs to be analysed as these experiments (usually at ambient temperature) simplified the natural process by having avoided complexities as e.g. crystals, changing viscosities. The approach of Ichihara et al. (2002) was very close to the gas-overpressure driven magma fragmentation from the physical point of view. They used a viscoelastic material with a known porosity that became rapidly decompressed. Taddeucci et al. (2004) rapidly decompressed Argon-saturated Silly Putty© and thereby simulated simultaneous bubble nucleation and bubble growth that might lead to fragmentation. Mader et al. (1996) mixed two chemically reacting liquids and investigated bubble nucleation and growth. Cagnoli et al. (2002) rapidly decompressed fine powders to shed light on the dynamics of gas-particle flows in volcanic conduits.

Alidibirov and Dingwell (1996, 2000) designed and further developed the fragmentation bomb, an experimental set-up that allowed investigating the fragmentation of natural samples upon rapid decompression of internal gas pressure. These experiments advanced the current understanding on magma fragmentation and the adjacent physical processes. However, due to the heterogeneous nature of natural samples, it remained difficult to actually evaluate the influence and importance of a single physical process or textural feature. Nevertheless, this approach opened the possibility to draw conclusions from the laboratory to the "real" world. Results of Spieler (2001) from experiments on 50*17 mm samples of nine sets of samples from Merapi (5), MSH (1) and Unzen (3), indicated a close relationship between open porosity and the overpressure required to completely fragment the samples (fragmentation threshold).

6.1.2 Sample description

Based on these results, experiments of this study intended to enlarge the range of open porosity and chemical composition and evaluate the relationship between open porosity and the fragmentation threshold (ΔP_{fr}) more clearly. In this purpose, a series of experiments was performed on eight sets of samples with varying porosity from the 1990-1995 Unzen eruption, two sets of samples from Montserrat, one of MSH and two of Stromboli (Table 1). Two of the Unzen sample sets exhibited similar values of open porosity to samples investigated by

Spieler (2001). These Unzen and the MSH samples have been analysed to check if the sample size had a measurable influence on the fragmentation behaviour.

Sample origin	Cylinder diameter (mm)	Experimental temperature (°C)	Open/total porosity (%)	Achieved fragmentation threshold (MPa)
Unzen (00 A)	26	850	3.80/4.40	22.5
Unzen (01 B)	25	850	5.70/6.00	20.0
Unzen (00 B)	26	850	11.90/14.50	9.0
Unzen (00 E)	26	850	14.10/16.60	6.5
Unzen (01 C)	25	850	20.45/21.30	5.8
Unzen (00 G)	26	850	34.30/35.60	5.5
Unzen (00 F)	26	850	33.60/36.00	3.5
Unzen (BKB)	25	850	53.90/59.90	4.1
Stromboli (Biondo)	25	850	80.50/81.20	7.5
Stromboli (Bruno)	25	850	47.50/48.30	4.2
MSH (crypto dome lava)	25	850	36.00/41.00	5.0
Montserrat (dome lava)	26	850	3.10/4.10	31.0
Montserrat (pumice)	26	850	68.80/73.40	3.2

Table 1: List of samples used for the investigation of rapid decompression induced fragmentation.

To investigate the influence of heating and pressurisation on the samples used, experiments identical to the fragmentation experiments in terms of heating and pressurization have been performed. Instead of rapidly decompressing and thereby fragmenting the sample, the furnace was switched off and the sample was slowly decompressed. Sample dimensions, weight, and open porosity were observed to have not changed measurably.

The glass transition temperature for glassy samples (quenched from 1500 °C) was determined to be 712 °C at a heating rate of 5 K/min. and 720 °C at a heating rate of 20 K/min.. The viscosity at the experimental temperature was evaluated by micropenetration and noted to be approximately $10^{11.6}$ (using a natural sample) or $10^{8.1}$ using a glassy sample (Marcel Potuzak, pers.comm.). The latter value was obtained from TVF (Richet and Bottinga, 1995) and Avramov (1994) fits.

Static fragmentation tests have been performed on 160*40*40 mm sample prisms of two sets of samples of Unzen (01 A and C) and Colima (Mexico) volcanoes. The Colima samples have been collected by Sebastian Müller and Dr. Oliver Spieler in March 2004. The open porosity is approximately 20 and 30 vol.%, respectively.

6.1.3 Experimental procedure

1. Rapid decompression experiments:

Fragmentation experiments were performed in the fragmentation bomb (Alidibirov and Dingwell, 1996) modified as described by Spieler et al. (2004) (Figure 22a, b). It is a shock tube type apparatus that permits simulation of volcanic conditions in terms of temperature, gas overpressure, and rate of decompression. In this study, it was used to quantify the effect of porosity on the fragmentation behaviour upon rapid decompression. The modified experimental set-up consists of three main units:

- A low-pressure tank (inner dimensions: d=40 cm, l=300 cm) at ambient pressure where the experimentally generated pyroclasts collected.
- A pressurization system with up to three diaphragms, each of which opens at a relative pressure differential. Diaphragms are discs (d=5.0 cm) of iron or copper with a thickness in the range of 0.3 to 1.0 mm. They have a circular (d=3.0 cm) and a cross imprint. The pressure differential that a diaphragm can withstand depends on the imprint depth, the material, and the diaphragm holder and decreases with increasing imprint depth.
- A high-pressure steel autoclave (l=45.0 cm) separated from the low-pressure tank (1) by the diaphragms (2). The autoclave's inner dimensions are asymmetrical with a larger centred drilling in the upper part (d=2.8 cm, l=25.0 cm) and a narrower one at the bottom (d=1.0 cm, l=20.0 cm). The sample is located at the base of the upper part. The pressure vessel was heated externally with a Linn® furnace.

This set-up allowed for a precise and reproducible pressurization of the sample. All experiments were performed at 850 °C. This temperature was estimated to be the temperature of the Unzen magma after mixing (Venezky and Rutherford, 1998). Samples were drilled parallel to flow alignment to re-enact their original orientation in the conduit. By applying realistic values of temperature and pressure to samples of the above described kind, a realistic approach to simulate magma fragmentation due to rapid decompression was obtained. Usually, sample size should exceed the phenocryst or bubble size by a factor of 10 to exclude an „overburden influence" of crystals or bubbles. Within the outer dimensions of the used autoclave, the chosen samples size (d=26.0 mm, l=60.0 mm) was the best possible compromise.

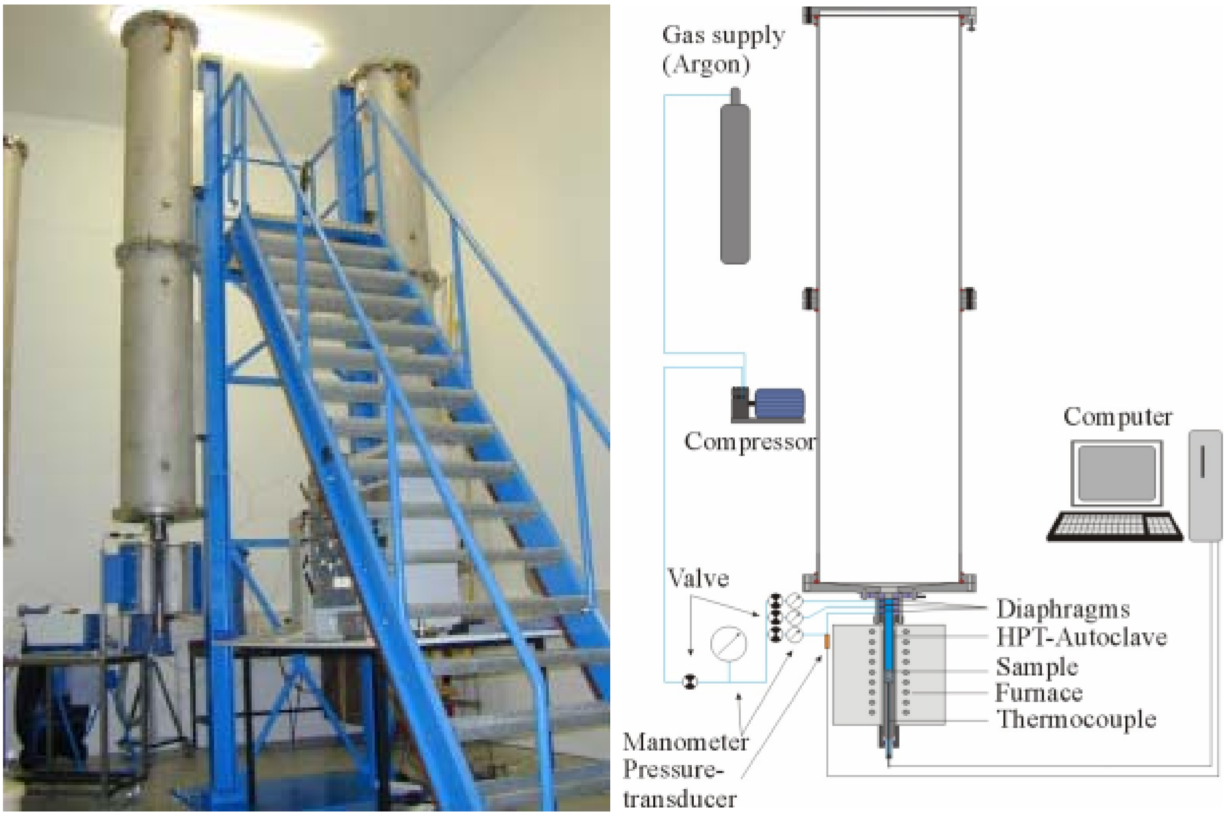

Figure 22: A) picture of the “fragmentation bomb”. B) Schematic drawing of the fragmentation bomb.

Each sample was pressed by hand into a steel sample container (type SC-A, d=26.1 mm, height=62.5 mm) after adding a two-component high-temperature cement (Haldenwanger®) on the cylinder and sample container wall. This gluing procedure usually allowed for a fixed sample position upon decompression. Heating was performed at a rate of ≈15 K/min up to 850 °C. This temperature was approximately 130 K above the glass transition temperature. At the final experimental temperature, the sample was slowly pressurized to the desired experimental pressure. The overpressure was applied by adding gas from outside. Consequently, this pressurisation did only affect the open porosity, i.e. all kinds of cavities that were accessible from the cylinder surface. In order to avoid heating induced changes of the physical properties of the sample and sample alteration, it was pressurized to 2 MPa with Argon 4.8 before heating. Comparative studies on sample cylinders and sample powder ($x < 10$ µm) revealed that the degree of closed porosity was minor (at most 2.5 vol.% for Unzen dome lava samples) and therefore did not effectively contribute to the sample fragmentation and its behaviour. Considering the short residence time at the final temperature, the gas-pressurised bubbles, and the determined high viscosity, no change in the sample shape or in porosity was observed. The majority of experiments in this study was conducted on eight sets of Unzen samples with values of open porosity in the range of 3.8 to 53.0 vol.%

(Table 1). Approximately ten experiments were performed for each sample set to precisely define the fragmentation threshold (ΔP_{fr}), i.e. the minimum pressure differential required to completely fragment a sample. As such, the applied pressure was raised stepwise in subsequent experiments in steps of 2.5 MPa until the first fragmentation occurred. If a sample was fragmented completely, another experiment was performed at approximately 1 MPa below the pressure of the previous experiment. If the sample had been partially fragmented, the applied pressure of the next experiment was increased by 1 MPa. In that way, ΔP_{fr} could be evaluated with a precision of approximately 0.5 MPa. Repetitive experiments confirmed the achieved values of ΔP_{fr} within this error range. Further investigations, though with a lower number of experiments, have been performed on samples from Stromboli, Montserrat and MSH. The achieved values of ΔP_{fr} have been combined with data from other samples and yield a comprehensive study on the relationship of overpressure, open porosity and fragmentation behaviour (Spieler et al., 2004).

Half a dozen of experiments were performed with a modified sample container with an inner diameter size reduction at the top (inner diameter of the top 1 mm was 24 mm). The aim of this changed set-up was to investigate the influence of wall friction on the fragmentation behaviour and evaluate the nature of the fragmentation process.

2. Static fragmentation tests:

As the fragmentation experiments in the fragmentation bomb are not calibrated according to any industrial norm, few indirect tensile failure experiments have been performed together with Mr. Wolfgang Bögl (Materialprüfungsamt, TU München) according to DIN EN 1015-11:1999/8 using a static material-testing equipment (Figure 23, Toni Technik®). Sample length was 160 mm, height and width 40 mm, respectively. The prism has been placed on two static bearing edges (distance 100 mm). A punching tool of a hydraulic system applied a controlled stress [0.5 kN/(mm²*s)] on the prism surface. Time until sample failure and the applied force at failure (kN) have been recorded and the resultant sample strength (N/mm²) was calculated.

Figure 23: Device as used for the static fragmentation tests with Mr. W. Bögl of the Materialprüfungsamt in Munich. The sample is placed on two static bearing edges and loaded by a hydraulically controlled punching tool from above. (picture credit: Wolfgang Bögl)

6.1.4 Results

1. Rapid decompression experiments:

In some decompression experiments, the sample cylinder had been moved upwards “en bloc” and got stuck in the upper parts of the autoclave or the diaphragm assemblage. As a first approach to avoid this, the hollow steel rod below the sample with a thermocouple therein was replaced by a massive one in order to minimize the amount of pressurised gas below the sample and avoid the sample to be rocketed out by this gas volume. Consequently, the temperature of the sample could only be controlled with the thermocouple of the furnace. To ensure constant experimental temperatures, the temperature gradient through a specially prepared sample at ambient pressure was investigated several times during the time span of this study. It was found that the furnace thermocouple was sufficiently and constantly precise and that the maximum gradient between the centre of the sample and top and bottom, respectively, was approximately 15 to 20 K. The gradient was 2.5 K for each 5 mm below the sample centre and 3 K for each 5 mm step in the lowermost centimetre of the sample. By minimizing the gas volume below the sample, experimental failure due to en-bloc movement of the samples was mostly avoided. In general, the above described change in set-up fulfilled its purpose. However, some dense samples were still being moved-up en bloc simply by the momentum of the pressure unloading. To avoid this, a special, modified sample container (diameter reduction at the top, type SC-B) was designed. The experiments revealed that the

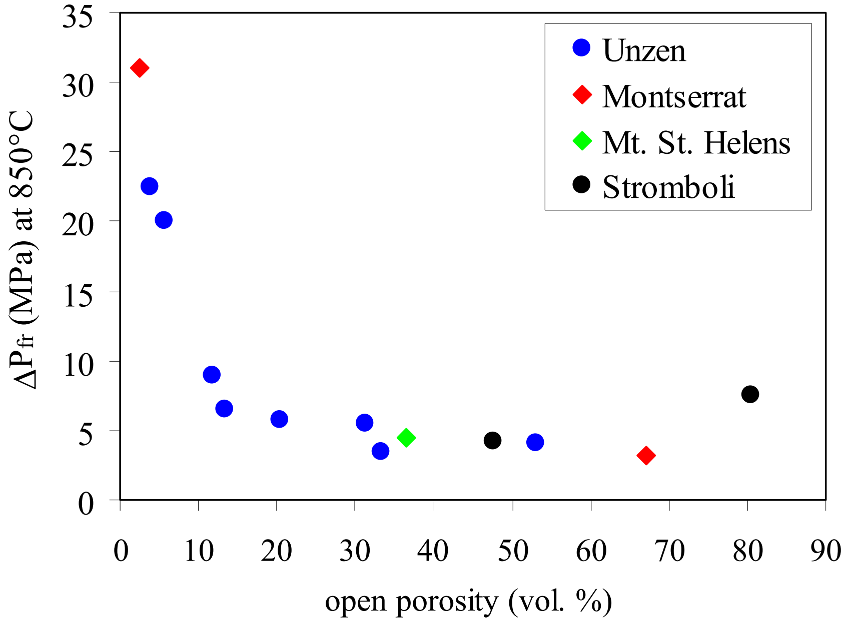

Figure 24: Plot of fragmentation threshold (ΔP_{fr}) against open porosity. A non-linear dependency is clearly visible.

diameter reduction had a major influence on the fragmentation behaviour. Even if experiments were performed at initial pressure conditions at up to 5 MPa above ΔP_{fr} achieved with "normal" sample containers (type SC-A), the fragmentation was only partial. This finding had important implications for the interpretation of the fragmentation process.

In this study, ΔP_{fr} of eight sets of samples from Unzen, two of Montserrat, one of MSH and two of Stromboli has been quantified at 850 °C (Figure 24) using type SC-A sample containers. In a plot of open porosity vs. fragmentation threshold (Figure 25, modified Figure 2 from Spieler et al., 2004), the data points of this study (red diamonds) that went into the publication "The fragmentation threshold of pyroclastic rocks" (Spieler et al., 2004) can be seen in the context of all investigated samples (black spheres). The evaluated threshold values can be seen in Table 1 and showed a non-linear decrease with increasing open porosity. The open porosity seemed to have a major influence on the fragmentation behaviour in gas overpressure-driven volcanic eruptions upon rapid decompression. However, some samples with high values of porosity exhibited unusually high values of ΔP_{fr} (Stromboli, Campi Flegrei).

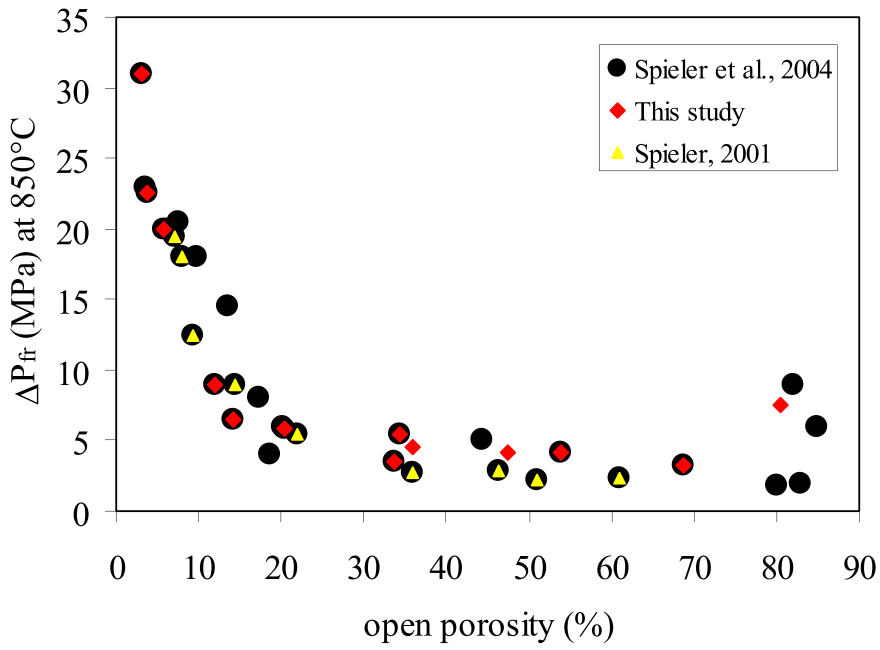

Figure 25: (modified from Spieler et al., 2004) Plot showing the dependency of the fragmentation threshold to open porosity. Yellow triangles indicate results of Spieler (2001), red diamonds the values achieved in this study.

A comparison of ΔP_{fr} values at 850 °C (this study) and at ambient temperature (Scheu, 2005) for 60*26 mm samples of Unzen revealed fairly constant values for dense dome lavas (< 10 vol.% open porosity) and bread-crust bomb samples (54 vol.% open porosity). Samples that exhibited intermittent values of open porosity consistently showed a reduced fragmentation threshold at elevated temperature (Figure 26 and Table 2).

The values of ΔP_{fr} achieved by Spieler (2001) on 50*17 mm samples and Kueppers (this study) on 60*26 mm samples on three sample sets with comparable open porosity do not show a clear influence of the sample size. Two pairs of samples (ENSP/01 B [~ 7 vol.% porosity] and MUZD UI/01 C [~ 21 vol.% porosity]) revealed constant values, the sample set FD24693/00 E [~14.50 vol.% porosity] showed a fragmentation threshold reduction with increasing sample size (Table 2).

Sample		Diameter (mm)	$T_{experiment}$ (°C)	Porosity (%) Open/total	Threshold (MPa)
Unzen (FD24693)	Spieler, 2001	17	850	14.50/16.80	9.0
Unzen (ENSP)		17	850	8.00/8.60	18.0
Unzen (MUZD UI)		17	850	22.00/22.90	5.4
Unzen (00 A)	This study	26	850	3.80/4.40	22.5
Unzen (01 B)		25	850	5.70/6.00	20.0
Unzen (00 B)		26	850	11.90/14.50	9.0
Unzen (00 E)		26	850	14.10/16.60	6.5
Unzen (01 C)		25	850	20.45/21.30	5.8
Unzen (00 G)		26	850	34.30/35.60	5.5
Unzen (00 F)		26	850	33.60/36.00	3.5
Unzen (BKB)		25	850	53.90/59.90	4.1
Unzen (00 A)	Scheu, 2005	26	22	5,50/6,20	23.0
Unzen (00 B)		26	22	11.90/14.50	8.5
Unzen (00 E)		26	22	14.10/16.60	8.5
Unzen (01 C)		26	22	20.45/21.30	10.5
Unzen (00 G)		26	22	34.30/35.60	7.0
Unzen (00 F)		26	22	33.60/36.00	8.0
Unzen (BKB)		26	22	53.90/59.90	5.0

Table 2: Comprehensive list showing the fragmentation threshold results of Spieler (2001), Scheu (2005) and this study.

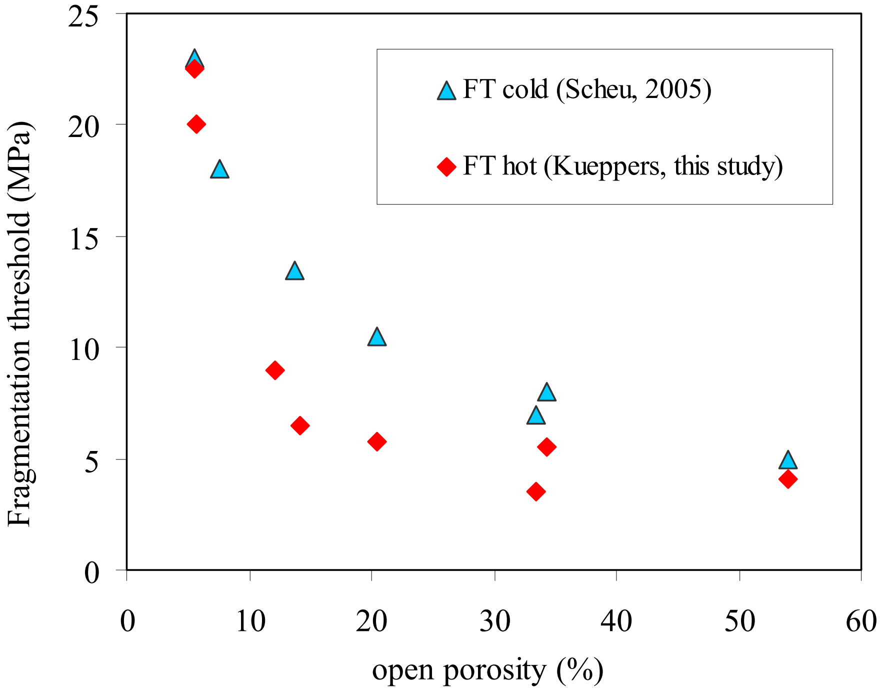

Figure 26: Plot showing the influence of the experimental temperature on the fragmentation threshold for samples from Unzen volcano. The deviation is highest for samples of 15 to 35 vol.% open porosity. Dense dome lavas and bread-crust bombs show consistent results.

2. Static fragmentation tests:

Thirteen flexible bending tests and three direct pulling tests have successfully been performed at ambient conditions. Due to the restricted amount of performed experiments, the results are of preliminary nature although indicating consistency. Generally spoken, a rock strength reduction with increasing porosity became obvious. Four out of five experiments on Unzen 01 A samples revealed consistent results. Only one experiment could be performed successfully for Unzen 01 C samples. Nevertheless, the indicated strength reduction of the latter sample due to its higher porosity was consistent with results of experiments on two sample sets of Colima. The flexible bending tests revealed lower yield strength compared to direct pulling tests. Phenocrysts in the Unzen samples seemed to have reduced the strength as they showed lower values than Colima samples at comparable porosity (Table 3). The yield strength is calculated in the same way as for dense concrete or granites, i.e. the area (thickness*width) has not been corrected for the porosity. The value of yield strength (N/mm^2) is directly comparable to the values of the decompression experiments (MPa).

sample name	run number	open porosity (%)	max. force (kN)	thickness (mm)	length (mm)	width (mm)	yield strength (N/mm^2)	
Unzen 01 A	1	7.0	0.955	39.8	160.0	38.8	2.51	flexible bending tests
	2	7.0	1.280	41.8	160.0	42.8	2.65	
	3	7.0	0.780	39.6	160.0	41.4	1.91	
	4	7.0	1.165	39.4	160.0	42.4	2.75	
	5	7.0	0.995	38.6	160.0	38.6	2.72	
Unzen 01 C	1	20.5	1.025	41.4	160.0	41.4	2.26	
Colima dense	1a	~ 20	2.206	41.4	160.0	39.5	4.49	
	2a	~ 20	2.338	42.3	160.0	40.4	4.85	
	3	~ 20	2.188	41.3	160.0	41.3	4.66	
Colima porous	1a	~ 30	0.486	40.3	160.0	42.1	1.06	
	1b	~ 30	0.655	40,0	160.0	41.8	1.47	
	2a	~ 30	0.889	41.1	160.0	41.8	1.89	
	2b	~ 30	0.299	40.4	160.0	41.7	0.66	
Colima dense	1b	~ 20	3.827	41.8	159.9	39.9	2.29	direct pull tests
	2b	~ 20	3.890	43.5	159.8	39.4	2.27	
Colima porous	3	~ 30	0.710	41.6	159.6	40.9	0.42	

Table 3: Results of static flexural tests with samples from Unzen and Colima volcanoes.

6.1.5 Interpretation

Density analysis of pyroclasts from explosive volcanic eruptions revealed that magma can be fragmented at nearly any value of porosity. The samples used in this study range from 3.0 to 80.5 vol.% in open porosity, chemically covered a wide field in volcanic rocks and showed that the chemical composition apparently has only a minor effect during the fragmentation process. The influence of the chemical composition on other physical or kinetic processes is beyond question. As illustrated in Figures 24 and 25, the overpressure required for full fragmentation (ΔP_{fr}) was found to be closely correlated with the open porosity and generally showed a negative relationship (Spieler et al., 2004). This trend may be roughly approximated by 1/x with x being the gas fraction. As some data points strongly deviated from the general trend, it was inferred that magma fragmentation is probably the combination of two or more simultaneously acting fragmentation mechanisms.

Influence of different fragmentation processes

The results shown above indicated that expanding gas is capable of magma fragmentation. However, it became likely that additional processes do exhibit an increasingly important influence on the fragmentation behaviour at low and high porosities.

Low porosities:

Results from experiments on dense samples revealed a strong increase in values of fragmentation threshold with decreasing porosity (Figure 24). Experiments were performed in a modified sample container (type SC-B). In that manner, the wall friction force was strongly increased from being simply represented by the cylinder wall (SC-A sample containers) to an additional one millimetre thick, circular obstacle at the top of the SC-B sample containers. In the latter case, the fragmentation behaviour was found to have completely changed. No complete fragmentation could be achieved even when applying values of up to 5 MPa above the fragmentation threshold. The bottom of the samples remained unmoved in all cases. It was suggested that fragmentation of dense samples in the fragmentation bomb was largely controlled by shear forces. These resulted from the momentum of the unloading decompression front on the sample (that tended to move and accelerate the sample upwards) and the counteracting wall friction (that acts to keep the sample where it is). This fragmentation process could be compared to shear-induced pyroclast formation as described by Papale (1999).

High porosities:

Figure 25 clearly showed that for samples of porosities > 35 vol.%, the fragmentation threshold values no longer adhered to a well defined trend but rather covered an area widening with porosity. Different sample sets of comparable porosity were found to exhibit completely different values of fragmentation threshold. One main difference between the sample sets was the bubble texture. The "Golden pumice" sample of Stromboli was found to exhibit unusually high values of ΔP_{fr} and thereby confirmed the results achieved with samples from the Campi Flegrei (Spieler et al., 2004). Both sample sets exhibited high values of porosity at low bubble number density but large bubble radii (type A samples) with adjacent high connectivity and exhibited values of ΔP_{fr} that were higher than expected. These samples showed an increasing fragmentation threshold with increasing porosity which in turn defined the upper border. The lower border of this field was defined by samples that followed the trend indicated by low-porous samples (e.g. Santorini). It may be approximated with 1/x with x being the gas fraction. Samples that showed this relationship of open porosity and ΔP_{fr} exhibited a high bubble number density with small bubble radii (type B samples). In porous samples, textural features (e.g. bubbles number, bubble ellipsoidity, bubble connectivity) could possibly have had a considerable influence on the fragmentation behaviour. Mueller et al. (2005) demonstrated that the gas permeability of volcanic rocks is dependent on 1) open porosity, 2) interconnectivity, and 3) predominant "shape" of the pore space (interconnected bubbles, fractures). In the case of type “A” samples, the pathway for volatiles was much bigger than in the case of samples with high bubble number density (type “B”) that exhibited lower values of permeability. As such, in order to cause full fragmentation of type “A” samples, higher values of overpressure (resulting in higher values of energy) needed to be applied, as this overpressure was efficiently reduced by permeable gas flow before and during the fragmentation process (Figure 27).

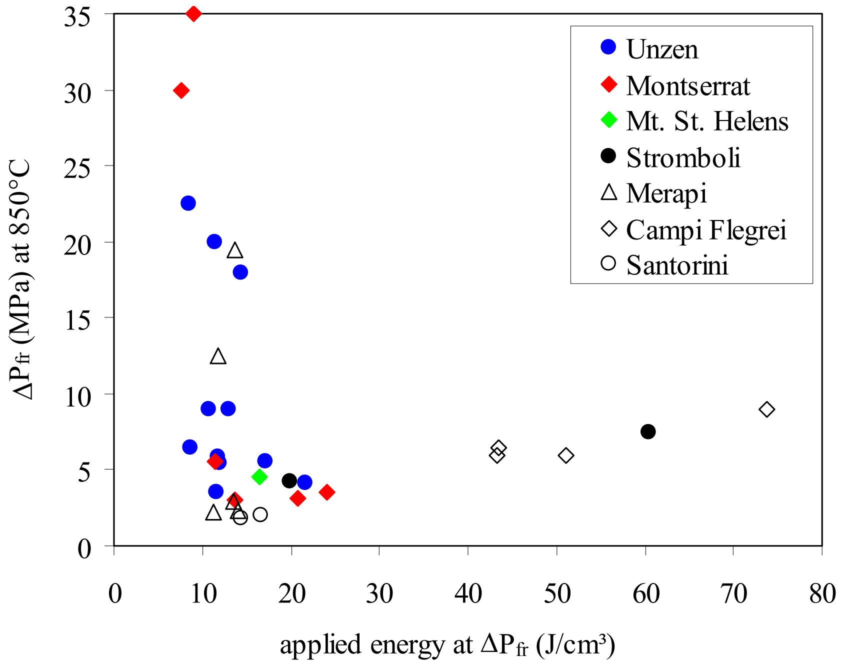

Figure 27: Plot of the applied energy (J/cm³) at the fragmentation threshold (MPa). The influence of gas loss by permeable gas flow is clearly visible. The Stromboli sample at ~60 J/cm³ exhibits comparable behaviour to samples from the Campi Flegrei. Both sample sets are characterized by large bubbles and proof the influence of permeable behaviour on fragmentation. Some samples at > 20 J/cm³ demonstrate the beginning influence of syn-fragmentation pressure reduction by permeable gas loss (Monterrat pumice, Unzen bread-crust bomb, Stromboli Bruno). Part of the Montserrat data was achieved by Ben Kennedy. The empty symbols refer to results achieved by O. Spieler (Spieler et al., 2004).

Comparison of experimental results with models

Several models have been tested so as to try and predict the overpressure required to cause magma fragmentation as a function of tensile strength (σ) for a given porosity (Φ). The tensile strength of a natural melt is influenced by several factors as e.g. 1) temperature, 2) melt composition, 3) porosity, and 4) phenocryst and/or microlite content. However, one of the limitations of the models is that they over-simplify the natural state of magma by assuming spherical bubbles in a glassy matrix. All models show their best fit to the experimental data for a different tensile strength (Figure 28). The best fit values have been evaluated using the program *TableCurve*, looking for the lowest value of the fit standard error. It is defined as the square root of the sum of the squared errors divided by the degree of freedom.

McBirney and Murase (1970) evaluated the critical tensile strength and the elastic modulus of the melt. As their model is based on the assumption of undeformed bubbles, it is unable to predict the fragmentation behaviour at $\Phi > 60$ vol.%. The fit of this model is fairly good for $\Phi < 35$ % when using a bulk tensile strength of 1.5 MPa.

The models of Zhang (1999) and Alidibirov (1996) considered the tangential stress distribution in the wall of one spherical bubble. Zhang examined the stress distribution throughout a thick bubble wall where the maximum stress is occurring at the inner bubble wall. At zero porosity, Zhang predicted a finite fragmentation threshold twice as high as the tensile strength. The modelled values more than likely represent the overpressure required to generate cracks. However, in dense samples with thick bubble walls, the stress required for crack propagation leading to full sample fragmentation (= fragmentation threshold) was probably higher than the stress required for crack generation. At some value of porosity, the stress required for crack generation will equal the stress required for crack propagation. At

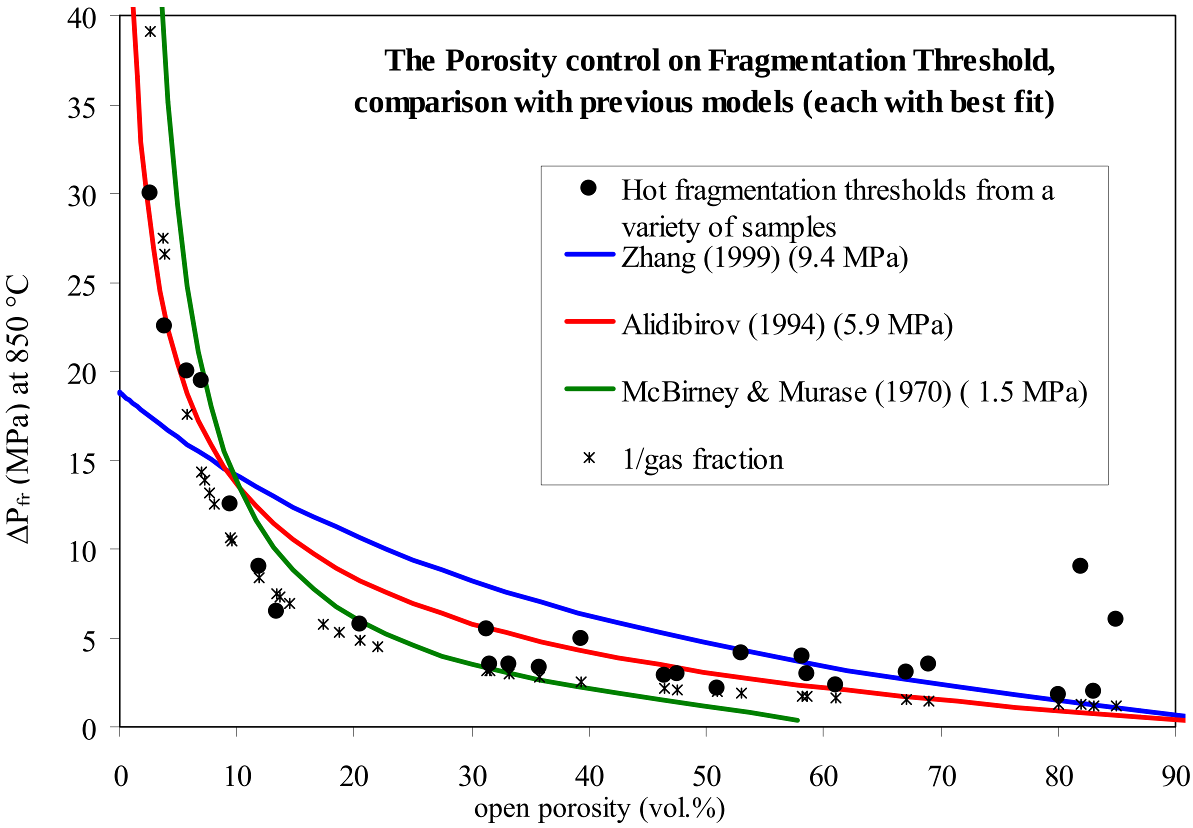

Figure 28: Plot of fragmentation threshold vs. open porosity showing the deviation of values predicted by various models even at the best fit (modified after Spieler et al., 2004).

high porosities, the calculated values of fragmentation threshold were nearly zero. This model assumed a continued strength reduction with increasing porosity. Zhang thereby ignored the fact that for certain bubble texture conditions the applied pressure may be effectively reduced by permeable gas flow. For a full fragmentation of samples of this kind, the initial applied pressure must account for and equal this pressure reduction. The degree of pressure reduction by bubble texture and interconnectivity can be clearly seen in Figure 24 and 27 and was shown by Mueller et al. (2005) for a broad variety of samples. It is therefore likely, that samples of intermediate porosity will exhibit the minimum fragmentation threshold. Zhang's model fits the experimental values achieved with the used set-up least well.

Alidibirov assumed an even stress accumulation through a thin bubble wall. The predicted values of tensile strength at zero porosity are several 100 MPa and are similar to values of tensile strength evaluated on glass fibres by Webb and Dingwell (1989). The best fit to the experimental results was found for a tensile strength of 5.9 MPa at $\Phi < 10\%$ and 30-65 %. As with the model of Zhang, the fragmentation threshold at high porosities is approaching zero and thereby underestimates the evaluated experimental results.

Influence of boundary conditions

Results of Spieler (2001) on one MSH, six Merapi, and three Unzen sample sets (50*17 mm) revealed a non-systematic influence of elevated temperature on the fragmentation threshold. Fragmentation experiments, both at ambient and elevated temperature, showed a clear influence of applied pressure and open porosity on the fragmentation behaviour. A comparison of fragmentation threshold values at 850 °C (this study) and at ambient temperature (Scheu, 2005) for 60*26/25 mm samples indicated fairly constant fragmentation threshold values for dense dome lavas (< 10 vol.% open porosity) and bread-crust bomb samples (54 vol.% OP). Samples that exhibit intermittent values of open porosity consistently resulted in a decreasing fragmentation threshold at elevated temperature. Physical properties (sample size, crystal content, porosity, pore interconnectivity) are insufficient to explain this differing behaviour, as experiments were performed on cylinders from identical blocks. The high decompression rate is unlikely to have been affected by temperature and will lead to brittle fragmentation in all experiments. The results achieved on the bread-crust bombs demonstrated that even relatively high values of closed porosity (6 vol.%) only exhibited a minor influence. By way of simplification, the pressure inside the closed pores was assumed to be at ambient conditions at the beginning of the experiments. In room temperature experiments (Scheu, 2005), the pressure in the closed porosity remained at or near ambient conditions. In high-temperature experiments (this study), this pressure was probably higher than ambient due to gas expansion and partial equilibration to the lithostatic pressure. However, as the samples did not remain long enough (less than 2 hours) above Tg, the acting pressure in closed pores will most likely not have reached the experimentally applied pressure. Different physical properties as described above might help to explain the varying fragmentation behaviour revealed for samples from different volcanoes (Spieler et al., 2004).

The influence of temperature on the fragmentation behaviour is to date not very well constrained. Spieler et al. (2002) showed that experimental temperature clearly affects the grain-size distribution of the artificial pyroclasts as experiments at comparable conditions (porosity, applied pressure) revealed a decreasing percentage of ash particles with increasing temperature. Most probably, a combination of two or more of the following parameters influences the temperature-dependent fragmentation behaviour of the Unzen samples:

- Strength of the glue: It is postulated that the response of the two different types of glues to rapid decompression may be different. Crystalbond^{TM} 509 was used at ambient temperature, a ceramic-type two-component glue (Haldenwanger$^{®}$) at high temperature.
- Thermal expansion. In hot experiments, the autoclave, sample container as well as the sample did expand, but most likely to various degrees. At high temperature (i.e. above the melting point), thermal expansivity data on highly viscous melts are sparse and missing for natural melts. No calculations (e.g. model by Lange and Carmichael) for the degree of expansivity of autoclave/sample holder on the one hand and the sample itself on the other hand have been performed. Therefore, the impact on wall friction and fragmentation behaviour is not known for this study.
- Changing "dynamic tensile strength". Spieler et al. (2003) assumed that the dynamic tensile strength of melts is reduced with increasing temperature, and therefore may be responsible for the observed decreasing fragmentation threshold with increasing experimental temperature, achieved on samples of Mt. St. Helens.

The fragmentation threshold values achieved by Spieler (2001) and Kueppers (this study) on three sample sets with comparable open porosity did not demonstrate a clear influence of the sample size. Two pairs of samples (ENSP/01 B and MUZD UI/01 C) revealed constant values, the 14.50 vol.% open porosity sample (FD24693/00 E) showed a fragmentation threshold reduction with increasing sample size (Table 2). Although this data set does not allow for a statistically relevant interpretation, the experiments in SC-B sample containers nevertheless revealed that the wall friction may have had a major influence on the fragmentation behaviour. The ratio of the cylinder volume to the cylinder surface (wall) (11.35 cm³ to 26.70 cm²) was 2.35 for small cylinders, whereas 1.54 for the large cylinders (31.86 cm³ to 49.01 cm²).

Comparison of rapid decompression fragmentation experiments and static fragmentation tests (DIN EN 1015-11:1999/8):

A comparison of experiments performed in the fragmentation bomb and tests according to industrial standards showed concordant results in terms of a lower fracture rigidity with increasing porosity. However, the different sample geometry (cylinder vs. prism), the confining conditions (glue vs. no confinement) and the way how the stress is applied (internal gas pressure vs. point load or pull) are crucially different. The applied energy (J/cm³) is assumed to be distributed homogeneously throughout the cylinders. The achieved value fragmentation threshold (MPa) represents a value that has caused a complete disintegration of the sample. The strength values (N/mm²) on the other hand represent a value required to cause a single fracturing of the sample. Both values can be directly compared as 1 N/mm² is defined as 1 MPa. Intuitively, the energy required to cause full fragmentation should be by far higher than the load required causing a single fracture. The results (Table 3) show two main features: 1) Increasing porosity leads to a strength reduction of the samples investigated. 2) The Unzen samples revealed much lower values of strength at comparable porosity. This is probably due to a weakening of the samples by the large, prefractured phenocrysts.

Relevance for dome collapse

The density distribution at Unzen (see above) has been combined with fragmentation behaviour investigations to permit the construction of possible eruption scenarios. The most abundant rock types at Unzen have an open porosity of 8 and 20 vol%. This corresponds to a threshold of 18 and 5.4 MPa, respectively. As a volcano is not a perfectly sealed system and as many factors play an important role in developing gas overpressure (primary gas content, magma ascent rate, magma or country rock permeability), the overpressure inside a dome is hard to quantify. Estimations of Woods et al. (2002) give a range of 5-10 MPa for the centre of the dome in the case of Montserrat with a high pressure gradient. This value can only be regarded as an upper limit for the case of Unzen as the most porous lavas at Unzen (35.5 vol.%) had a lower porosity than the rock with the highest porosity at Montserrat (68.8 vol.%). A combination of estimated pressure conditions within an active volcano with experimental results on the fragmentation threshold and the density distribution determined in the field leads to the conclusion that most BAFs at Unzen were triggered by gravitational collapse. Puffs of ash often noted prior to BAFs close to the resulting collapse scar (Ui et al., 1999) possibly indicate locally restricted fragmentation events that 1) contributed to triggering gravitationally induced instability or 2) could take place after a collapse event had created a new surface (= remaining collapse scar). Explosive events at Unzen took only place within the first weeks of lava effusion after large-scale dome collapses.

6.1.6 Summary

The fragmentation bomb is a practical way for simulating and investigating the effects of gas-overpressure driven volcanic eruptions. Thirteen sets of differently porous samples (3 to 80.5 vol.% open porosity) from four different volcanoes (Montserrat, MSH, Stromboli, Unzen) were investigated for their fragmentation behaviour at 850 °C. Thorough analysis of the experimental results led to the conclusion that magma fragmentation of the above mentioned kind is the result of at least two different fracture processes and the degree of permeability. All three processes are taking place simultaneously upon rapid decompression. The influence of each process depends on the sample's porosity. At low porosities, shear forces will most probably be the most important fragmentation process. The drag force that tends to accelerate the melt in the direction of the highest decompression is acting against the wall friction force. The accelerating drag force is oriented vertically upwards for experiments of this study but natural eruptions showed that this direction can divert dramatically ("lateral blasts"; MSH, 1980; Bezymianny, 1956). With increasing porosity, the influence of gas expansion becomes increasingly important when the force exerted by the expanding gas on the bubble walls can cause tensile failure. This will most probably take place where the bubble walls are thinnest or weakened, e.g. by crystals. At high values of porosity, bubble textures (bubble number density, bubble radii, ellipsoidity, interconnectivity) are found to have a major influence on the fragmentation behaviour as they control 1) bubble wall thickness and 2) the sample permeability. Permeable gas flow can effectively reduce the applied overpressure (Mueller et al., 2005). As a consequence, two sample sets with identical values of open porosity but enormously differing bubble textures may exhibit completely different fragmentation behaviour. The investigated samples represent a large data set and, in the context of further samples, the results reveal the close relationship of open porosity and applied pressure for the fragmentation behaviour upon rapid decompression (Spieler et al., 2004). Although the general importance of the chemical composition for many physical and/or kinetic processes is beyond question, its influence during fragmentation was found to be minor.

6.2 Investigation of the fragmentation efficiency

6.2.1 Introduction

The results of the fragmentation threshold analysis shown above represent a paramount step towards a better understanding of syn-eruptive physical processes. Fine ash is no longer assumed to be exclusively produced in large quantities during phreatomagmatic eruptions. Nevertheless, detailed knowledge of ash generation and its associated energy conversion is still lacking for volcanic eruptions (Zimanowski et al., 2003). To investigate the efficiency of the fragmentation process and evaluate the influence of physical parameters thereon, a series of hot (850 °C) fragmentation experiments has been performed in the fragmentation bomb. Three sets of samples with varying porosity samples from Unzen volcano have been subjected to initial overpressure conditions above their respective fragmentation threshold (Figure 29). The efficiency was evaluated by grain-size and surface area analysis of the experimentally generated pyroclasts. As these pyroclasts did not undergo transport-related sorting, the

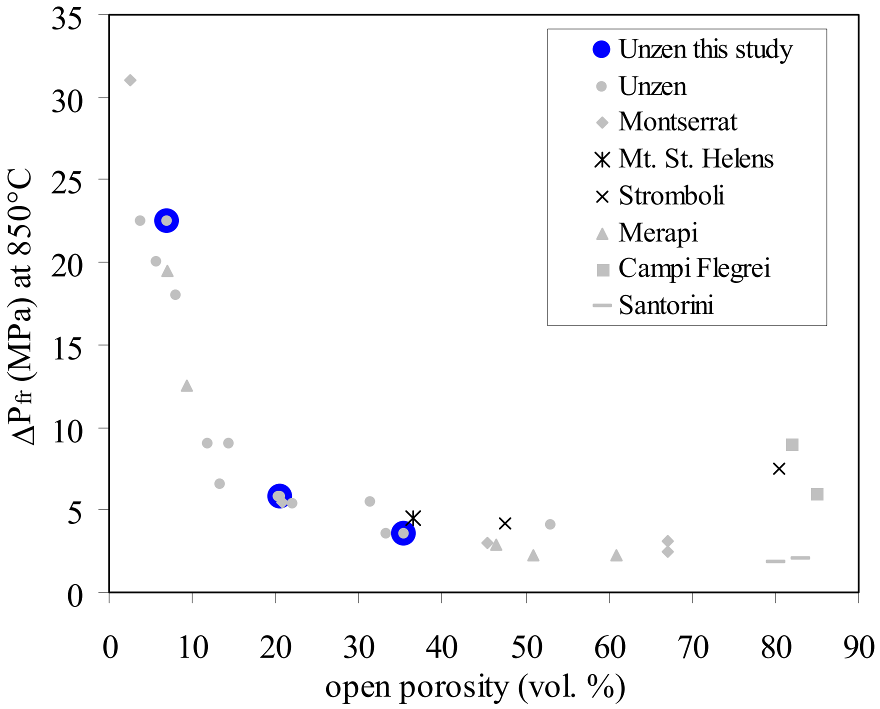

Figure 29: Plot of fragmentation threshold vs. open porosity. The lava samples of Unzen used to investigate the fragmentation efficiency are indicated by the massive blue circles. Their size of these three data points is only a matter of good visibility.

evaluated grain-size distribution plots are not directly comparable to those achieved from natural pyroclastic deposits.

6.2.2 Sample description

Cylindrical samples (d=25 mm, l=60 mm) have been drilled from the same blocks as samples for the fragmentation threshold analysis. The samples exhibit the following values (average) of open porosity:

- 7.0 vol.% open porosity (01 A), the densest rock type,
- 20.5 vol.% open porosity (01 C), the most abundant rock variety, and
- 35.5 vol.% open porosity (01 F), the most porous dome rock variety.

The closed porosity was found to be generally below 2.5 vol.%. The specific surface area (As_{spec}) of the sample cylinders ranges, depending on open porosity, from 0.020 to 0.045 m²/g (Scheu, 2005). The mean pre-fragmentation surface area (As_{cyl}) of the analysed sample sets is in the order of 1.7 to 2.0 m² (Table 4).

Sample name	Weight (g)	Open porosity (%)	Closed porosity (%)	Threshold (MPa)	Specific sample surface (m²/g)	Total cylinder surface (m²)
01 A	70.0	7.0 (+/- 1.5)	0.4	22.5	0.0247	1.744
01 C	59.0	20.5 (+/- 1)	0.9	5.8	0.0329	1.951
01 F	47.0	35.5 (+/- 1)	2.0	3.5	0.0419	1.984

Table 4: Properties of the samples used for the investigation of the fragmentation efficiency.

6.2.3 Experimental procedure

The experimental set-up used for these experiments was nearly identical to the one used in the fragmentation threshold analysis. All experiments have been performed at initial pressure conditions above the relevant ΔP_{fr}. The generated pyroclasts have been investigated for their post-fragmentation grain-size distribution and the inherent surface increase. The surface increase has been achieved by comparing the pyroclast surface results with surface values achieved on several cylinders per sample set (Scheu, 2005). Ceramic cements as the one used to glue samples in experiments evaluating the fragmentation threshold exhibit a high specific surface area. Therefore, experiments of this study had to be performed without the contamination of the pyroclasts. In order to guarantee a tight position of the sample, a slightly changed sample container was designed (type SC-C). At constant outer dimensions, the inner diameter of this sample container was reduced to 25 mm. The sample could be pressed therein after it had expanded slightly upon being heated with a high-temperature fan (approximately 550 °C). Upon cooling, the sample sat tightly in the sample container. Experiments have been performed at 850 °C and initial pressure conditions as high as 50 MPa. During the course of the experiments, it is known that autoclave, sample container, and sample will expand. However, it was assumed that the inner walls of the autoclave could prevent the sample container from expanding in a similar way (as during sample preparation) and that the sample therefore would have sat tightly before and during fragmentation. Few experiments below the fragmentation threshold confirmed this as they showed only partial fragmentation with unmoved bottom parts of the samples.

6.2.4 Pyroclast analysis

The pyroclast sampling started (earliest) two hours after the fragmentation of the sample. This time span was required for cooling of the high-T section and settling of the fine ash particles according to Stokes' Law. The high-P section was detached and replaced by a sedimentation cylinder. Upon opening the top of the low-P tank, it was rinsed with approximately ten litres of distilled water at 8.5 MPa. The water-pyroclast mixture was flowing into the sedimentation cylinder through a 250 µm sieve and thus became separated into a coarse and a fine fraction. Analysis of the coarse fraction involved weighing, dry sieving, and surface analysis. The suspended fine particles were allowed to settle in the sedimentation cylinder into a flask screwed to its bottom. After two days, the water was drained through a capillary tube to avoid turbulence-induced particle loss. The particles remaining on the walls of the sedimentation cylinder were flushed into the flask. This was connected to a rotational vaporizer and the fine fraction was dried in approximately 30 minutes. The degree of grain-size reduction during the rotational movement (20 rounds per minute) was assumed to be minor. Abrasion experiments (see below) were performed to address this question in detail. Analysis of the fine fraction ($x<250$ µm) included weighing, surface analysis, wet laser refraction, and dry post-laser refraction sieving.

Sieving

The dry coarse fraction ($x>250$ µm) was sieved at half-Φ steps ($\Phi=-\log_2 d$, with d=particle diameter in mm). Sieving duration was approximately 10 seconds per sieve class for particles ≥2 mm and approximately 20 seconds per sieve class for smaller particles. This resulted in a maximum total sieving duration of 180 seconds for the smallest particles of this fraction. Repetitive sieving confirmed the high accuracy of this sieving duration. The weight of all particles smaller than 250 μm after the sieving (sieving abrasion) is generally below 0.7 % of the sample weight.

After the laser refraction analysis, the fine particles were dried and particles larger than 90 μm were sieved at 2.5, 3, and 3.5 Φ. This allowed for comparison of the laser refraction and sieving data. As the laser refraction method to grain-size analysis of natural ash particles from Unzen volcano was found to be sufficiently precise, it was now possible to combine sieving (weight %) and laser refraction (volume %) data to a coherent grain-size distribution plot. For that, the laser refraction data were recalculated to weight %.

Surface analysis

To evaluate the fragmentation-induced increase in surface area, the pyroclast surface was analysed by Argon adsorption and compared to the cylinder surface. Compared to theoretical models (e.g. Koptsik et al., 2002), surface analysis of loose particles by Argon adsorption is very time-consuming. However, despite recent improvements, models still underestimate the surface areas actually measured by as much as two orders of magnitude (Riley et al. 2003). The noted discrepancy between measured and modelled values of surface area may primarily arise from simplified geometrical assumptions in these models (cubes, spheres). Experimentally derived pyroclasts from natural magmas are heterogeneous and irregular in shape and thus show different material properties. The surface represented by the outer cylinder surface (top, bottom and wall) is very small compared to the inner surface values. Therefore, no correction had to be performed although the force exerted by the expanding gas is primarily acting on the surface of the interconnected porosity.

Initially, the pyroclast surface analysis was supposed to reveal the surface increase represented by each size class individually. This approach had to be given up as the surface area represented by the particles of a single sieve class from a single sample was below the minimum detectable limit (0.1 m²). As a consequence, the particles of several sieve classes were put together to fulfil measuring requirements. Surface analysis was accordingly performed for four size groups:

- x<250 μm (I),
- 250<x<710 μm (II),
- 710<x<2000 μm (III), and
- x>2000 μm (IV).

Size group I comprised all fine particles separated during the rinsing process. Size groups II and III comprised three sieve classes each. The surface area (m²) of each size group was calculated from its specific surface area (m²/g) and its weight (g). Analysis of the particles larger than 2 mm (size group IV) showed that the specific surface area represented by these particles was in the range of the specific pre-fragmentation surface area of the corresponding cylinder. As a consequence, it was assumed by way of simplification that size group IV does not contribute effectively to the total surface increase of this sample and the specific surface area value of the respective cylinder was used. The total pyroclasts surface has been calculated by summing up the surface values represented by each size group:

$$As_{pyroclasts} = As_{spec\,(I)} * m_{(I)} + As_{spec\,(II)} * m_{(II)} + As_{spec\,(III)} * m_{(III)} + As_{spec\,(cyl)} * m_{(IV)} \qquad \text{Eq. 5}$$

The increase in surface area was evaluated by comparing pre- and post-fragmentation values.

$$\Delta As = \left[\frac{As_{pyroclast} - As_{cyl}}{As_{cyl}} * 100 \right] \qquad \text{Eq. 6}$$

As_{spec} is the specific surface area (m²/g) of a size group; $As_{pyroclasts}$ and As_{cyl} are the effective surface area values (m²).

Additionally, assuming that no particle “remembers” the pressure at which it had been generated, the surface of each sieve class was measured separately after putting together the particles of several samples. In that way the samples represented enough surface to become reproducibly measured.

Laser refraction analysis

Fine particle grain-size analysis was performed by laser refraction using a Beckman-Coulter© LS230 (Figure 30, measuring range 0.0375-2000 µm, wave length 750 nm, software version 3.01). This technique calculates the grain-size distribution of a suspended sample based on refraction angle and intensity of a laser beam. It has several assumptions:

- Particles are spherical, non-porous, opaque, and large in respect to the used wavelength.
- Particles are distant enough from each other, i.e. now shadowing effect.
- All particles refract the light with the same efficiency.

There are two optical models to interpret the light scattering pattern and convert it to a size distribution, the Fraunhofer diffraction model and the Mie Theory. The Fraunhofer model is based on the action of light diffracted at the particles whereas the Mie Theory accounts for the effects of diffraction and diffusion as light travels through particles. The latter theory is more accurate for small grain sizes (submicron) but requires knowledge of the refraction index and the absorption.

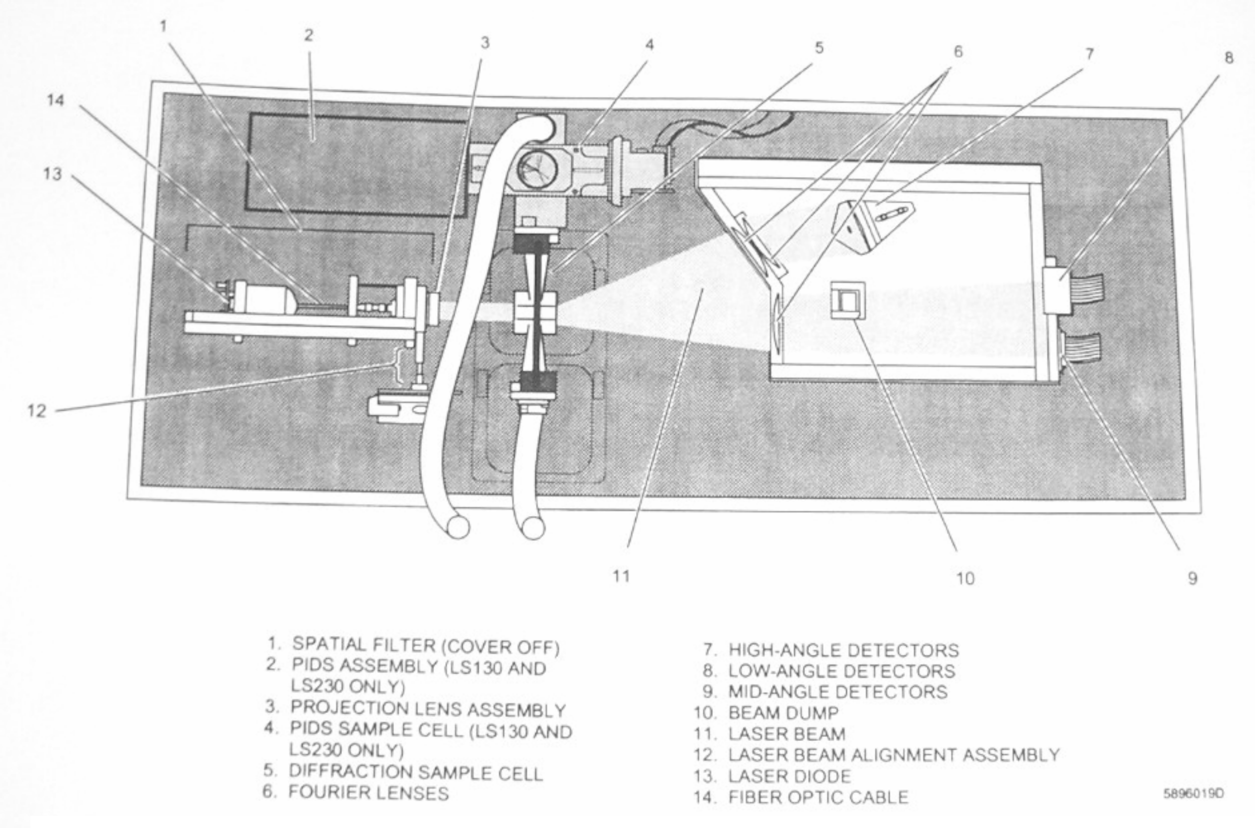

Figure 30: Schematic drawing illustrating the detection of the refraction pattern in the Coulter LS230 device. Picture taken from the Coulter handbook.

In this study, the data have been evaluated with the Fraunhofer Theory for several reasons: 1) The amount of fine particles is low. (Particles smaller than 10 µm (respirable ash) only represent a very small proportion: up to 0.15 g [0.28 wt.%] for 01 A, 0.25 g [0.58 wt.%] for 01 C and 0.33 g [0.70 wt.%] for 01 F samples). 2) Unknown refraction indices (The experimentally generated pyroclasts represent multi-material mixtures and do not exhibit a constant refraction index.). 3) Unknown degree of absorption and/or multi-absorption.

The suspended sample is circulating in a tube at constant flow speed. In the measuring cell consisting of two parallel glass plates, the laser beam passes the sample perpendicularly to the flow direction and is refracted at the surface of the individual particles. The degree of refraction is proportional to the particle size and the angle of refraction increasing with decreasing particle size. The refracted light forms concentric rings, the radius of which is dependent upon the particle size. The intensity of light refracted to a certain angle is dependent upon the proportion of the particle size in question. Fourier lenses collect the diffracted light and focus it onto three sets of detectors, a low-angle (LAD), a mid-angle (MAD), and a high-angle detector (HAD). The LAD consists of 62 detector elements that allow for a very high resolution. Both the MAD and HAD consist of 32 detector elements each. Each detector element registers light of a certain refraction angle.

In this study, 250 µm was chosen as grain-size boundary between sieving and laser refraction analysis. Therefore, the influence of shadowing of big particles on the results of the laser refraction is reduced. As the amount of sample was impractible to be measured in a single run of laser refraction, it was split into sub-fractions of approximately 0.1 g each. Each sub-fraction was measured independently. The results of all sub-fractions from each sample were assessed based on their weight and the result for the complete sample (vol.%) was calculated.

The total grain-size distribution plots (wt.%) result from a combination of sieving data of particles > 250 µm and laser refraction data (initially in vol.%) of all smaller particles.

SEM analysis

Scanning Electron Microscopy analysis was performed on pyroclasts of variable grain size. Although all particles are derived from experiments at 850 °C (i.e. above Tg), no particle was found that exhibited signs of post-fragmentation surface changes by surface tension.

6.2.5 Results

The data analysis was twofold: 1) The grain-size distribution of the experimentally generated pyroclasts was evaluated as a function of porosity and applied pressure, and 2) the increase in surface area as a function of particle size and applied energy.

The results revealed that the values achieved by laser refraction technique and post-laser refraction sieving (dry) differed by less than 0.5 wt.% based on the total sample weight. This proofed the applicability of the laser refraction method to the grain-size analysis of experimentally generated Unzen pyroclasts although they exhibited irregular shapes and varying refraction indices. The laser refraction data (vol.%) have been converted to wt.% and assessed to half-Φ steps. In that way, these data could be combined with sieving data and formed one grain-size plot covering the complete range of particle size. These plots clearly showed a non-Gaussian particle size distribution with decreasing grain-size of the most abundant fraction with increasing experimental pressure (Figure 31). Plotting the weight fraction of fine particles (< 250 µm) as a function of applied experimental pressure, a large scatter within all three data sets was observed. This was most probably due to heterogeneities in the natural samples. Nevertheless, the positive correlation is beyond doubt (Figure 32). For any applied pressure, the amount of ash particles produced increased with the samples' porosity. Taking the fine particle genesis as a matter of the fragmentation efficiency, a close link to the potential energy for fragmentation (PEF) became obvious. PEF was calculated

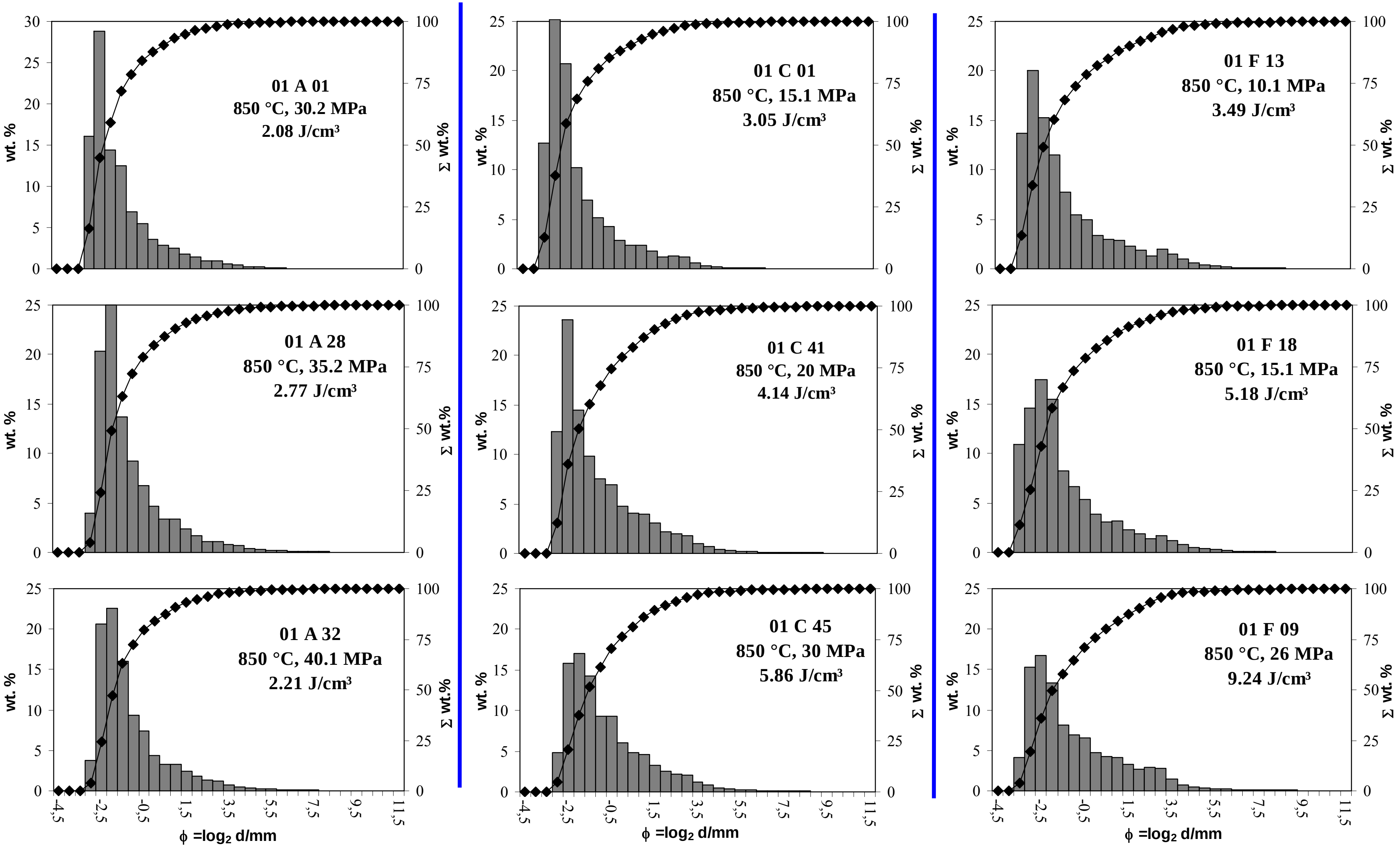

Figure 31: Three grain-size plots of each investigated sample set. Left column: MUZ 2001 A. Middle column: MUZ 2001 C. Right column: MUZ 2001 F. x-axis is giving the grain-size in half-Φ steps with decreasing grain-size to the right.

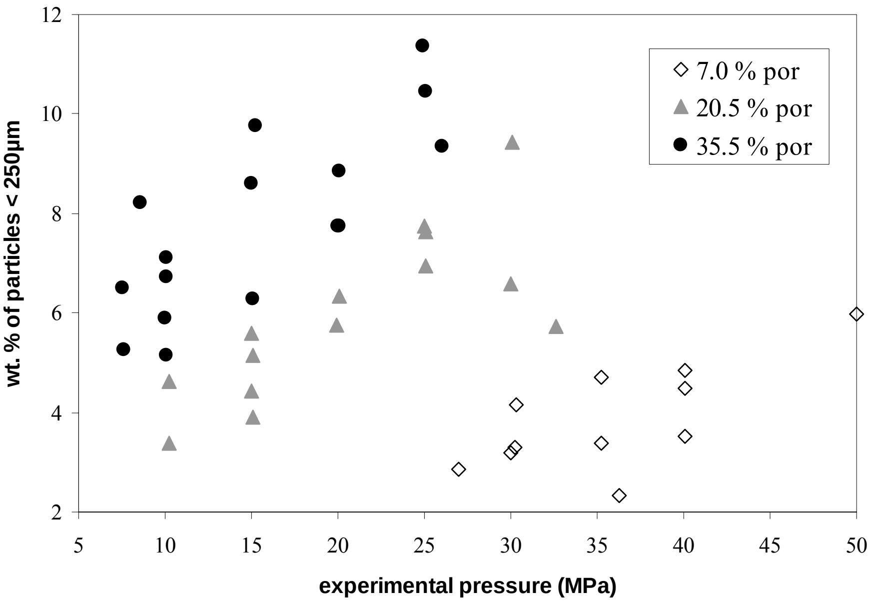

Figure 32: Plot revealing the increase of experimentally generated pyroclasts (< 250 µm) as a function of porosity and applied pressure. The large scatter is most probably due to the natural (i.e. not synthetic) sample nature.

from the sample's volume (V_{cyl} in m^3), the gas fraction (θ, dimensionless), and the applied experimental pressure (ΔP in Pa). The PEF stored in the sample, i.e. the amount of pressurised gas, could be estimated and may be approximated as:

$PEF := \theta * V_{cyl} * \Delta P$ Eq. 7

All three sample sets indicated a common trend when considering the particles smaller than 250 µm. However, when considering all ash-sized particles, the amount of generated particles was highest for the 20.5 % porosity samples (Figure 33). It was investigated whether the grain-size distributions followed a Gauss- or a Rosin-distribution (Schleyer, 1987). All data points fall in the field of the Rosin-distribution. Accordingly, the appropriate parameter to express the overall grain-size reduction is defined as:

$\text{Mean diameter} = (\Phi_{18.4} + \Phi_{36.79} + \Phi_{68.4})/3$ Eq. 8

In a plot of this mean diameter vs. PEF, the effect of porosity and applied pressure on the grain-size reduction was clearly visible (Figure 34).

The increase in surface area was evaluated by comparing pre- and post-fragmentation values. The specific surface area (As_{spec}) of the sample cylinders was found to be in the range of 0.020 to 0.045 m^2/g, depending on open porosity (Scheu, 2005). The mean pre-fragmentation surface area (As_{cyl}) of the analysed sample sets was accordingly in the order of 1.7 to 2.0 m^2 (Table 4). It is noteworthy that even larges differences in open porosity did not influence the represented free surfaces dramatically. Particles > 2 mm exhibited values of specific surface area similar to the pre-fragmentation cylinders. The experimental pyroclasts

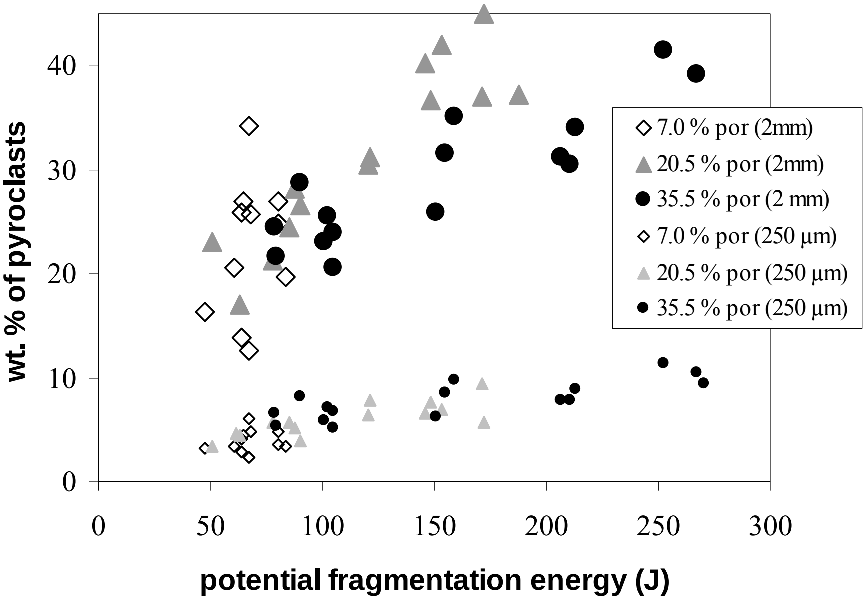

Figure 33: A plot of the weight fraction of experimentally generated fine particles vs. the potential fragmentation energy (J). It becomes obvious that all three data sets define a common trend for particles < 250 µm. When considering all ash-sized particles, the 20.5 % porosity samples exhibits the highest amount of generated particles for a comparable energy value.

have accordingly been measured exclusively for particles < 2 mm and allowed for quantifying the increase in specific surface area (m^2/g) with decreasing particle size. As anticipated, the results proved that the highest specific surface was represented by the particles x<250 µm. Average values of As_{spec} can be seen in Tables 5 through 7 for the three size groups of the

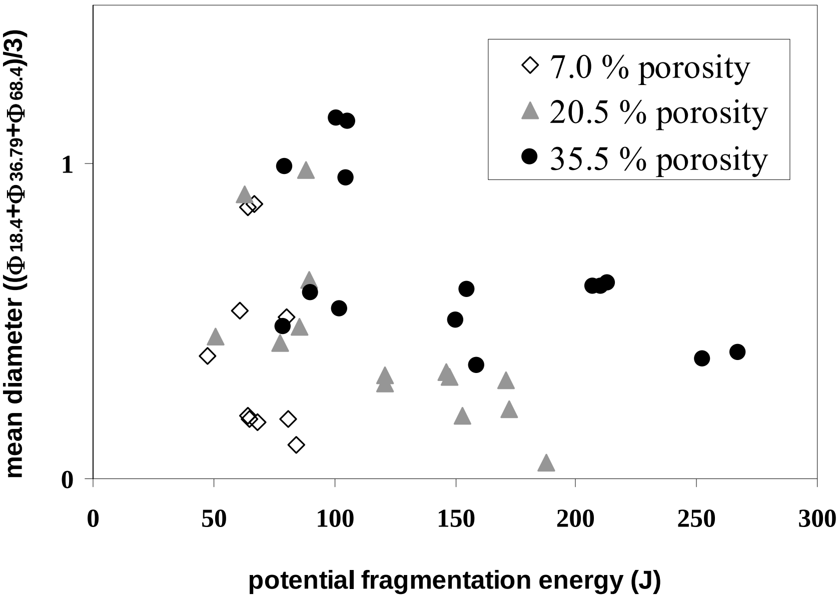

Figure 34. Plot of mean diameter vs. potential energy. Small mean diameter values represent small particles. The data from 01 A samples show a large scatter. Mean diameter values for 01 C samples are generally slightly lower compared to 01 F samples.

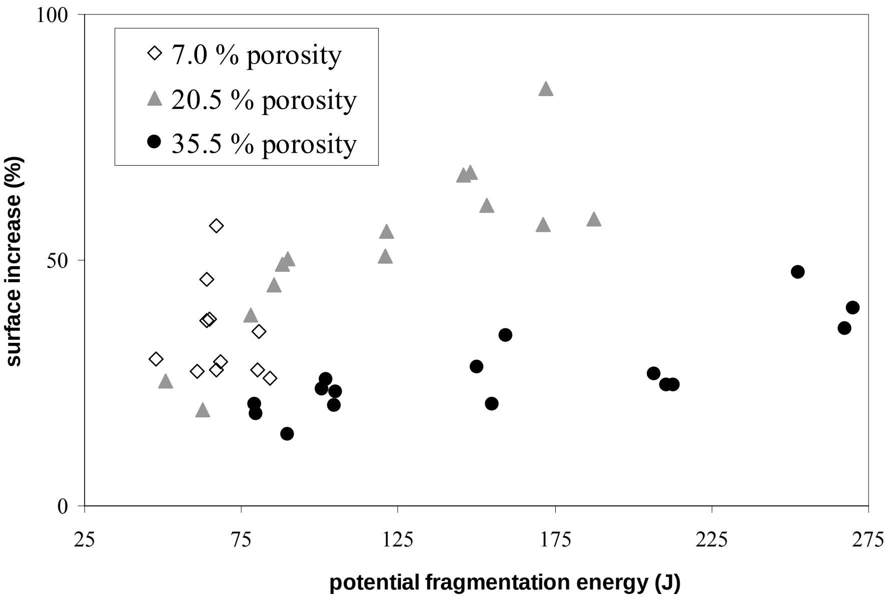

Figure 35: Plot of surface increase (%) vs. potential fragmentation energy (J). The dense samples exhibit a large scatter. The more porous samples (35.5 vol.% porosity) revealed a lower surface increase than the less porous sample (20.5 vol.% porosity).

three sample sets. The surface increase was found to be positively correlated with the PEF. Results from experiments with dense samples showed a large scatter but the trend was clearly visible for samples with a higher porosity (Figure 35). The newly generated surface was approximately twice as high for 01 C samples (20.5 vol.% open porosity) compared to 01 F samples (35.5 vol. % open porosity).

Additionally, assuming that no particle "remembers" the pressure at which it had been generated, the surface of each sieve class (250 µm < x < 2.8 mm) was evaluated separately after putting together the particles of several samples. In that way, the samples represented enough surface area to become reproducibly measured and it was possible to evaluate the specific surface as a function of particle size. The specific surface area did not decrease linearly with increasing particle size (Figure 36). The surface represented by all ash particles could be calculated by summing up the products of all sieve classes with its corresponding specific surface value. The increase in surface has then been calculated as described above. Therefore, the observed results of surface increase are generally lower than those achieved from measuring the three size groups.

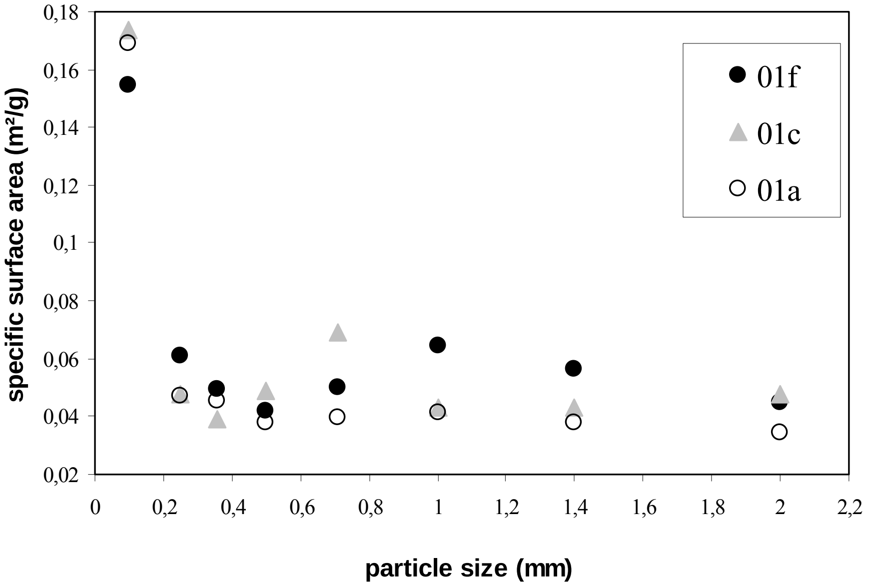

Figure 36: After putting together pyroclasts of a single sieve class of several samples, enough surface are was represented for reproducible measurements. A non-linear dependency achieved specific surface area with increasing particle size became obvious.

							Size group I				Size group II				Size group III			
Sample	Applied pressure (MPa)	Cylinder weight (g)	Open porosity (%)	Energy (J)	Specific cylinder surface (m²/g)	Pre-fragmentation cylinder surface (m²)	Weight of particles <250 µm (g)	Percentile of starting weight	Specific surface area (m²/g)	New surface (m²)	Weight of particles 250 <x< 710 µm (g)	Percentile of starting weight	Specific surface area (m²/g)	New surface (m²)	Weight of particles 710 < x 1400 µm (g)	Percentile of starting weight	Specific surface area (m²/g)	New surface (m²)
01 A26	27.0	69.7760	8.11	63.87	0.0255	1.7769	1.9923	2.8553	0.2396	0.4266	2.7245	3.9046	0.1074	0.2232	4.8900	7.0081	0.0300	0.0222
01 A33	30.0	72.8515	5.39	47.62	0.0238	1.7363	2.3144	3.1769	0.1556	0.3050	3.5342	4.8512	0.0657	0.1480	6.0833	8.3503	0.0349	0.0673
01 A21	30.2	70.5884	6.90	60.85	0.0247	1.7464	2.3361	3.3095	0.1581	0.3115	3.9913	5.6543	0.0441	0.0773	8.1786	11.5863	0.0365	0.0962
01 A19	30.3	70.3170	7.26	64.15	0.0250	1.7584	2.9248	4.1595	0.1969	0.5029	5.0710	7.2116	0.0535	0.1447	10.1877	14.4882	0.0413	0.1665
01 A27	35.2	69.6333	8.18	83.95	0.0255	1.7726	2.3542	3.3809	0.1777	0.3583	3.8850	5.5792	0.0434	0.0695	7.4838	10.7474	0.0305	0.0374
01 A28	35.2	69.8255	7.86	80.68	0.0253	1.7677	3.2828	4.7014	0.1335	0.3551	5.2200	7.4758	0.0489	0.1231	10.3571	14.8328	0.0398	0.1500
01 A24	36.3	71.3758	6.32	67.14	0.0244	1.7410	1.6625	2.3292	0.1976	0.2880	2.6100	3.6567	0.0631	0.1010	4.6568	6.5243	0.0447	0.0946
01 A32	40.1	71.5525	5.51	64.92	0.0239	1.7105	3.2049	4.4791	0.1429	0.3812	5.3778	7.5159	0.0524	0.1532	10.6375	14.8667	0.0351	0.1191
01 A29	40.1	72.2315	5.80	68.40	0.0241	1.7393	3.5021	4.8484	0.1467	0.4294	5.1595	7.1430	0.0363	0.0630	9.9297	13.7470	0.0259	0.0181
01 A30	40.1	70.7337	6.78	79.95	0.0247	1.7449	2.4989	3.5328	0.1420	0.2931	4.1986	5.9400	0.0477	0.0967	9.2281	13.0500	0.0318	0.0658
01 A31	50.0	72.4672	4.60	67.07	0.0234	1.6928	4.3649	6.0201	0.1600	0.5964	6.8740	9.4857	0.0315	0.0556	13.5670	18.7216	0.0466	0.3153
Average values			6.61		0.0246	1.7443			0.1611				0.0487				0.0361	

Table 5: Surface analysis results for dense Unzen samples (01 A)

							Size group I				Size group II				Size group III			
Sample	Applied pressure (MPa)	Cylinder weight (g)	Open porosity (%)	Energy (J)	Specific cylinder surface (m^2/g)	Pre-fragmentation cylinder surface (m^2)	Weight of particles <250 µm (g)	Percentile of starting weight	Specific surface area (m^2/g)	New surface (m^2)	Weight of particles 250 <x< 710 µm (g)	Percentile of starting weight	Specific surface area (m^2/g)	New surface (m^2)	Weight of particles 710 < x 1400 µm (g)	Percentile of starting weight	Specific surface area (m^2/g)	New surface (m^2)
01 C09	10.2	51.0530	20.08	51.00	0.0327	1.6668	2.3673	4.6370	0.1590	0.2991	3.5504	6.9543	0.0542	0.0765	5.7962	11.3533	0.0410	0.0484
01 C22	10.2	58.5668	21.29	53.99	0.0334	1.9546	1.9780	3.3773	0.1619	0.2542	2.8658	4.8932	0.0655	0.0921	5.0787	8.6716	0.0421	0.0443
01 C32	15.0	50.3824	20.90	78.22	0.0331	1.6697	2.2285	4.4232	0.1527	0.2664	3.0543	6.0622	0.0942	0.1865	5.4212	10.7601	0.0698	0.1987
01 C44	15.0	58.4138	20.50	76.72	0.0329	1.9218	3.2690	5.5963	0.1986	0.5417	4.3724	7.4852	0.0803	0.2073	7.8524	13.4427	0.0616	0.2254
01 C01	15.1	59.3028	20.19	76.07	0.0327	1.9400	2.3195	3.9113	0.1664	0.3101	5.5919	9.4294	0.0908	0.3248	8.8055	14.8484	0.0693	0.3222
01 C46	15.1	60.5848	19.35	72.75	0.0322	1.9514	3.1253	5.1586	0.1865	0.4822	4.2089	6.9471	0.0777	0.1915	7.4680	12.3265	0.0605	0.2113
01 C41	19.9	59.3698	20.79	102.69	0.0331	1.9636	3.4148	5.7518	0.1804	0.5031	5.4465	9.1739	0.0674	0.1870	9.2716	15.6167	0.0671	0.3155
01 C38	20.1	59.1292	20.71	103.32	0.0330	1.9528	3.7526	6.3464	0.1756	0.5350	5.7017	9.6428	0.0779	0.2559	8.9956	15.2135	0.0677	0.3119
01 C42	25.0	59.0422	21.06	131.10	0.0332	1.9623	4.5814	7.7595	0.1567	0.5656	7.0669	11.9692	0.0595	0.1856	13.1013	22.1897	0.0683	0.4594
01 C43	25.1	59.7170	20.25	126.46	0.0328	1.9557	4.1520	6.9528	0.1873	0.6417	6.2330	10.4376	0.0667	0.2116	11.4650	19.1989	0.0749	0.4832
01 C39	25.1	59.8408	19.99	125.14	0.0326	1.9505	4.5673	7.6324	0.1792	0.6696	7.0045	11.7052	0.0671	0.2417	12.4657	20.8314	0.0653	0.4077
01 C45	30.0	60.5014	19.54	146.20	0.0323	1.9556	3.9815	6.5808	0.1692	0.5450	6.2350	10.3055	0.0687	0.2268	12.1566	20.0931	0.0617	0.3576
01 C40	30.1	60.2772	19.59	146.88	0.0324	1.9502	5.6844	9.4304	0.1700	0.7824	7.6436	12.6807	0.0572	0.1899	13.8477	22.9734	0.0823	0.6916
01 C34	32.6	60.4233	19.68	159.81	0.0324	1.9582	3.4596	5.7211	0.1906	0.5469	6.4815	10.7268	0.0682	0.2320	12.5262	20.7307	0.0620	0.3703
Average values			20.28		0.0328	1.9514			0.1739				0.0711				0.0638	

Table 6: Surface analysis results for Unzen samples (01 C)

							Size group I				Size group II				Size group III			
Sample	Applied pressure (MPa)	Cylinder weight (g)	Open porosity (%)	Energy (J)	Specific cylinder surface (m²/g)	Pre-fragmentation cylinder surface (m²)	Weight of particles <250 µm (g)	Percentile of starting weight	Specific surface area (m²/g)	New surface (m²)	Weight of particles 250 <x< 710 µm (g)	Percentile of starting weight	Specific surface area (m²/g)	New surface (m²)	Weight of particles 710 < x 1400 µm (g)	Percentile of starting weight	Specific surface area (m²/g)	New surface (m²)
01 F10	7.5	47.0880	36.06	79.08	0.0422	1.9888	3.0603	6.50	0.1449	0.3142	3.2149	6.83	0.0611	0.0606	5.2665	11.18	0.0503	0.0426
01 F08	7.6	47.2526	35.85	79.73	0.0421	1.9898	2.4828	5.25	0.1296	0.2171	2.8947	6.13	0.0717	0.0857	4.8289	10.22	0.0590	0.0816
01 F21	8.6	47.4114	35.64	89.97	0.0420	1.9905	3.9005	8.23	0.0885	0.1812	3.7631	7.94	0.0627	0.0781	5.9566	12.56	0.0487	0.0400
01 F12	10.1	47.2564	35.62	105.31	0.0420	1.9834	3.1734	6.72	0.1448	0.3262	3.2246	6.82	0.0654	0.0754	4.9068	10.38	0.0555	0.0661
01 F13	10.1	47.6276	34.55	102.15	0.0413	1.9684	3.3827	7.10	0.1659	0.4214	3.4005	7.14	0.0596	0.0621	5.3688	11.27	0.0472	0.0312
01 F16	10.1	47.4890	35.43	104.86	0.0419	1.9878	2.4503	5.16	0.1678	0.3085	2.7583	5.81	0.0576	0.0433	4.5338	9.55	0.0548	0.0587
01 F17	10.0	48.5094	34.23	100.58	0.0411	1.9956	2.8576	5.89	0.1689	0.3651	3.1031	6.40	0.0549	0.0425	5.2026	10.72	0.0552	0.0729
01 F18	15.1	47.8340	34.33	150.43	0.0412	1.9707	3.0041	6.28	0.1874	0.4391	3.4974	7.31	0.0607	0.0682	5.8624	12.26	0.0505	0.0545
01 F19	15.2	46.6414	36.05	159.31	0.0422	1.9697	4.5497	9.75	0.1655	0.5610	4.5519	9.76	0.0547	0.0568	7.2352	15.51	0.0520	0.0703
01 F20	15.0	47.1762	35.54	155.20	0.0419	1.9778	4.0531	8.59	0.1288	0.3520	3.9998	8.48	0.0546	0.0508	6.7881	14.39	0.0439	0.0131
01 F01	20.0	47.2460	35.93	210.73	0.0422	1.9918	3.6589	7.74	0.1619	0.4379	4.2448	8.98	0.0584	0.0687	6.4738	13.70	0.0405	-0.0107
01 F02	20.1	47.0156	36.19	213.03	0.0423	1.9894	4.1664	8.86	0.1421	0.4157	4.6040	9.79	0.0504	0.0372	7.2128	15.34	0.0481	0.0414
01 F05	20.1	47.5074	35.22	206.80	0.0417	1.9826	3.6797	7.75	0.1665	0.4591	4.2842	9.02	0.0558	0.0601	6.8398	14.40	0.0446	0.0194
01 F06	25.1	46.7618	36.36	267.35	0.0424	1.9834	4.8863	10.45	0.1611	0.5801	5.2675	11.26	0.0464	0.0208	8.1739	17.48	0.0568	0.1174
01 F07	24.9	47.9322	34.76	252.67	0.0415	1.9871	5.4433	11.36	0.1736	0.7190	5.5919	11.67	0.0531	0.0648	8.8055	18.37	0.0607	0.1695
01 F09	26.0	47.2388	35.55	270.31	0.0419	1.9807	4.4224	9.36	0.1713	0.5721	4.7439	10.04	0.0514	0.0448	7.2688	15.39	0.0678	0.1880
Average values			35.46		0.0419	1.9836			0.1543				0.0574				0.0522	

Table 7: Surface analysis results of porous Unzen samples (01 F)

6.2.6 Interpretation

The used experimental set-up allowed for an almost complete sampling of pyroclasts (less than 0.1 g loss) generated during gas-overpressure-driven fragmentation under well constrained conditions. As the experimental pyroclasts underwent minimal transportation-related sorting, the resultant grain-size distributions may partially differ from grain-size distributions of natural deposits.

Brittle magma fragmentation occurs when the stress exerted by gas on the bubble walls can not be dissipated by viscous deformation and exceeds the tensile strength. Bubble wall thickness is generally decreasing with increasing porosity and one might assume that thinner bubble walls withstand less pressure differential. However, fibre elongation tests (Dingwell and Webb, 1989) showed that below a certain critical thickness, high surface tension values may lead to an increase in strength. SEM investigations of the pyroclasts produced during fragmentation experiments did not reveal any sign for post-fragmentation changes in surface shape. Preliminary fractographic investigations by Prof. Daniel Rittel and his students come to the same conclusion (pers. comm.). Accordingly, ductile fragmentation is unlikely to have been involved during the experiments of this study.

The influence of increasing experimental pressure in combination with porosity had a major influence on the pyroclast genesis. All three sets of samples exhibited a shift of the most abundant grain-size fraction towards a smaller size (Figure 31) and a corresponding increase of the weight fraction of particles < 250 µm with increasing pressure. For a given pressure, the amount of ash particles produced was highest for 01 F samples (Figure 32). The large scatter within each data set may have been a result of locally restricted heterogeneities of the natural samples. The influence of minor changes in porosity was found to be highest for the low-porosity samples. As the experimental results could not be directly compared based on the values of applied experimental pressure, the grain-size data were compared on the basis of PEF (Figure 33). A comparison of weight fractions of pyroclasts < 250 µm and < 2 mm revealed different trends. While the < 250 µm particles indicated a common trend for all three sample sets, all ash-sized particles indicated that, at a constant value of PEF, the fragmentation of the 20.5 vol.% porous samples (01 C) was more efficient than of the 35.5 vol.% porous samples (01 F). Thin section analysis (see above) had shown that the 01 F samples are characterized by large bubble diameters and high interconnectivity. Accordingly, the applied energy (PEF) could be effectively reduced during the fragmentation process by permeable gas flow as indicated by Mueller et al. (2005). Accordingly, only a part of the PEF did actually go into the fragmentation process and higher values of energy had to be applied to achieve amounts of generated pyroclasts comparable to 01 C samples. The data of the dense samples (01 A) exhibited a large scatter and only cover a small PEF range at the lower end of the range covered within this study. Applying higher values of overpressure in dense samples was found to be an ineffective means of increasing energy as it remains small and locally restricted. The apparent steep, near vertical increase in surface is therefore probably not representative of gas expansion induced fragmentation.

As revealed from the analysis of the fragmentation behaviour, shear failure due to the contrasting forces of unloading-induced sample acceleration and wall friction was probably the most important fragmentation process in dense samples. As the decompression rate is a matter of applied pressure, the pulling force of the unloading wave was unproportionally high for 01 A samples even at comparably small values of energy.

In addition to the grain-size analysis, the fragmentation efficiency was evaluated as a function of surface increase (%). It accounts for the amount of new fracture surfaces generated by brittle fragmentation upon rapid decompression. Figure 35 shows a plot of surface increase (%) vs. potential energy for fragmentation. Here, the trend indicated by Figure 33 becomes even more striking. The amount of new surface represented by 01 C samples was approximately twice as high as for 01 F samples. This is probably related to two factors: 1) A decrease of bubble wall thickness with increasing porosity although a single bubble wall might break several times. However, it is worth noting that any fracture surface in 01 F samples is likely to be generally smaller than in 01 C samples and will therefore not have contributed as much to the total surface increase. Accordingly, any bubble wall break-up in 01 C samples will represent more newly formed surface than it would in 01 F samples. 2) Effective reduction of the applied overpressure by permeable gas flow due to textural features.

6.2.7 Summary

Three sets of Unzen samples have been investigated to evaluate the influence of open porosity in combination with applied pressure on the fragmentation behaviour and pyroclast generation (fragmentation efficiency). All experiments have been performed at 850 °C and at initial pressure values above the respective fragmentation threshold. The aforementioned set-up allowed for accurate simulation of explosive volcanic fragmentation whilst investigating the resulting pyroclast generation. The grain-size distribution was analysed by dry sieving for particles > 250 µm and laser refraction of the suspended particles smaller than 250 µm. Laser refraction was found to be applicable to the size analysis of pyroclasts from natural samples. The increase in surface area has been evaluated by Argon adsorption of pre-fragmentation cylinders and post-fragmentation pyroclasts. The results show that fragmentation efficiency depends on the potential energy for fragmentation (PEF) stored in the samples that can be estimated from the porosity and the applied pressure. Grain-size and surface analysis data for the dense samples (MUZ A) generally exhibit a large scatter but the mean (MUZ C) and highly porous samples (MUZ F) show concordant trends. At a constant pressure, the weight fraction from experimentally derived ash particles is highest for the most porous samples. Data from each sample set indicate increasing amounts of ash particles with increasing pressure. At a comparable value of PEF, the average grain-size is smaller for MUZ C samples indicating a more efficient fragmentation. The increase in surface is approximately twice as high for MUZ C samples compared to MUZ F samples. Two reasons may be responsible for this: 1) decreasing bubble wall thickness with increasing porosity leading to a less efficient generation of new surface and 2) effective reduction of the applied overpressure by permeable gas flow.

7 Abrasion experiments

7.1 Introduction

During mass movements of any kind, particles interact with other particles. If for example rocks were to be the dominant constituent of such a movement, this would lead to surface rounding (abrasion) or grain-size reduction (disruption) with following abrasion at the newly formed edges. Transport-related processes of such kind may have changed the original density distribution as evaluated by Kueppers et al. (2005) by preferential abrasion of the least rigid clasts. The fine particles (< 250 µm) of the fragmentation efficiency study (see above) have been dried in a rotational vaporizer. For most of this drying process, particles have been suspended in water but abrasion is likely to have been taken place during the final stage of this drying process.

Due to their heterogeneous composition in grain size and temperature (as well the involved velocities and energy), natural volcanic rock mass movements (e.g. rock falls, BAFs, pyroclastic flows) can hardly be simulated in the laboratory. Rotational movement in a closed container was used as a proxy to shed light on the susceptibility of porous clasts to abrasion.

7.2 Sample description

In this study, four sets of variously porous clasts of Unzen have been investigated that exhibit the following average values of open porosity:

- 5.7 vol.% porosity [01 B]
- 20.5 vol.% porosity [01 C]
- 35.0 vol.% porosity [00 F]
- 53.5 vol.% porosity [BKB]

The first three sets (01 B, 01 C, and 00 F) represent dome-forming lavas, the highly porous sample (BKB) derives from bread-crust bombs from the 11 June 1991 vulcanian eruption. Approximately 2 kg of each starting material have been broken-up in a jaw crusher. The resulting clasts have been sieved wet at 8 (-3.0 Φ) and 11.2 mm (-3.5 Φ), respectively. Fragments of the chilled margin of the bread-crust bombs have not used.

7.3 Experimental procedure

40 to 160 g of the dry sample material were subject to rotational movement at ambient temperature in a gum rotational tumbler (100 inner, 116 mm outer diameter) at constant speed

(40 rounds per minute). Theoretically, the particles have been rolling 12.57 m/min. Experimental duration was 15, 30, 45, 60, and 120 minutes, respectively, with no water being present. The used experimental durations have been much longer than natural run-out times of BAFs in order to allow for their highly energetic nature. Every experiment started with new sample material. Particle analysis included washing out, drying and sieving. The increase in generated fine particles (< 250 µm) was evaluated as a function of experimental duration and the open porosity of the samples.

7.4 Results

The results reveal the paramount influence of the porosity on the degree of abrasion (Figure 37, Table 8). It is usually highest during the first 30 to 45 minutes. The degree of abrasion was generally found to be slightly higher with bigger starting material size. All dome-forming lava samples (01 B, 01 C, and 00 F) show sub-parallel results with higher values of generated particles with increasing porosity. Interestingly, in 15 minutes experiments, more fine particles are generated from 00 F samples than from BKB samples. Experiments with longer durations did produce additional fine particles but at diminishing rates. Dense samples are hardly abraded and the increase in generated fine particles remained minor (< 1 wt.%) even in the longest lasting experiments. The amount of generated fine particles increases with the samples' porosity and is as high as 6 wt.% for the most porous samples experiments that lasted for 120 minutes. The large phenocrysts were found to have represented zones of higher resistivity to abrasion.

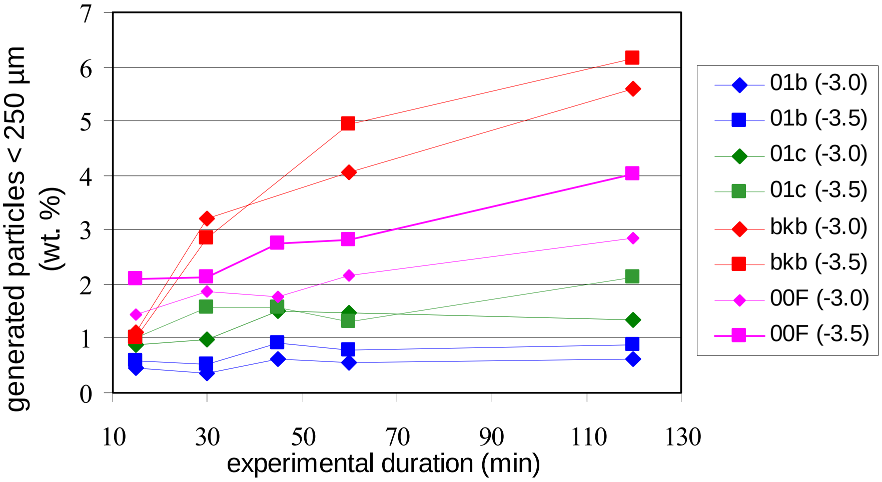

Figure 37: Plot of generated particles (< 250 µm) showing a general positive correlation with experimental duration and porosity. The higher amount of generated particles in 15 minutes experiments from 00 F samples compared to BKB samples showed the influence of bubble size on the abrasion.

Sample	Particle size (mm)	starting weight (g)	duration (min)	distance (m)	particles < 250 µm (g)	weight fraction of particles < 250 µm
01 B	8<x<11.2	121.8405	15	232.2	0.5449	0.45
01 B	8<x<11.2	127.1920	30	464.4	0.4768	0.37
01 B	8<x<11.2	129.1210	45	696.6	0.7953	0.62
01 B	8<x<11.2	111.9626	60	928.8	0.6201	0.55
01 B	8<x<11.2	115.3894	120	1857.6	0.7141	0.62
01 B	11.2<x<16	54.9733	15	232.2	0.3198	0.58
01 B	11.2<x<16	126.8470	30	464.4	0.6726	0.53
01 B	11.2<x<16	156.8150	45	696.6	1.4378	0.92
01 B	11.2<x<16	119.5678	60	928.8	0.9465	0.79
01 B	11.2<x<16	117.2458	120	1857.6	1.0295	0.88
01 C	8<x<11.2	80.8404	15	232.2	0.7172	0.89
01 C	8<x<11.2	95.7902	30	464.4	0.9356	0.98
01 C	8<x<11.2	105.0134	45	696.6	1.5914	1.52
01 C	8<x<11.2	83.1144	60	928.8	1.2360	1.49
01 C	8<x<11.2	88.4996	120	1857.6	1.1829	1.34
01 C	11.2<x<16	75.6532	15	232.2	0.7709	1.02
01 C	11.2<x<16	109.7300	30	464.4	1.7071	1.56
01 C	11.2<x<16	130.8215	45	696.6	2.0642	0.00
01 C	11.2<x<16	86.3804	60	928.8	1.1322	1.31
01 C	11.2<x<16	94.7846	120	1857.6	2.0160	2.13
00 F	8<x<11.2	83.2822	15	232.2	1.2049	1.45
00 F	8<x<11.2	62.3064	30	464.4	1.1645	1.87
00 F	8<x<11.2	73.7384	45	696.6	1.2943	1.76
00 F	8<x<11.2	80.5752	60	928.8	1.7491	2.17
00 F	8<x<11.2	89.0064	120	1857.6	2.5424	2.86
00 F	11.2<x<16	118.2732	15	232.2	2.4771	2.09
00 F	11.2<x<16	92.4108	30	464.4	1.9515	2.11
00 F	11.2<x<16	95.9326	45	696.6	2.6417	2.75
00 F	11.2<x<16	90.485	60	928.8	2.5465	2.81
00 F	11.2<x<16	108.385	120	1857.6	4.3657	4.03
BKB	8<x<11.2	76.6132	15	232.2	0.8421	1.10
BKB	8<x<11.2	56.8801	30	464.4	1.8318	3.22
BKB	8<x<11.2	57.6045	60	928.8	2.3379	4.06
BKB	8<x<11.2	58.1589	120	1857.6	3.2513	5.59
BKB	11.2<x<16	39.5585	15	232.2	0.4022	1.02
BKB	11.2<x<16	68.1258	30	464.4	1.9410	2.85
BKB	11.2<x<16	59.3349	60	928.8	2.9319	4.94
BKB	11.2<x<16	61.6998	120	1857.6	3.7880	6.14

Table 8: Results of the abrasion experiments

7.5 Interpretation

As acceleration and therefore the theoretical top speed of anything moving down an inclined slope is mass-dependent, blocks of different size and/or porosity will travel at different speeds. Therefore, it is obvious that different blocks will collide with other blocks. The effect of every collision is a matter of relative speed, relative mass and block temperature which in turn may lead to pseudotachylitic structures (Schwarzkopf et al., 2000). However, most collisions result in small bits and pieces of one block being hit off, preferentially along edges or corners. Blocks may be disrupted into smaller angular blocks that may subsequently be abraded upon the next impact or simply by rolling along the ground. It remains speculative, which of the performed experiments is closest to the degree of abrasion during the natural scenario. Most probably, abrasion has affected the measured grain-size distribution (Kueppers et al., 2005). Due to the instability of the dome and the latent heat, the first overview field work on the BAF deposits was performed in late 1996, however, without a statistically relevant investigation of clast porosity (Miyabuchi, 1999). Shortly after the end of the eruption, fast growing plants were distributed on the BAF deposits by the aid of helicopters to stabilize these deposits and minimize the imminent risk of lahars during the monsoon seasons. Therefore, it remained impossible to distinguish single flow units and field work was performed exclusively on the surface of the BAF deposits (Kueppers et al., 2005). Due to this, a comparison of density distributions achieved at measurement points (MP) at different distance from the dome is barely feasible as the deposits at these MPs might have belonged to different flow units. Additionally, the limited knowledge about the physical state and the relative size and porosity of the blocks involved in a single event made it impossible to precisely pinpoint the actual effect of abrasion during a single event to exactly reveal the abrasion-induced shift in porosity distribution. The results obtained proved the dependency of abrasion on grain size and porosity. The 15 minutes experiments on 00 F and BKB samples reveal a different behaviour. Here, more fine particles have been generated with 00 F samples. This revealed the additional influence of bubble size on the abrasion. Bubble size is smaller in BKB samples leading to an easier abrasion of 00 F samples. The degree of abrasion during the 15 minutes experiments was generally below 2.1 wt.% (sample 00 F, -3.5 Φ). As this time span is comparable to the final drying interval of the fine particles in the rotational vaporizer, the shift of the grain-size distribution to smaller particles is found to be minor.

IV Conclusion

Enhanced knowledge of pre- and syn-eruptive processes is vital to deal with the increasing threat imposed to population and infrastructure by volcanoes that have been active historically and may potentially erupt in future. For many years, most of this knowledge was received from experiments on analogue materials and/or numerical models. In order to increase their significance and applicability for the "real" case, the natural complexity may not be oversimplified and the input parameters must be reliable and realistic. In the light of this, a close connection of field and laboratory work is essential.

During two field campaigns, the density distribution of the deposits of the 1990-1995 eruption of Unzen volcano, Japan has been investigated in detail. The results showed the relative abundances of clast porosity, revealed a bimodal density distribution and allowed conclusions on magma ascent and degassing conditions.

In the laboratory, the fragmentation behaviour upon rapid decompression has been investigated in a modified fragmentation bomb (Spieler et al., 2004). At 850 °C, initial overpressure conditions as high as 50 MPa have been applied to sample cylinders (25 mm diameter, 60 mm length) drilled from natural samples. In a first step, the minimum overpressure required to cause complete sample fragmentation (= fragmentation threshold, ΔP_{fr}) has been evaluated. Results from samples of several volcanoes (Unzen, Montserrat, Stromboli, and Mt. St. Helens) showed that ΔP_{fr} mainly depended on open porosity and permeability of the specific sample as these parameters were controlling pressure build-up and loss. The experiments further revealed that sample fragmentation was not the result of a single process but the result of a combination of simultaneously occurring processes as indicated by Alidibirov et al. (2000). The degree of influence of a single process to the fragmentation behaviour was found to be porosity-dependent.

Further experiments at initial pressure conditions above ΔP_{fr} and close investigation of the artificially generated pyroclasts allowed evaluating the fragmentation efficiency upon changing physical properties of the used samples. The efficiency of sample size reduction was investigated by grain-size analysis (dry sieving for particles bigger than 0.25 mm and wet laser refraction for particles smaller than 0.25 mm) and surface area measurements (by Argon adsorption). Results of experiments with samples of different porosities at different initial pressure values showed that the efficiency of fragmentation increased with increasing energy.

The energy available for fragmentation was estimated from the open porosity and the applied pressure.

A series of abrasion experiments was performed to shed light on the grain size reduction due to particle-particle interaction during mass movements. The degree of abrasion was found to be primarily depending on porosity and experimental duration. The results showed that abrasion may change the density distribution of block-and-ash flows (BAF) by preferentially abrading porous clasts. However, during the short drying interval prior to the analysis of the experimental pyroclasts, abrasion-induced grain-size reduction only played a minor role and was assumed to be negligible.

Anhang

	Year of eruption	SiO_2 (whole rock)	SiO_2 (matrix)	Phenocrysts (%/max. size)	matrix crystalls (%)	open porosity (%)	closed porosity (%)
Unzen	1991-1995	dacitic (65%)	rhyolitic (78-80 %)	Plagioclase, hornblende, biotite, quartz (23-28 %/20 mm)	Plagioclase, Pargasit, Pyroxene, Fe-Ti-oxides, Apatite (33-50 %)	1-35 % (dome lavas), up to 57 % (bread-crust bombs)	< 2.5 % (dome lavas), up to 6.5 % (bread-crust bombs)
Stromboli	2003	no data	Biondo: basaltic (49.5 %)/ Bruno: shoshonitic 53 %	Biondo: Pyroxene, Plagioclase, Olivine (together 1-2 %) / Bruno: porphyritic with Pyroxene (up to 5 mm), Plagioclase and Olivine	Biondo: nearly no microlites / Bruno: Pyroxene, Plagioclase, Olivine, Ti-Magnetite and Apatite	Biondo (80-84.5%) / Bruno (43-52%)	< 0.7 % (Biondo) / < 1.2 % (Bruno)
Montserrat	1997	andesitic (58-62%)	rhyolitic (76-79 %)	Plagioclase (30-35 %), Amphibole (6-10%), Orthopyroxene, Ti-Magnetite and Quartz	Microphenocrysts (15-20 %), Microlites (20-30 %)	Lava (2.5 %)/ Pumice (67 %)	< 1.2 % (Lava) / 5.5-7.5 % (Pumice)
Mt. St. Helens	1980	dacitic (65%)	no data	Plagioclase, Hypersten, Hornblende and Fe-Ti-Oxides (30%/< 210 µm)	mostly plagioclase (45%/< 10 µm)	36.5 %	< 4 %

Anhang 1: Petrological description of the sample sets used in this study. Data on Unzen and Montserrat from Scheu (2005) and literature cited therein. Data on Stromboli from Andronico et a. (preliminary report from INGV Catania, 2003). Data from Mt. St. Helens from Spieler et al. (2003).

Reference list

Alidibirov M (1994) A model for viscous magma fragmentation during volcanic blasts. Bull Volcanol 56, 459-465

Alidibirov M and Dingwell DB (1996) An experimental facility for investigation of magma fragmentation by rapid decompression. Bull Volcanol 58, 411-416

Alidibirov M and Dingwell DB (2000) Three fragmentation mechanisms for highly viscous magma under rapid decompression. JVGR 100, 413-421

Andronico D, Bertagnini A, Corsaro RA, Landi P, Miraglia L, Pompilio M (2003) Caratteri mineralogico-petrografici dei prodotti emessi durante l'esplosione dello Stromboli del 5 aprile 2003. Preliminary report of INGV Catania

Avramov I (1994) Viscosity of undercooled melts. Journal of Materials Science letters 13, 1367-1369

Belikov BP, Zalesskii BV, Rozanov YA, Sanina EA, and Timchenko IP (1964) Methods of studying the physicomechanical properties of rocks. In: Zalesskii BV (ed.) Physical and mechanical properties of rocks. Izdatel'stvo Nauka, Moskau, 1-58

Botcharnikov R, Holtz F, Behrens H, and Sato H (2003) Phase equilibrium study and constraints on pre-eruptive conditions of Unzen magmas. Abstract volume of IODP-ICDP meeting 2003, Mainz, Germany

Cagnoli B, Barmin A, Melnik O, and Sparks RSJ (2002) Depressurization of fine powders in a shock tube and dynamics of fragmented magma in volcanic conduits. EPSL 204, 101-113

Cas RAF and Wright JV (1987) Volcanic successions: modern and ancient. Chapman & Hall, London Glasgow New York Tokyo Melbourne Madras, 476-478

Dingwell DB (1996) Volcanic dilemma: Blow or flow? Science 273, 1054-1055

Dingwell DB (1998) Recent experimental progress in the physical description of silicic magma relevant to explosive volcanism. In: Gilbert JS and Sparks RSJ (eds.) The physics of explosive volcanic eruptions. Geol.Soc., London, Spec. Pub., 145, 9-26

Gardner JE, Thomas RME, Jaupart C, and Tait S (1996) Fragmentation of magma during Plinian volcanic eruptions. Bull Volcanol 58, 144-162

Hoblitt RP and Harmon RS (1993) Bimodal density distribution of cryptodome dacite from the 1980 Mount St. Helens, Washington. Bull Volcanol 55, 421-437

Hoshizumi H, Uto K, and Watanabe K (1999) Geology and eruptive history of Unzen volcano, Shimabara Peninsula, Kyushu, SW Japan. JVGR 89, 81-94

Hoshizumi H, Uto K, Matsumoto A, and Kurihara A (2004) Growth history of Unzen volcano, Kyushu, Japan – Results of two flank drillings of Unzen Scientific Drilling Project. Abstract V24B-02, AGU Fall meeting

Houghton BF and Wilson CJN (1989) A vesicularity index for pyroclastic deposits. Bull Volcanol 51, 451-462

Ichihara M, Rittel D, and Sturtevant B (2002) Fragmentation of a porous viscoelastic material: Implications to magma fragmentation. J. Geophys. Res. 106, 2226-2239

Koptsik S, Strand L, and Clarke N (2003) On the calculation of the surface area of different soil size fractions. Applied Geochemistry 18, 629-651

Kueppers U, Scheu B, Spieler O, Dingwell DB (2005) Field-based density measurements as tool to identify pre-eruption dome structure: set-up and first results from Unzen volcano, Japan. JVGR 141, 65-75.

Mader HM, Philips JC, Sparks RSJ, and Sturtevant B (1996) Dynamics of explosive degassing of magma: observations of fragmenting two-phase flows. J. Geophys. Res. 101, 5547-5560

Mastrolorenzo G, Brachi L, and Canzanella A (2001) Vesicularity of various types of pyroclastic deposits of Campi Flegrei volcanic field: evidence of analogies in magma rise and vesiculation mechanisms. JVGR 109, 41-53

Mayfield JD and Schiffman P (1998) Measuring the density of porous volcanic rocks in the field using a saran coating. Journal of geoscience education 46, 460-464

McBirney AR and Murase T (1970) Factors governing the formation of pyroclastic rocks. Bull Volcanol 34, 372-384

Miyabuchi Y (1999) Deposits associated with the 1990-1995 eruption of Unzen volcano, Japan. JVGR 89, 139-158

Mueller S, Spieler O, Scheu B, and Dingwell DB (2005) Permeability and degassing of dome lavas undergoing rapid decompression: an experimental determination. Bull Volcanol doi: 10.1007/s00445-004-0392-4

Mueller S, Spieler O, Kueppers U, Scheu B, and Dingwell DB (2005) Density Distribution in Pyroclastic Deposits: A Comparative Study. Abstract at EGU meeting, Vienna, Austria

Mungall JE (1995) Textural controls on explosivity of lava in Merapi-type block and ash flows. Extended Abstract of IAVCEI meeting

Nakada S and Tanaka M (1991) Magmatic processes of Unzen volcano. Bulletin of the Volcanological Society of Japan 36, 113-121

Nakada S and Motomura Y (1999) Petrology of 1990-1995 eruption. JVGR 89, 173-196

Nakada S, Shimizu H, and Ohta K (1999) Overview of the 1990-1995 eruption at Unzen volcano. JVGR 89, 1-22

Nakada S, Yoshimoto M, Shimano T, Kurokawa M, Nakai S, Sugimoto T, Hoshizumi H, Oguri K, Noguchi S, and Goto Y (2004) Petrology of conduit lava at Unzen volcano; results of Unzen Scientific Drilling Project. Abstract V33D-1491, AGU Fall meeting

Nonaka M, Nakada S, and Goto Y (2004) Emplacement process of the 1991-1995 dome at Unzen volcano, Japan. Abstract V33D-1486, AGU Fall meeting

Okada H (1992) Geological and tectonic setting of Unzen volcano. In: Yanagi T, Okada H, and Ohta K (eds.) Unzen volcano – the 1990-1992 eruption. The Nishinippon Kyushu University Press, 1992

Papale P (1999) Strain-induced magma fragmentation in explosive eruptions. Nature 397 425-428

Polacci M, Pioli L, and Rosi M (2003) The plinian phase of the campanian ignimbrite eruption (Phlegrean Fields, Italy): evidence from density measurements and textural characterization of pumice. Bull Volcanol 65, 418-432

Raue H (2004) Magmenfragmentation im bruchhaften Regime: ein neues Modell zur Energiebilanzierung am Beispiel der Phlegräischen Felder/Italien. PhD Thesis, University of Würzburg, Germany

Richet P and Bottinga Y (1995) Rheology and configurational entalpy of silicate melts. Reviews in Mineralogy 32, 67-93

Riley CM, Rose WI, and Bluth GJS (2003) Quantitative shape measurements of distal volcanic ash. J. Geophys. Res. 108 (B10) 2504, doi:10.1029/2001JB000818

Romano C, Mungall J, Sharp T, and Dingwell DB (1996) Tensile strengths of hydrous vesicular glasses: an experimental study. Am. Mineral. 81 (1996) 1148–1154

Sakuma S, Nakada S, and Uto K (2004) Unzen Scientific Drilling Project: Challenging drilling operation into the magmatic conduit shortly after eruption. Abstract V24B-03, AGU Fall meeting

Scheu B (2005) Understanding silicic volcanism: Constraints from elasticity and failure of vesicular magma. PhD thesis, University of München, Germany

Schleyer R (1987) The goodness of fit to ideal Gauss and Rosin distributions: a new grain-size parameter. J. Sed. Petrol. 57, 871-880

Schopper JR (1982) Porosity and permeability. In: Angenheister G (ed) Numerical Data and Functional Relationships in Science and Technology. Springer, Berlin Heidelberg New York, 184-193

Schwarzkopf LM, Schmincke HU, and Troll VR (2001) Pseudotachylite on impact marks of block surfaces in block-and-ash flows at Merapi volcano, Central Java, Indonesia. Geol. Rundsch. 90, 769-775

Smith JV, Miyake Y, and Oikawa T (2001) Interpretation of porosity in dacite lava domes as ductile-brittle failure textures. JVGR 112, 25–35

Sparks RSJ (1978) The dynamics of bubble formation and growth in magmas: a review and analysis, JVGR 28, 257-274.

Sparks RSJ, Barclay J, Jaupart C, Mader HM, and Phillips JC (1994) Physical aspects of magma degassing. I. Experimental and theoretical constraints on vesiculation, Rev. Mineral. 30, 414-445

Spieler O (2001) Die Fragmentierung hochviskoser Magmen – Experimenteller Aufbau und Analysetechniken, PhD thesis, University of Munich, Germany

Spieler O, Alidibirov M, and Dingwell DB (2003) Grain-size characteristics of experimental pyroclasts of 1980 Mount St. Helens cryptodome dacite: effects of pressure drop and temperature. Bull. Volcanol. 65, 90– 104.

Spieler O, Dingwell DB, and Alidibirov M (2004) Magma fragmentation speed: An experimental determination. JVGR 129, 109-123.

Spieler O, Kennedy B, Kueppers U, Dingwell DB, Scheu B, and Taddeucci J (2004) The fragmentation threshold of pyroclastic rocks. EPSL 226, 139-148

Taddeucci J, Spieler O, Ichihara M, Dingwell DB, and Scarlato P (2004) Vesiculation, fragmentation, and degassing in a viscoelastic magma analogue. IAVCEI General Assembly, Pucòn, Chile

Ui T, Matsuwo N, Suita M, and Fujinawa A (1999) Generation of block-and-ash flows during the 1990-1995 eruption of Unzen Volcano, Japan. JVGR 89, 123-137

Umakoshi K, Shimizu H, Matsuwo N and Ohta K (1992) Surface temperature measurements of lava domes and pyroclastic flows by infrared thermal video system. In: Yanagi T, Okada H, and Ohta K (eds.) Unzen volcano – the 1990-1992 eruption. The Nishinippon Kyushu University Press, 1992

Venezky DY and Rutherford MJ (1999) Petrology and Fe-Ti oxide reequilibration of the 1991 Mount Unzen mixed magma. JVGR 89, 213-230

Watanabe K and Hoshizumi H (1995) Geological Map of Unzen volcano. Geological map of volcanoes 8, Geological survey of Japan

Webb SL and Dingwell DB (1989) Structural relaxation in silicate melts and non-Newtonian melt rheology in igneous processes. Physics and Chemistry of Minerals 16, 508-516

Woods AW, Sparks RSJ, Ritchie LJ, Batey J, Gladstone C, and Bursik MI (2002) The explosive decompression of a pressurized volcanic dome: the 26 December 1997 collapse and explosion of Soufrière Hills Volcano, Montserrat. In: Druitt TH and Kokelaar BP (eds.) The eruption of Soufrière Hills Volcano, Montserrat, from 1995 to 1999. Geological Society, London, Memoirs, 21, 595-602

Zhang Y (1999) A criterion for the fragmentation of bubbly magma based on brittle failure theory. Nature 402, 648 – 650

Zimanowski B, Wohletz K, Dellino P, and Buettner R (2003) The volcanic ash problem. JVGR 122, 1-5

Product Manual COULTER LS Series, Version 2.11a (August 1997)

Operator's Manual Gemini III 2375 Surface Area Analyzer, Version 237-42825-01 (October 1996)

Curriculum Vitae

Persönliche Daten:

Ulrich Küppers, geboren am 27. April 1973 in Krefeld, Germany, wohnhaft in Waakirchen

Schulbildung:

1979 – 1983	Besuch der Grundschule Schaftlach
1983 – 1992	Besuch des Gymnasiums Tegernsee
Juli 1992	Erwerb der allgemeinen Hochschulreife

Studium:

November 1993 – September 1999	Studium der Geologie/Paläontologie am Institut für Allgemeine und Angewandte Geologie der Ludwig-Maximilians-Universität (LMU) München
Juli 1999	Erwerb des Diploms in Geologie/Paläontologie
Seit Juni 2000	Promotion am Institut für Mineralogie, Petrologie und Geochemie der LMU München (seit 2002 Sektion Mineralogie am Department für Geo- und Umweltwissenschaften der LMU München)

Berufstätigkeit:

Oktober 1992 – Januar 1994	Zivildienst beim Bayerischen Roten Kreuz Miesbach
Januar 1998	Praktikum am Istituto Internationale di Vulcanologia, Catania, Italien
April 1998	Praktikum am Bayerischen Landesamt für Wasserwirtschaft, München
Oktober 1999 – Mai 2000	Angestellter bei der Dr. Rietzler & Heidrich GmbH, Rosenheim (geologisches Ingenieurbüro)
Juni 2000 – September 2002	wissenschaftlicher Angestellter in der Sektion Mineralogie, Petrologie und Geochemie der LMU München
seit Oktober 2002	wissenschaftlicher Angestellter am Department für Geo- und Umweltwissenschaften der LMU München